Chapter 3

SUPPLEMENTARY INFORMATION FOR ATP CONSUMPTION IN SPACE AND TIME IN MICROTUBULE-MOTOR STRUCTURES

3.1 Materials and Methods

Sample Chambers for Aster, ATP Calibration, and ATP Hydrolysis Experiments

For both the aster and ATP hydrolysis experiments, a flow cell was created by placing parafilm spacers between a microscope slide and a cover glass. A mild heat treatment at 65 °C was applied to facilitate the adhesion of parafilm to the glass surfaces, resulting in a flow cell that is approximately 70 – 100 μm in height and has a volume of approximately 5 μL. To prevent nonspecific protein adsorption onto the glass, the glass surfaces were coated with an acrylamide brush [1]. The reaction mixture was loaded into each channel by capillarity and sealed with a fast-setting silicone polymer (Picodent Twinsil Speed).

Sample Preparation and Reaction Mixture for Aster and ATP Hydrolysis Experiments

For aster experiments involving Ncd motors, the reaction mixture consisted of Ncd-mCherry-micro, Ncd-mCherry-iLID, 2.8 μM A81D, and microtubules (1.5 μM tubulin). We systematically varied the final concentrations of each Ncd motor type from 0.2 μM to 0.75 μM, supplemented with 500 μM of MgATP (Sigma A9187). Additionally, aster experiments were conducted with K401-mCherry-micro, K401-iLID, 2.8 μM A81D, and microtubules (1.6 μM tubulin), resulting in a final concentration of 0.25 μM for each motor type with 1000 μM of MgATP.

For ATP hydrolysis experiments, we varied the concentration of MgATP (ranging from 50 μM to 1420 μM), ADP (ranging from 0 μM to 1420 μM), and potassium phosphate (pH 7.0, ranging from 0 mM to 40 mM) using 1 μM Ncd-mCherry-micro, 1.4 μM A81D, and microtubules (1.5 μM tubulin).

The concentrations are specifically associated with protein monomers in the cases of Ncd-mCherry-micro and Ncd-mCherry-iLID, along with K401-mCherry-micro and K401-iLID, whereas tubulin represents the protein dimer.

For both aster and ATP hydrolysis experiments, the reaction mixture consisted of 66.7 mM PIPES at pH 6.8, 4.7 mM $MgCl_2$, 0.83 mM EGTA, a crowding agent (20-22% glycerol, Sigma, G5516), a surface passivating agent (0.50 mg/mL Pluronic F-127, Sigma, P2443), and an oxygen-scavenging system to prevent photobleaching (0.37 mg/mL pyranose oxidase, Sigma, P4234; 7.2 mg/mL glucose, Thermo Fisher Scientific, USA; 9 μg/mL catalase, Sigma, C40; 5.4 mM DTT, Thermo Fisher Scientific, USA; 2.0 mM Trolox, Sigma, 238813).

Sample preparation and handling were performed in a dark room with red light to minimize early light activation of the optogenetic proteins. We prepared the reaction mixture right before loading it into the flow cell and sealed it using Picodent Twinsil Speed. The experiments were repeated at least three times at room temperature (approximately 25°C).

Activation and Imaging Protocol for aster and ATP hydrolysis experiments

In experiments focusing on aster formation, we selected one position within the flow channel, which is illuminated by an excitation region with a diameter of 400 μm. In the case of experiments related to ATP hydrolysis, the entire field of view is illuminated. GTypically, one experiment is conducted per flow channel.

The fluorescent motors (mCherry labeled) and the A81D ATP probe were imaged simultaneously every 20 seconds using a $\times$10 objective. The exposure time values for 405nm and 480nm excitations were 33-150 ms and 50-160 ms, respectively, and 100-300 ms for 587 nm mCherry excitation.

ATP Calibration Assays

For our ATP hydrolysis experiments, we used a ratiometric fluorescent ATP probe, QUEEN 7μ mutant, A81D) [2], which allows the estimation of ATP levels in the reaction mixture. In these assays, we quantified the fluorescence intensity of A81D, which serves as a reporter system coupled with a fluorophore to monitor ATP hydrolysis by Ncd-mCherry-micro or K401-mCherry-micro motor proteins in our experiments.

For ATP calibration experiments, we examine the relationship between the QUEEN 405/480 ratio and MgATP concentration, ranging from 0 μM to 3000 μM. We used 1.4-2.8 μM A81D with GMP-CPP-stabilized microtubules (1.5 μM tubulin) in the reaction mixture at various MgATP concentrations. The composition of the reaction

mixture for ATP calibration is the same as outlined in section 3.1, excluding motor proteins.

Epifluorescence imaging was performed every 20s using excitation filters (405 and 480 nm) and a $\times$10 objective. The exposure time values for 405nm and 480nm excitation are 33-150ms and 50-160ms, respectively. Typically, five positions within the same flow cell were chosen for averaging. The experiments are performed at room temperature (approximately 25°C).

Flow Chamber, Sample Preparation, and Imaging Protocol for Microtubule Gliding Assays

The flow chambers were constructed as previously described [3]. In brief, we built a chamber by assembling an amino-silanized coverslip and an acrylamide-coated microscope slide separated by melted parafilm spacers.

We treated the amino-silanized glass surface with glutaraldehyde to attach antibodies. For this purpose, the chamber was incubated with 10% (v/v) glutaraldehyde (Sigma, G7776) for 30 minutes. After removing unreacted glutaraldehyde by rinsing the chamber with MilliQ water, it was then incubated with a 0.02 mg/ml solution of anti-FLAG antibody (F3165, Sigma) to specifically bind motor proteins to the glass surface. The remaining exposed surface was blocked with a 0.2% (w/v) Pluronic F-127 (Sigma, P2443) and 2 mg/ml β-casein (Sigma, C6905) solution for 5 minutes. Motors were bound to the surface by incubating Ncd-YFP-iLID FLAG-tag motor proteins (at $\approx$ 1 nM in 10 mg/ml bovine serum albumin (BSA, JT Bakers), 1 mM DTT, and 500 μM mgATP in M2B buffer (80 mM PIPES, 1 mM EGTA, 2 mM $MgCl_2$)) for 5 minutes. Unbound motors were washed out with M2B, and then AlexaFluor 647 labeled GMP-CPP stabilized microtubules in M2B with 1mM DTT were flowed in. After 5 minutes of incubation at room temperature, the flow cell was rinsed with M2B to remove unbound microtubules.

The imaging buffer consisted of M2B buffer with 0.5 mg/ml β-casein, 0.50 mg/mL Pluronic F-127, 3 mM $MgCl_2$, 2 mM Trolox, and an oxygen scavenging system (0.37 mg/ml pyranose oxidase, 7.2 mg/ml glucose, 9 μg/ml catalase, 5.4 mM DTT, 2.0 mM Trolox). In microtubule gliding experiments, we varied the concentrations of mgATP (ranging from 20 μM to 5000 μM), ADP (ranging from 0 μM to 5000 μM), and potassium phosphate (pH 7.0, ranging from 0 mM to 40 mM). Following the addition of the reaction mixture, the flow cell was sealed using Picodent Speed. The experiments were repeated at least three times at room temperature (approximately

25°C).

Image acquisition of AlexaFluor 647-labeled microtubules was performed in a sealed chamber using Total Internal Reflection Fluorescence (TIRF) microscopy with an HCX PL Apo 100×/1.47 TIRF objective. Imaging was performed at one frame per second for 100 seconds. We also imaged Ncd motor proteins (YFP labeled) bound to the glass surface. Individual microtubules were tracked using custom-written Python code to determine their speed.

3.2 Image Analysis

Here we detail our image processing method. We aim to be very careful in checking how our operations modify the data. The predominant goal of the following text is to identify where variation sources occur in our data and how to remove such variation.

The analyzed dataset measures ATP concentration through a fluorescently labeled ATP probe, Queen A81D [2]. The probe contains a superfolder GFP attached to the epsilon subunit of an ATP synthase and capitalizes on the dual excitation peaks of GFP. When ATP binds to the epsilon subunit, there are increased emissions from the 405 nm excitation, and in the unbound state there are increased emissions from the 480 nm excitation state. Taking the ratio of light intensities at 405 nm and 480 nm, an ATP calibration can be created by fitting a curve to the intensity ratio versus ATP concentration, as is shown in Figure 3.10 below. Note that each image should not contain any spatial dependence, as we are measuring the fluorescence of homogeneous mixtures of ATP, the ATP probe, and motor proteins. Without microtubules present, there cannot be any ATP hydrolysis or structure formation.

Background Subtraction

Cameras artificially add an offset to the intensity values of an image to ensure that no pixels are recorded as having less than zero signal [4]. We identify this offset by taking a "dark image," where we close the camera shutter, preventing light from reaching the camera. We use the averaged image of multiple dark images, as shown in Figure 3.1, as the background image subtracted from all fluorescent images.

Figure 3.1: **Camera offset is found by taking a "dark image."** The average of six images are taken with the camera shutter closed. The average offset value is 1913.8 intensity counts. This image is subtracted from all fluorescent images. The horizontal lines present in the image roughly appear at the same place in all images.

Uneven Illumination Correction

Microscopy images of uniform samples can often have artificial gradients of intensity across space. Commonly, this artifact arises from vignetting cast by magnification tubes, non-uniform light sources, and off axis light [5]. Here, we work to distinguish the fraction of an image's variance that is due to a spatial gradient, implying uneven illumination, rather than local fluctuations.

To search for the origin of variation, we will divide our image into a grid. As we prove in Section 3.2, the total variance, σ^2_{tot}, of the image will equal the average variance within a grid block, $\left\langle \sigma^2_{\text{in}} \right\rangle$ plus the variance of the average grid block value, σ^2_{btwn},

$$\sigma^2_{\text{tot}} = \left\langle \sigma^2_{\text{in}} \right\rangle + \sigma^2_{\text{btwn}}. \tag{3.1}$$

If the variance within grid blocks dominates the total variance term, then most of the variation in an image arises from the noise of nearby pixel values, see the second row of Figure 3.2. However, if the variance between grid blocks (the variance of grid block average values) dominate, the image variance is attributable to intensity differences across regions of the image. Since we explore homogeneous ATP images here, we expect all the variance to be within grid blocks. If instead most of the variance is between blocks, this is a sign of uneven illumination, which manifests as a gradient of intensity from one side of the image to the other, see the first row of Figure 3.2. Thus, we can use this grid block method as a metric for the amount of

uneven illumination present in an image.

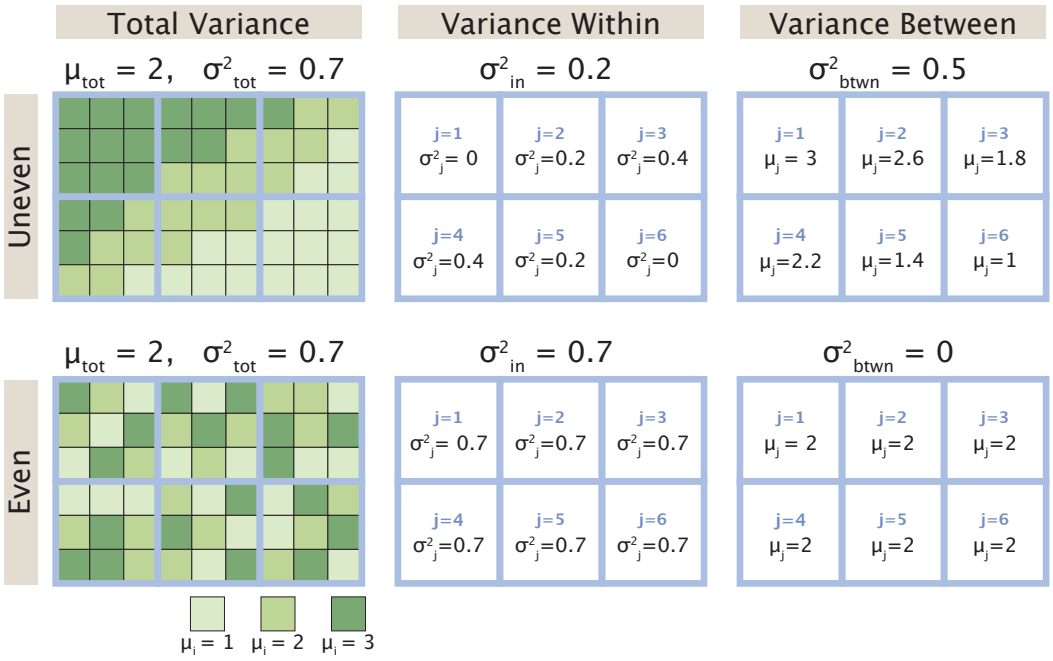

Figure 3.2: **Partitioning of variance for unevenly versus evenly illuminated images.** Here, we go through the exercise of finding the variance within and between blocks for two synthetic images. We assign each pixel value in the first column to have a value between one and three. By eye, we would consider the image in the first row to be unevenly illuminated, since there is an intensity gradient across the image. We would consider the image in the second row to be evenly illuminated, since there is no apparent intensity pattern. Splitting the image into six grid blocks of nine pixels each, we quantify our assumptions. The second column reports the variance of pixels within each grid block. Taking the average of these variances, we report σ^2_{in}, our metric for the variance within grid blocks (as defined by Equation 3.9). In the third column, the mean value of each grid block is reported. Taking the variance of these means gives σ^2_{btwn}, our metric for the variance between grid blocks (as defined by Equation 3.10). While the total image mean and variance for both images are the same, we find that more variance is between blocks in the first row and all the variance is within blocks in the second row. Thus when an image is unevenly illuminated, the variance between blocks dominates.

When dividing our image into into B blocks each containing N_B pixels, we must take note of the variance partitioning in the limits $N_B = 1$ and $N_B = N$, where N is the total number of pixels in the image. In the limiting case that each block only contains one pixel, $N_B = 1$, the variance within a block will be zero and the variance between blocks will equal the total variance of the image. In the opposite limit, where there is one large block containing all pixels, $N_B = N$, the variance

within the block is the total variance of the image and there is no variance between blocks. Thus, we must pick and intermediate N_B block size. In Equation 3.2, we graph the fraction of the variance within blocks versus the number of pixels per block. We find, somewhat surprisingly, that the data fits well to a cubic function of the logarithm of ATP concentration. Since we are looking for a middle ground block size that does not favor variance partitioning in either limit, we look near the inflection points of the curves. In Equation 3.3, we plot the fraction of variance within grid blocks versus the number of pixels per block for all measured ATP conditions. The light gray boxes contain the inflection points of all curves in both bound and unbound ATP channels. In this region, the slopes of all curves are low, implying that regardless of the choice of box size, the fraction of variance within blocks is about the same. Thus, we arbitrarily select the midpoint of the gray box (on a linear scale) as the block size we will use to compare the changes of variance partitioning when correcting images.

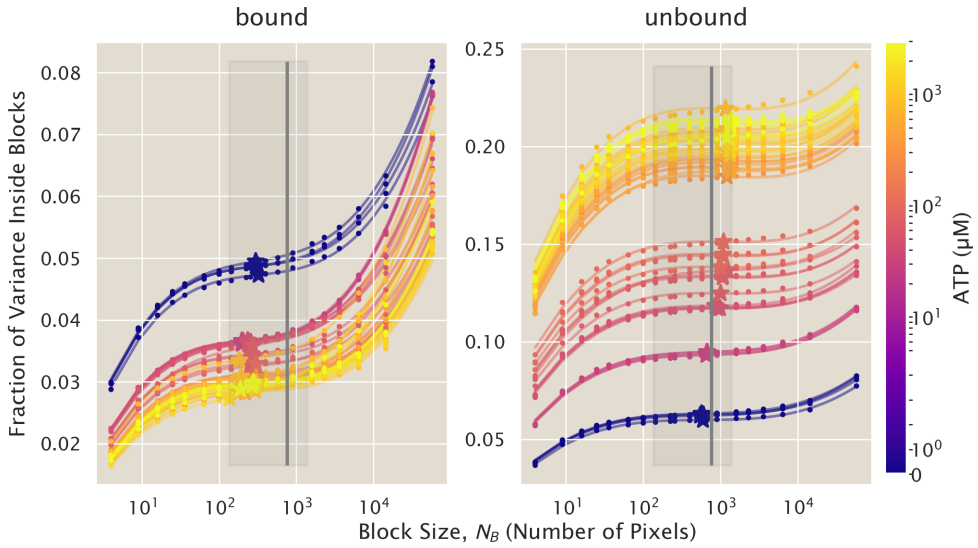

Figure 3.3: **The variance within grid blocks varies with the size of the grid block.** We measure how the variation within a block changes with the number of pixels per grid block (represented by circular markers). The trend fits well to a cubic polynomial of the form $\sigma^2_{\text{in}} = ax^3 + bx^2 + cx + d$, where $x = \ln(N_B)$ and N_B is the number of pixels in a grid block. Each solid line fits the data for a single image and is color coded by the concentration of ATP in the sample. We plot the inflection point for each fit (represented by star markers). The gray box is the region containing all the inflection points from both the bound and unbound channel's images. The gray line plots the midpoint (on a linear scale) of the gray box region. The value of the curves at the gray line as compared to the value at line's inflection point is nearly the same. So, we take this value as an arbitrary size by which we can compare the variance partitioning within versus between blocks as we perform uneven illumination corrections on our images.

From Figure 3.3, we see a very small amount of the variance is located within grid blocks, meaning the vast majority of variance is between grid blocks, implying uneven illumination. We now correct the uneven illumination by fitting a 2D quadratic polynomial of the form,

$$\text{2Dquad}(x, y) = ax^2 + by^2 + cxy + dx + ey + f, \tag{3.2}$$

as described by [6], to our image. Next, we create a normalization matrix from our 2D quadratic polynomial fit,

$$\alpha = \frac{\langle \text{2Dquad}(x, y) \rangle}{\text{2Dquad}(x, y)}, \tag{3.3}$$

where we divide the average polynomial fit value by the value of each filter pixel

value. We then multiply the original image by this filter to find an evened image,

$$\mathrm{im}_{\mathrm{ev}} = \alpha \cdot \mathrm{im}. \tag{3.4}$$

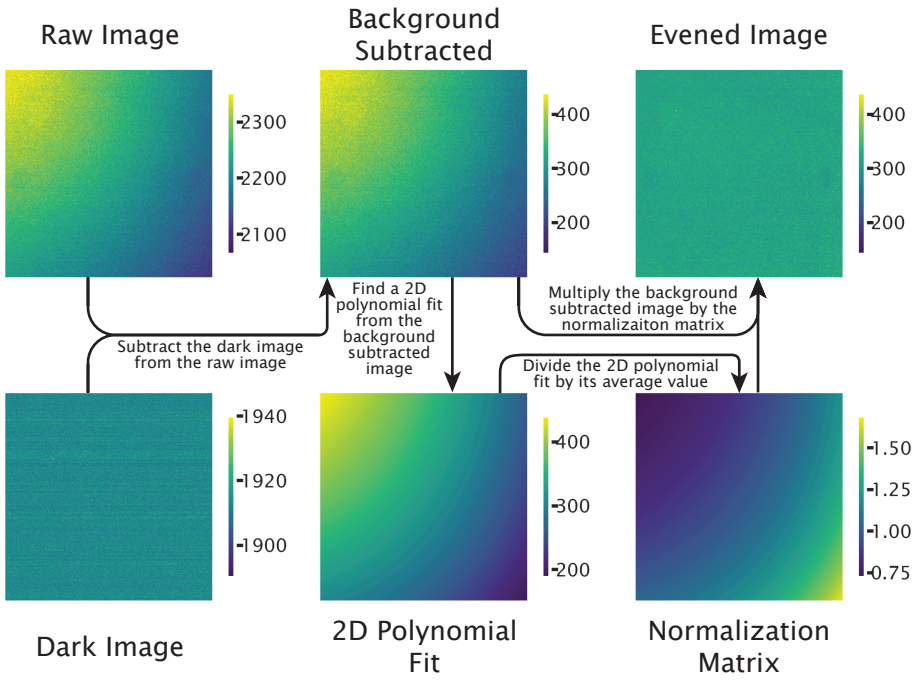

Figure 3.4: **Uneven illumination correction process.** We detail the pipeline to correct uneven illumination in images of homogeneous ATP samples. A camera shutter closed, "dark," image is subtracted from the "Raw Image" to create the "Background Subtracted" image. Then, a 2D polynomial is fit to the "Background Subtracted" image using Equation 3.2. A normalization matrix is created from the 2D polynomial fit using Equation 3.3. Finally, the "Background Subtracted" image is multiplied by the normalization matrix to create an "Evened Image."

By eye, the post-filter image, "Evened Image," in Figure 3.4, does not appear to retain any of the light gradient present in the "Raw Image." We can confirm numerically that after correction, nearly all the image variance is within blocks. In Figure 3.5, the fraction of variance within blocks is plotted for all images, with most images containing over 98% of their variance within grid blocks.

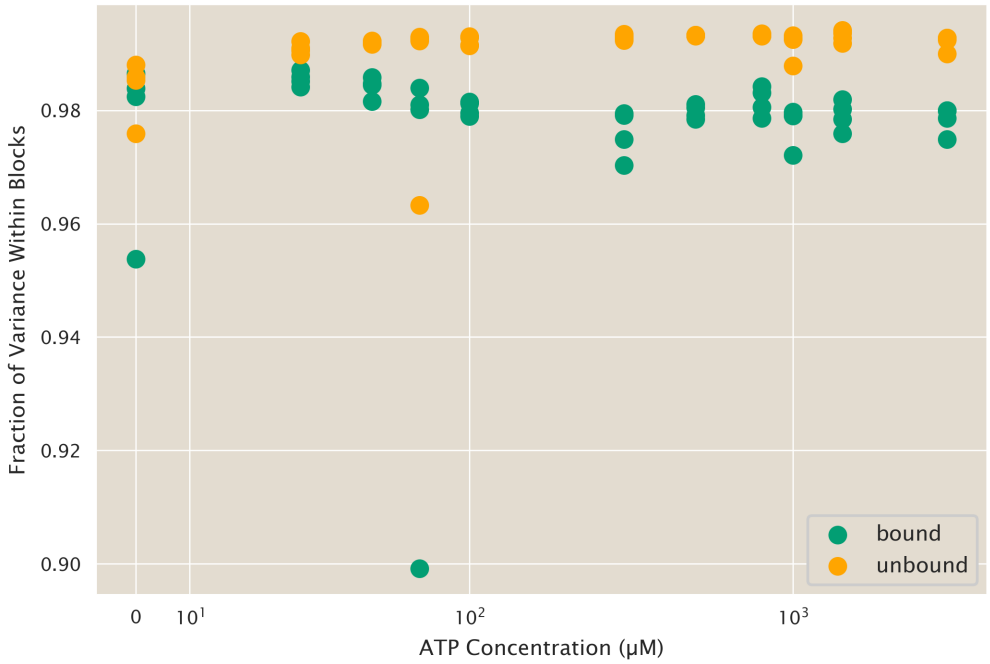

Figure 3.5: **Nearly all of the image variance is located within grid blocks after correction.** After applying a 2D polynomial filter to the images, over 85% of variance is located within grid blocks, and over 98% for most images. There is no apparent correlation between variance fraction and ATP concentration. Green dots mark data from images taken in the bound ATP channel, while orange dot mark data from the unbound ATP channel.

Most of the variance before correction occurred along the $y = -x$ diagonal, as seen in Figure 3.4. Visually, we see the result of the 2D polynomial filter in Figure 3.6, which plots the intensity value of the image versus the distance along the $y = -x$ diagonal, represented by the multiplication of the x and y pixel coordinate. Indeed, we see a negative slope before correction and an approximately zero slope after correction.

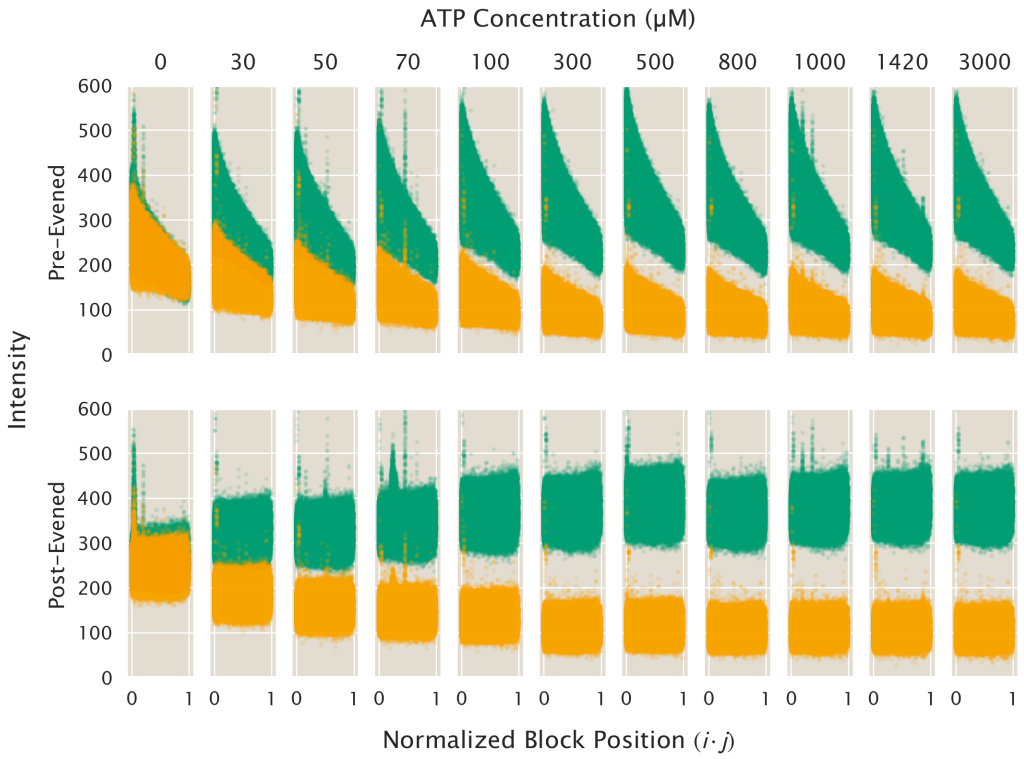

Figure 3.6: **Intensity trend with pixel location.** The intensity value of a pixel versus the location of the pixel is plotted along the upper left to lower right diagonal of the image, as assigned by the multiplication of the pixel coordinates, $i \cdot j$. The green dots represent data from the bound ATP channel (excitation 405 nm) and the orange dots present data from the unbound channel (excitation 480 nm). In the top row of plots, images taken before uneven illumination correction, regardless of ATP concentration or imaging channel, show a negative slope. In the second row, images after uneven illumination correction have approximately no slopes, indicating that the filter correctly removed any illumination bias along the diagonal.

Regardless of the gradient direction, for an image of a homogeneous ATP sample to be even, we would expect grid block averages should be the same across the image. This would imply that there is not a correlation between the intensity of the block and it's location. In Figure 3.7A and Figure 3.7B, we mark the average value for every grid block of every image. The average values are color coded by their grid block's location, which is mapped out in Figure 3.7C. For each ATP concentration, there is no clear trend in the intensity based on block location (with the exception of the corner blocks – the deepest purple and red dots – which are subject to edge effects).

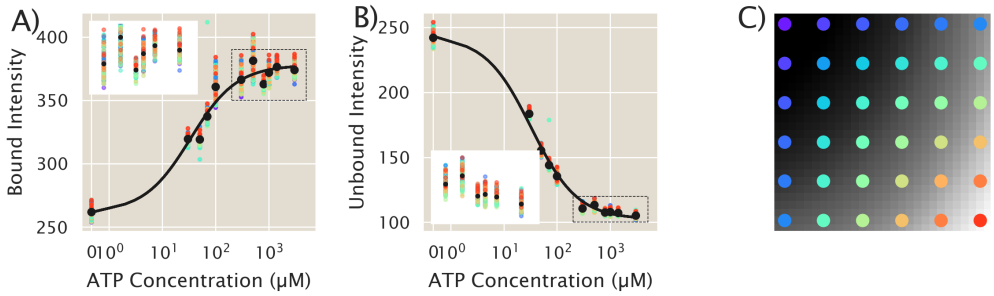

Figure 3.7: **After correction, grid block values of homogeneous ATP images do not depend on block location.** The average grid block intensity values for all images are plotted with respect to the ATP concentration of the sample, where A) reports data from the bound ATP channel and B) reports data from the unbound ATP channel. The data points are color coded by the location of their grid block. Black dots are the average value for each ATP concentration. A subset of data is plotted in the white inset of both figure A) and B) for a zoomed in view of the data spread. The data in the inset is denoted by the dotted black rectangle. A map of the grid block location by color is shown in C) overlayed on an unevened ATP image.

We additionally fit intensity versus ATP concentration for each grid block using a Michaelis-Menten curve of the form,

$$I = (I([\text{ATP}] = \infty) - I([\text{ATP}] = 0)) \frac{[\text{ATP}]}{K_\text{M} + [\text{ATP}]} + I([\text{ATP}] = 0), \tag{3.5}$$

where I is the intensity of the block, and K_M is the Menten constant. We plot the the fit parameters versus the block position in Figure 3.8. Again, there is no significant trend based on the region of the image and the fit parameters are roughly centered about the mean fit parameter.

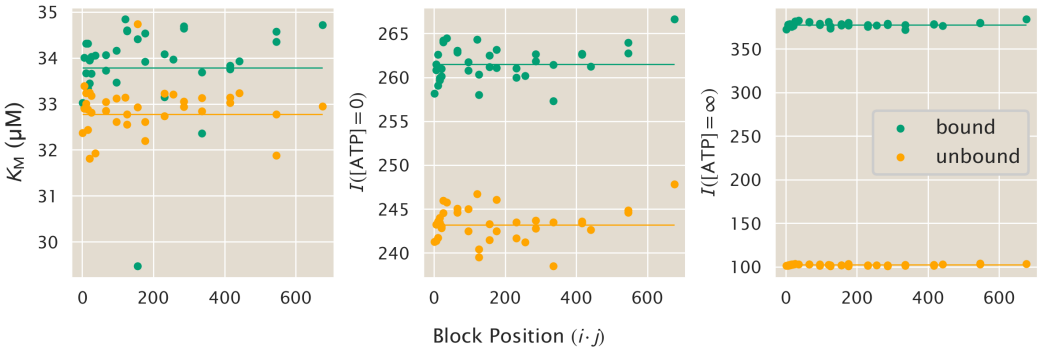

Figure 3.8: **Michaelis-Menten fit parameters of the evened image do not have a trend.** We fit the intensity versus ATP concentration to a Michaelis-Menten curve of the form of Equation 3.5. Plotting the fit parameters versus grid block position, as denoted by multiplying the i, j coordinates of a grid block, we find no trend based on position. The bound ATP channel is plotted in green, while the unbound channel is orange. The fit to the averaged evened images are represented by a horizontal line.

We now have confidence in our ability to correct any image of a homogeneous ATP sample. Taking a 2D polynomial fit of the image, we find the gradient of light and create a normalization matrix to remove it. However, if our image was not of a uniform sample, gradients in light may be due to features of the experiment and thus the image's 2D polynomial fit may not only contain information on uneven illumination. However, if the normalization matrices of homogeneous ATP samples are the same across multiple images and across ATP concentrations, these matrices could be applied to remove uneven illumination from experimental images with real gradients. We compute the normalization matrices for homogeneous images across a range of ATP concentrations. In Figure 3.9, we plot the mean value of 36 grid blocks distributed through the image, where each ATP concentration value has four repeats. The standard deviation is very low, a fraction of a percent, compared to the mean value, indicating the same normalization matrix could be used to describe images taken at a variety of ATP concentrations. However, we do note that each light channel should have its own filter correction as the mean normalizaiton values for images taken at 405 and 480 channel emissions differ.

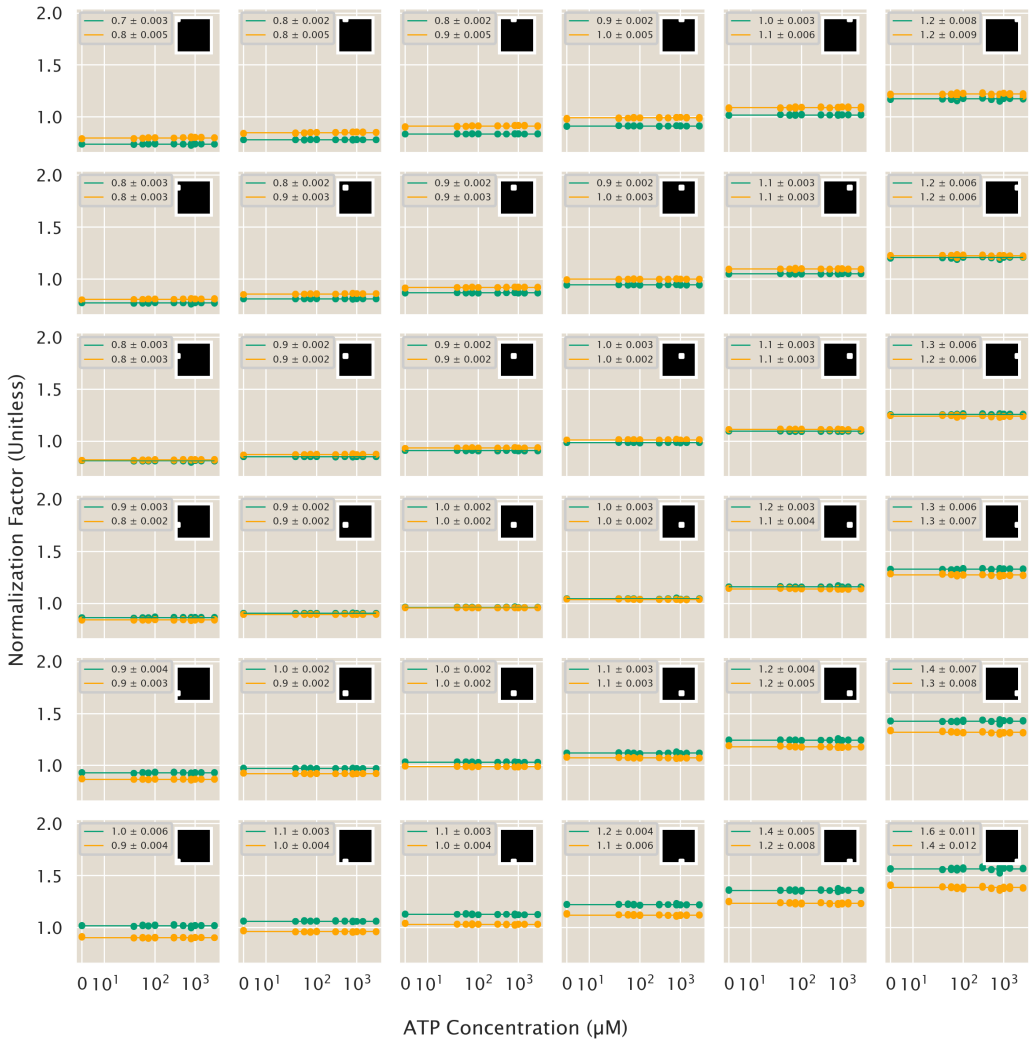

Figure 3.9: **The normalization matrices across ATP concentrations report the same value at a given grid block.** Each subplot charts the average intensity value for a given grid block where the inset shows the location of the grid block within the image. The horizontal lines plot the evened image average and the standard deviation is low, a fraction of a percent compared to the mean, indicating the average of filters well represent each filter.

In this data set, we measure the intensity values reported by the ATP probe for a range of known ATP concentrations. Thus, from these images, we can establish a calibration of the intensity values for given ATP concentrations. Taking the ratio of the bound to unbound image intensity values, we fit the data to a Michaelis-Menten function,

$$R = (R_{\max} - R_{\min}) \frac{\frac{[\mathrm{ATP}]}{K_{\mathrm{M}}}}{1 + \frac{[\mathrm{ATP}]}{K_{\mathrm{M}}}} + R_{\min}, \tag{3.6}$$

where R is the intensity ratio of the bound and unbound channels, [ATP] is the concentration of ATP, and K_M is the Michaelis-Menten constant, as shown in Figure 3.10.

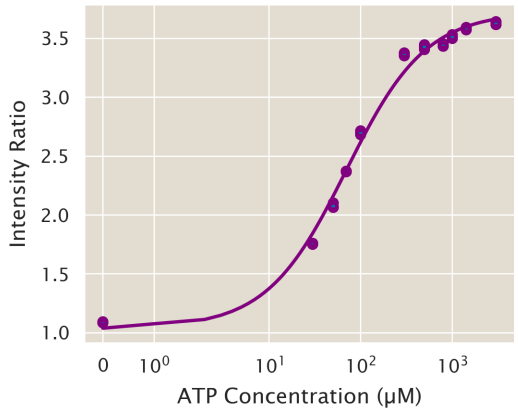

Figure 3.10: **ATP Calibration Curve.** Intensity versus ATP concentration values are plotted where each ATP concentration has four replicates. The data is fit to a Michaelis-Menten curve of the form of Equation 3.6. Here, $K_M = 70\,\mu$M, $R_{max} = 3.7$, and $R_{min} = 1$.

We are left to ask what are the error bars on our calibration? In answering this question, we additionally ask how the standard deviation of intensity values scale with increasing ATP concentration. We plot the histograms of intensity values for the evened images in Figure 3.11. We find that as the ATP concentration increases, so does the mean, while the standard deviation remains nearly constant. We plot the Gaussian distribution given our histogram's mean and standard deviation and find the intensity is well predicted by a Gaussian of the form,

$$\frac{1}{\sqrt{2\pi\sigma}} \exp\left(\frac{-(x-\mu)^2}{2\sigma^2}\right). \tag{3.7}$$

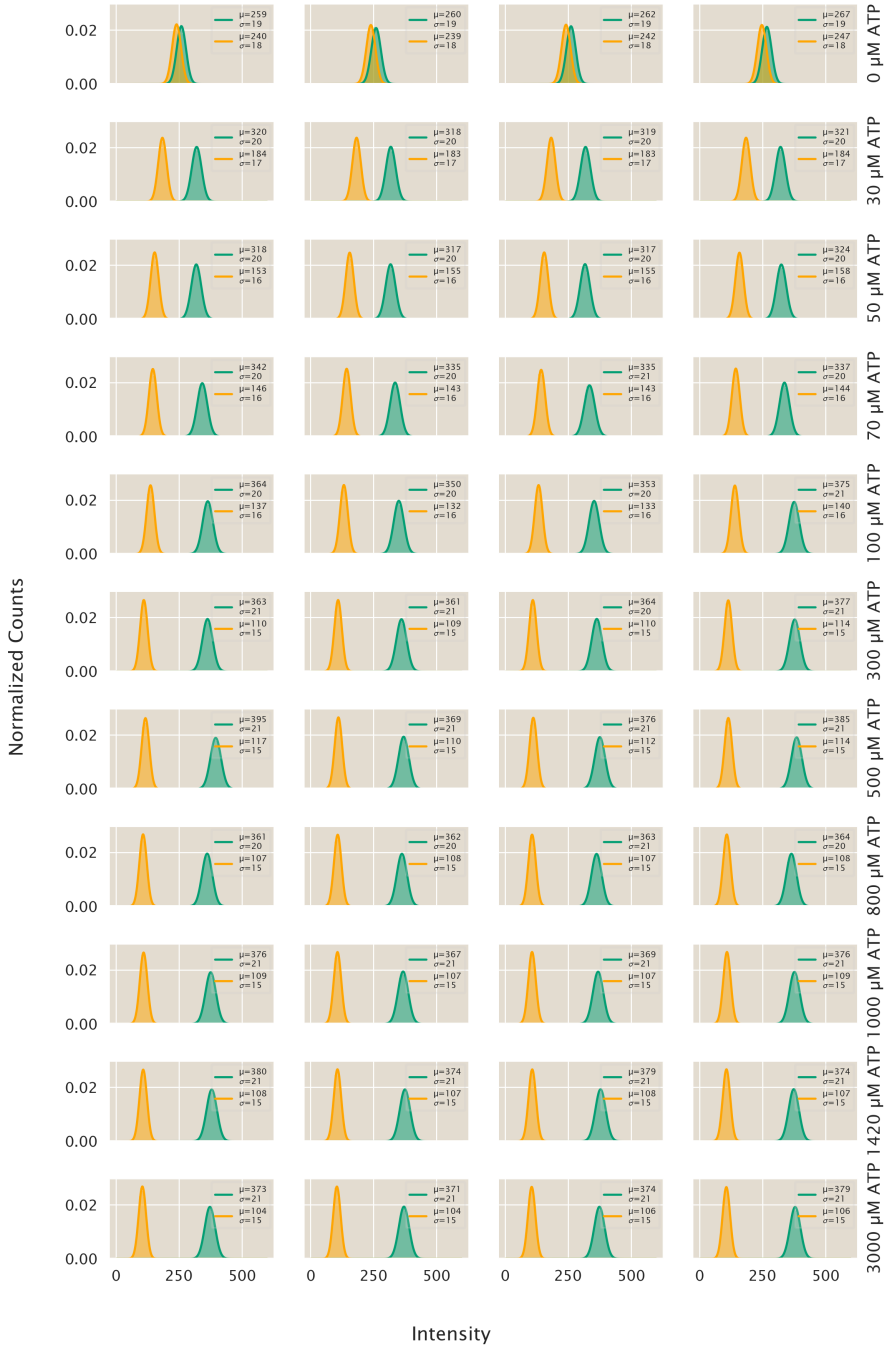

Figure 3.11: **Intensity histograms of evened images are Gaussian distributed.** Each row contains intensity distributions for four replicate images at a given ATP concentration. Plugging the mean and standard deviations of the histograms into Equation 3.7, a Gaussian curve describing the distribution is plotted by the solid line. With increasing ATP concentration, there is little change in the standard deviation relative to the mean. Green curves represent the bound excitation channel, while orange curves represent the unbound excitation channel.

While dividing two Gaussian functions does not result in a Gaussian, we find the ratio of bound to unbound intensities can still be approximated by a Gaussian, as shown in Figure 3.12. We now find there is a significant broadening in the histograms, indicating that as the ATP concentration increases, so too does the ratio mean and standard deviation.

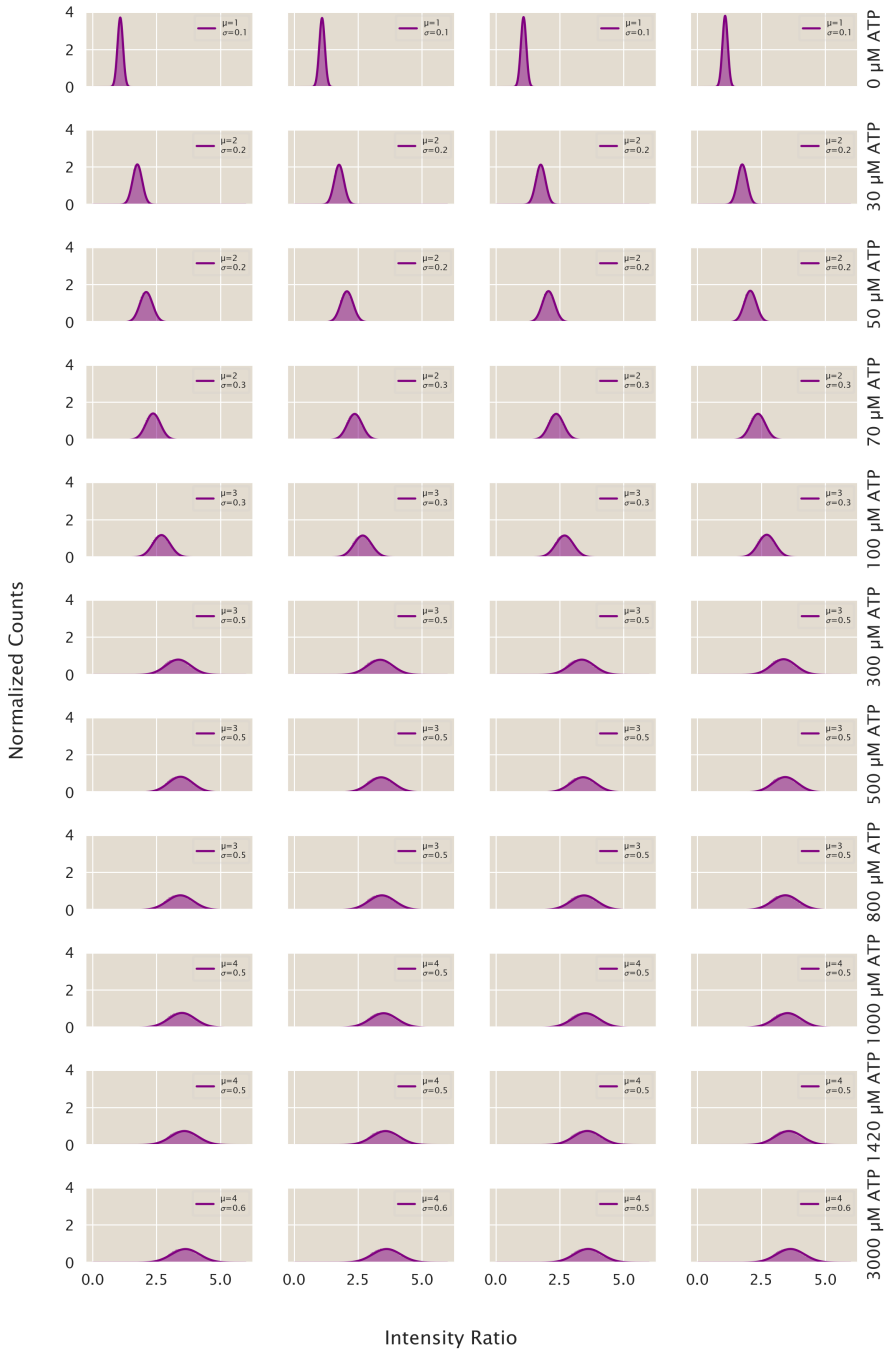

Figure 3.12: **Intensity ratios are Gaussian distributed.** Each row contains intensity ratio distributions for four replicate images at a given ATP concentration. Plugging the mean and standard deviations of the histograms into Equation 3.7, a Gaussian curve describing the distribution is plotted by the solid line. As ATP concentration increases, there is significant broadening of the ratios histogram, such that the standard deviation increases.

Understanding how the standard deviation scales with the mean of the intensity ratio distribution can help inform us how to compute the error of our calibration at various ATP concentrations. In Figure 3.13, the standard deviation is shown to trend linearly with the mean of the histograms. For the intensity values measured by the bound and unbound channels, there is a very small slope, 0.02, such that the standard deviation is relatively unaffected by the mean. However, for the ratio of these two channels, the slope is, 0.18, which results in notable changes in the standard deviation for our range of ATP concentrations. Thus, our next step will be to use these results to model the error on our ATP calibration fit.

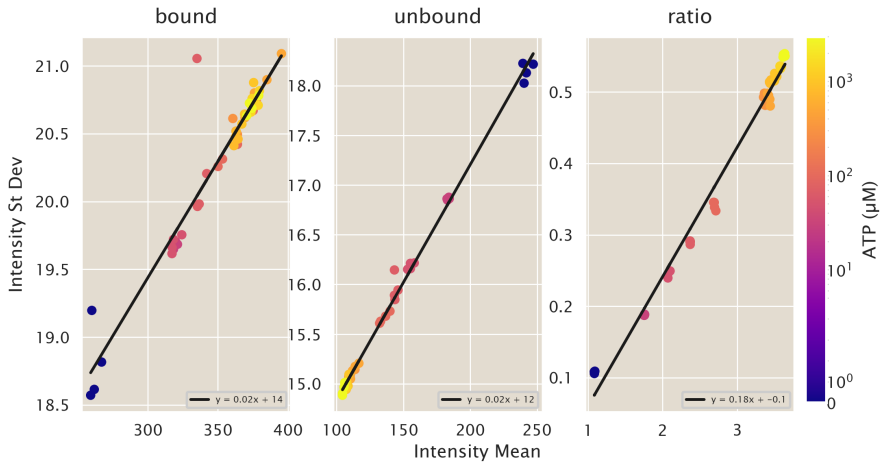

Figure 3.13: **The mean and standard deviation of intensity histograms are linearly related.** Here we plot the standard deviation versus the mean across ATP concentrations and linearly fit the data (black line). For both the bound and unbound intensity channels, there is a weak positive slope of 0.02 between the mean and standard deviation of the intensity distributions. However, there is a larger slope of 0.18 for the distribution of the ratio of intensities. Thus, the linear relation describes the broadening of the histograms seen in Figure 3.12 .

Proof the Total Variance is the Sum of the Variances Within and Between Grid Blocks

The total variance of the image, can be written as

$$\sigma^2_{\text{tot}} = \frac{1}{N}\sum_{i}^{N}(I_i - \langle I \rangle)^2 \tag{3.8}$$

where i sums over each pixel, I_i is the intensity value of a given pixel, and $\langle I \rangle$ is the average intensity value of all pixels in the image. To understand if most of the

variance in the images occur within given regions of the image or between regions of the image, we divide the image into a grid with B blocks each containing N_B pixels. Inside of a given grid block, indexed j, the variance is

$$\sigma_{\text{in}}^2 = \sigma_{\text{j}}^2 = \frac{1}{N_B} \underbrace{\sum_{i}^{N_B}}_{\text{in } j} \left(I_i - \langle I \rangle_j \right)^2, \tag{3.9}$$

which sums over all pixels, i, that are within block j, and where $\langle I \rangle_j$ is the average of pixel intensity values within block j. Finally, we define the variance between blocks as,

$$\sigma_{\text{btwn}}^2 = \frac{1}{B} \sum_{j}^{B} \left(\langle I \rangle_j - \langle I \rangle \right)^2. \tag{3.10}$$

Let us rewrite the form of the total variance to see how it relates to the variance inside and between blocks,

$$\sigma_{\text{tot}}^2 = \frac{1}{B} \sum_{j}^{B} \frac{1}{N_B} \underbrace{\sum_{i}^{N_B}}_{\text{in } j} \left(I_i - \langle I \rangle \right)^2. \tag{3.11}$$

Expanding the square yields,

$$\sigma_{\text{tot}}^2 = \frac{1}{B} \sum_{j}^{B} \frac{1}{N_B} \underbrace{\sum_{i}^{N_B}}_{\text{in } j} \left(I_i^2 - 2 I_i \langle I \rangle + \langle I \rangle^2 \right). \tag{3.12}$$

We add and subtract $-2 I_i \langle I \rangle_j + \langle I \rangle_j^2$ to simplify terms to the form of inside block variance. Highlighting terms in red that become the inside block variance,

$$\begin{aligned}
\sigma_{\text{tot}}^2 &= \frac{1}{B} \sum_{j}^{B} \frac{1}{N_B} \underbrace{\sum_{i}^{N_B}}_{\text{in } j} \left(I_i^2 - 2 I_i \langle I \rangle + \langle I \rangle^2 - 2 I_i \langle I \rangle_j + \langle I \rangle_j^2 + 2 I_i \langle I \rangle_j - \langle I \rangle_j^2 \right) \\
&= \frac{1}{B} \sum_{j}^{B} \frac{1}{N_B} \underbrace{\sum_{i}^{N_B}}_{\text{in } j} \left(\left(I_i - \langle I \rangle_j \right)^2 - 2 I_i \langle I \rangle + \langle I \rangle^2 + 2 I_i \langle I \rangle_j - \langle I \rangle_j^2 \right) \\
&= \frac{1}{B} \sum_{j}^{B} \left(\sigma_j^2 + \frac{1}{N_B} \underbrace{\sum_{i}^{N_B}}_{\text{in } j} \left(2 I_i \left(\langle I \rangle_j - \langle I \rangle \right) - \langle I \rangle_j^2 + \langle I \rangle^2 \right) \right).
\end{aligned} \tag{3.13}$$

Bringing all terms that do not depend on i out of the first sum,

$$\sigma_{\text{tot}}^2 = \frac{1}{B}\sum_j^B \left(\sigma_j^2 - \langle I \rangle_j^2 + \langle I \rangle^2 + \frac{2}{N_B}\left(\langle I \rangle_j - \langle I \rangle\right) \underbrace{\sum_i^{N_B}}_{\text{in } j} I_i \right). \tag{3.14}$$

Note that $\frac{1}{N_B}\underbrace{\sum_i^{N_B}}_{\text{in } j} I_i$ is simply $\langle I \rangle_j$, so we can write

$$\sigma_{\text{tot}}^2 = \frac{1}{B}\sum_j^B \left(\sigma_j^2 - \langle I \rangle_j^2 + \langle I \rangle^2 + 2\left(\langle I \rangle_j - \langle I \rangle\right)\langle I \rangle_j \right). \tag{3.15}$$

With some algebra, we can simplify our expression,

$$\begin{aligned}
\sigma_{\text{tot}}^2 &= \frac{1}{B}\sum_j^B \left(\sigma_j^2 - \langle I \rangle_j^2 + \langle I \rangle^2 + 2\langle I \rangle_j^2 - 2\langle I \rangle_j \langle I \rangle \right) \\
&= \frac{1}{B}\sum_j^B \left(\sigma_j^2 + \langle I \rangle_j^2 - 2\langle I \rangle_j \langle I \rangle + \langle I \rangle^2 \right) \\
&= \frac{1}{B}\sum_j^B \left(\sigma_j^2 + \left(\langle I \rangle_j - \langle I \rangle\right)^2 \right) \\
&= \frac{1}{B}\sum_j^B \sigma_j^2 + \frac{1}{B}\sum_j^B \left(\langle I \rangle_j - \langle I \rangle\right)^2.
\end{aligned} \tag{3.16}$$

Interestingly, the second term on the right hand side is exactly Equation 3.10, the variance between blocks,

$$\sigma_{\text{tot}}^2 = \frac{1}{B}\sum_j^B \sigma_j^2 + \sigma_{\text{btwn}}^2. \tag{3.17}$$

We can interpret the first term as the average of the variances within blocks,

$$\sigma_{\text{tot}}^2 = \left\langle \sigma_{\text{in}}^2 \right\rangle + \sigma_{\text{btwn}}^2. \tag{3.18}$$

Thus, the total variance in the image is average variance inside blocks plus the variance between blocks. Now, we have a direct way to determine how much variance is between blocks, implying uneven illumination.

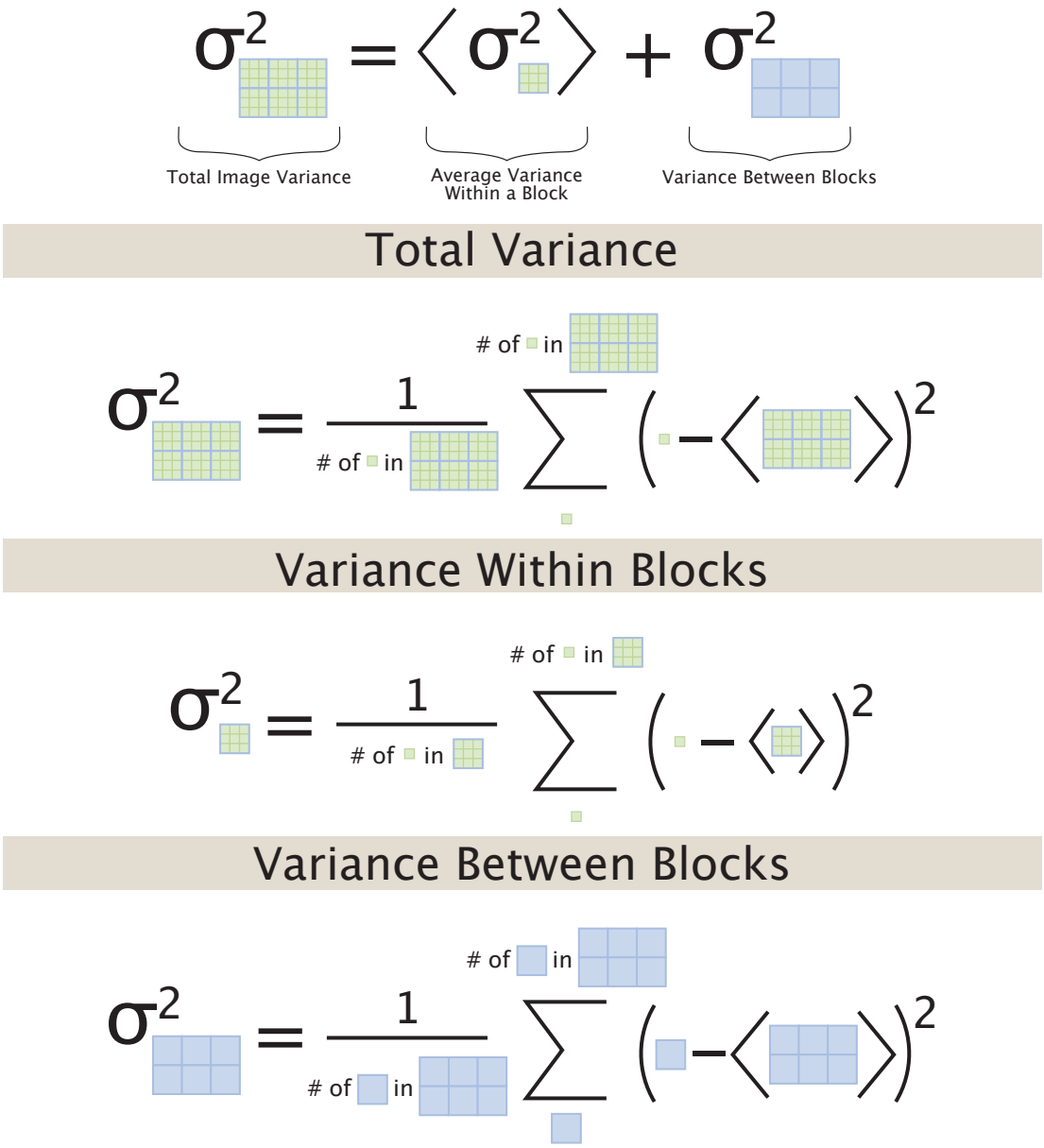

Figure 3.14: **Graphical representation of variance between and within blocks.** The top panel is the equation for the total variance in terms of the variance within a block and between blocks. The subsequent three panels graphically depict the definition of each type of variance, where a single green block represents one pixel, i, and a blue block represents one grid block, j, containing N_{B} pixels.

3.3 Conceivable Geometric and Optical Distortions Arising from 2D Images of 3D Distributions

Monitoring the rapidly changing, and optically labile, chemical reactions driving aster formation with microscopy imposes fundamental technical constraints on our

measurements. Specifically, while asters are formed by molecular motors, microtubules, and ATP arranged in rich three-dimensional structures, imaging these distributions fully in three dimensions over our conditions of biochemical interest would significantly constrain the fastest changes resolvable in these spatial fields. In addition, acquiring 3D data (via many tightly-spaced 2D images in an axial dimension) imposes a significantly larger burden of excitatory photons that can photobleach and further perturb fluorescently-labeled molecules like those we monitor. Consequently, to capture fine changes in aster structure over space and time, the bulk of our measurements are in the form of two-dimensionsal epifluorescence images of developing asters. These images are collected while focused at a central axial plane through the aster.

To interpret this slew of experimental results, in principle, we must account for the difference between our 3D objects of interest and the 2D epifluorescence microscopy images representations of these structures. Here, in the sections that follow, we assess the possible consequences/distortions following from these two-dimensional acquisitions, both conceptually in general, and empirically for our specific imaging conditions. To augur what follows, our analyses largely show that the conceptually-possible differences between two-dimensional data and three-dimensional distributions are in fact empirically negligible, largely due to the narrowness of the optical point spread functions convolving these images compared to the shape of the raw underlying structures we image.

Our discussion that follows proceeds in three parts. First, we consider the ideal case where the optical weighting function along the axial dimension is zero everywhere except the focal plane actually sampled, meaning the acquired 2D image precisely matches the equivalent 3D slice (with no distortion). Second we consider the opposing case where the weighting function is uniform along the axial dimension, resulting in a uniform projection when integrating over each slice in the axial dimension. Lastly, we consider the most realistic case falling between these two limits, where a nonzero, nonuniform, weighting function accumulates fluorescence signal from slices above and below the focal plane, giving a convolution with the signal at the focal plane. In imaging practice, we numerically verify that the narrowness of this weighting function (relative to the objects of interest) makes this case closely approximate the first case of a bona fide slice through the underlying three dimensional distribution.

General form of a 2D image projection

In general, a two dimensional image $\hat{I}(x, y)$ collected at spatial position (x, y) is an integral of a true underlying source profile $I(x', y', z')$ from sources at positions (x', y', z'), where each source is weighted by some optical weighting function $f(x', y', z')$ throughout space,

$$\hat{I}(x, y) = \int_{-\infty}^{\infty} \int_{-\infty}^{\infty} \int_{-\infty}^{\infty} I(x', y', z')\ f(x', y', z')\, \mathrm{d}x'\mathrm{d}y'\mathrm{d}z'. \tag{3.19}$$

Specific imaging cases

In a first ideal case, when the weighting function is simply a Dirac delta function over the axial dimension centered at the focal plane at z, namely $f(x', y', z') = \delta(x - x')\delta(y - y')\delta(z - z')$, the image $\hat{I}^{(1)}(x, y)$ is exactly the corresponding focal slice through the three dimensional profile,

$$\hat{I}^{(1)}(x, y) = \int_{-\infty}^{\infty} \int_{-\infty}^{\infty} \int_{-\infty}^{\infty} I(x', y', z')\ \delta(x - x')\delta(y - y')\delta(z - z')\, \mathrm{d}x'\mathrm{d}y'\mathrm{d}z' \tag{3.20}$$

$$= I(x, y, z). \tag{3.21}$$

In a second opposing case, the image accumulates signal uniformly over sources along the axial dimension, namely $f(x', y', z') = \delta(x - x')\delta(y - y') \times 1$. This gives an image $I^{(2)}(x, y)$ of the form,

$$\hat{I}^{(2)}(x, y) = \int_{-\infty}^{\infty} \int_{-\infty}^{\infty} \int_{-\infty}^{\infty} I(x', y', z')\ \delta(x - x')\delta(y - y')\, \mathrm{d}x'\mathrm{d}y'\mathrm{d}z' \tag{3.22}$$

$$= \int_{-\infty}^{\infty} \mathrm{d}z'\ I(x, y, z). \tag{3.23}$$

When the underlying distributions $I(x, y, z)$ are axially- symmetric or spherically-symmetric ($\equiv I(\rho, \theta)$ or $\equiv I(r)$), such images two dimensional images $\hat{I}$ adopt the forms of Abel transformations [7]. In principle, the underlying $I(r)$ or $I(\rho, \theta)$ can be recovered by an inverse Abel transformation [7, 8] on the measured two-dimensional image $\hat{I}$, though in practice, the numerical success of these schemes is a delicate and often fraught inverse problem.

In a third, intermediate, and most realistic case, we acknowledge that the sources from above and below the focal plane at z can contribute with nonzero weight to the measured signal at z, and also further acknowledge the possible contributions of sources at transverse positions (x', y') distinct from the query position (x, y). Specifically, the optical weighting function of a source at (x', y', z') is a point-spread function (set by the microscope) well modeled as depending only on the displacement $(x - x', y - y', z - z')$ to the query point (x, y). This gives an image $\hat{I}^{(3)}(x, y)$ of the form,

$$\hat{I}^{(3)}(x, y) = \int_{-\infty}^{\infty} \int_{-\infty}^{\infty} \int_{-\infty}^{\infty} I(x', y', z') f(x - x', y - y', z - z') \, \mathrm{d}x' \mathrm{d}y' \mathrm{d}z'. \quad (3.24)$$

Models of the point spread function $f(x-x', y-y', z-z')$ corresponding to circular apertures appropriate for microscope objectives are available [9, 10, 11] to varying levels of analytical and numerical detail, including the popular Born and Wolf model expressed in terms of Airy and Bessel functions. Often a very good approximation to these empirical circumstances is a Gaussian decay factorizable in transverse and axial dimensions with anisotropic widths, namely,

$$f(x - x', y - y', z - z') = \mathrm{psf}_{\mathrm{tr}}(x - x', y - y' | \sigma_{\mathrm{tr}}^2) \times \mathrm{psf}_{\mathrm{ax}}(z - z' | \sigma_{\mathrm{ax}}^2). \quad (3.25)$$

Case Two: Abel Transformation

When the optical weighting function is not purely localized at the focal plane, but instead is uniform throughout the axis of the imaging volume, the distortion of a three-dimensional profile is conceivably appreciable. Image sources at axial positions far away from the focal plane are convolved with sources actually residing at the focal plane, in principle posing an intractable ill-posed inverse problem: there are many different underlying 3D distributions consistent with a given 2D measured image. However, intriguingly, when the underlying distribution $I(x, y, z)$ is spherically-symmetric or axially-symmetric, a measured two-dimensional profile $\hat{I}(\rho, \theta)$ uniquely specifies the original three-dimensional profile, a relationship expressed by the so called Abel transformation and its complement, the inverse Abel transformation. Here, we explicitly describe how a radially-symmetric image (e.g., of spherically-symmetric aster) manifests a two dimensional projection forming an Abel transformation, under this pessimistic scenario when the optical weighting function does not decay away from the focal plane as rapidly as expected from epifluorescence microscopy. We also remark on qualitative features that can be analytically shown to survive in such a two dimensional uniformly-weighted projection. We provide this discussion to give maximally conservative statements about how

two dimensional images still report on key features of three dimensional structures, even in the counterfactual setting where distant image sources are weighted equally to those appearing on the focal plane.

Imagining a 3D, spherical aster where we possess an omniscient knowledge of the concentration profile, we ask what will be the concentration profile reported by a microscope 2D image? To solve, we integrate the height, over z (in cylindrical coordinates), of a skyscraper cutting through the aster sphere. For a given skyscraper address with cylindrical coordinates (ρ, θ), we calculate the concentration of the image pixel value corresponding to the skyscraper,

$$\hat{I}(\rho, \theta) = \int_0^h dz\, I(\rho, \theta, z). \tag{3.26}$$

Since there is radial symmetry in θ, we can remove the θ dependence in the integral such that,

$$\hat{I}(\rho) = \int_0^{2\pi} d\theta \int_0^h dz\, I(\rho, z) = 2\pi \int_0^h dz\, I(\rho, z). \tag{3.27}$$

We now change to spherical coordinates, rather than cylindrical, since we consider the aster to be a sphere. Thus, the concentration as a function of r, which depends on ρ and z, can be written as,

$$\hat{I}(\rho) = 2\pi \int_0^h dz\, I(r(\rho, z)). \tag{3.28}$$

Since for a given skyscraper ρ is constant, we can change the integration variable from z to r with the equation,

$$r^2 = \rho^2 + z^2. \tag{3.29}$$

Differentiating with respect to r,

$$2r = 2z\frac{dz}{dr} \Rightarrow dz = \frac{r}{z}dr. \tag{3.30}$$

Using the substitution, $z = \sqrt{r^2 - \rho^2}$,

$$dz = \frac{r}{\sqrt{r^2 - \rho^2}}dr. \tag{3.31}$$

Thus, the concentration at a given 2D image radius, ρ of a 3D aster is,

$$\hat{I}(\rho) = 2\pi \int_\rho^{\sqrt{\rho^2+h^2}} dr\, I(r)\frac{r}{\sqrt{r^2 - \rho^2}}. \tag{3.32}$$

As a sanity check, we can ensure that a uniform concentration in 3D, $I(r, \theta, \phi) = I_0$ is still uniform in 2D. Plugging this constant into equation 3.34,

$$\hat{I}(\rho) = 2\pi I_0 \int_{\rho}^{\sqrt{\rho^2+h^2}} dr \, \frac{r}{\sqrt{r^2 - \rho^2}}, \tag{3.33}$$

and performing a u-substitution where $u = \sqrt{r^2 - \rho^2}$ and $du = r/\sqrt{r^2 - \rho^2}$,

$$\hat{I}(\rho) = 2\pi I_0 \int_0^h du = 2\pi I_0 h. \tag{3.34}$$

We can ensure that if we simply integrated over a constant sample from the perspective of the microscope, we would obtain the same constant,

$$\hat{I}(\rho, \theta) = \int_0^h dz \, I_0 = I_0 h, \tag{3.35}$$

and assuming spherical symmetry,

$$\hat{I}(\rho) = \int_0^{2\pi} d\theta \, I_0 h = 2\pi I_0 h. \tag{3.36}$$

The transform defined in equation 3.34, is called an Abel Transform, and has an analytical inverse function, under the condition that $I(r) \to 0$ faster than $\frac{1}{r}$ [8].

3.4 Empirical Deconvolution on an Aster

Here we acknowledge the contributions of intensity signals from nearby pixels on a queried pixel as directed by a finite width point spread function. The majority of data in this study analyzes 2D images that pass through the aster center. Figure 3.15 depicts an image of this type. In analyzing the intensity "smearing" that occurs from neighboring pixels, it is important to not only evaluate the contribution of other pixels in the same plane but also pixels in planes above and below the pixel of interest. In this section, we evaluate how the results of deconvolution on 3D image stacks of an aster modify the intensity value of the resultant image. We acquire images of an aster motor distribution every 0.5 μm in the axial direction. We then perform a deconvolution procedure using an ImageJ plugin, Deconvolution Lab2 [9], employing the Richardson-Lucy deconvolution method. As inputs, we provide an image or image stack and also a point spread function. For circular apertures, the point spread function has been shown to be an Airy function [10]. However, for ease of use, practitioners often approximate these functions with a Gaussian. We demonstrate the results of deconvolving with both of these methods.

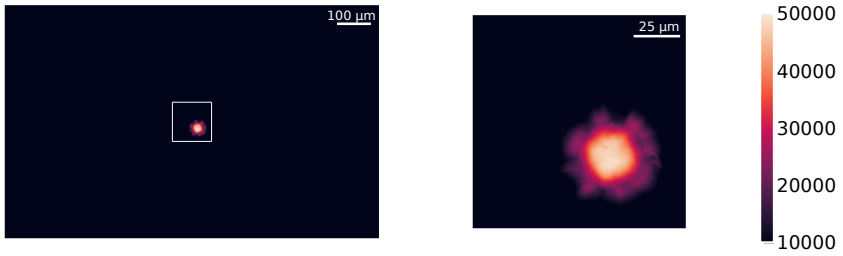

Figure 3.15: **Image of the center of an aster for deconvolution.** As an example image for deconvolution, the center plane of a z-stack of a fully formed aster is shown. On the left, the full figure dimensions are shown, while on the right, a cropped view of the center of the image is shown, corresponding to the white square on the left. We note the aster is not perfectly centered within the image which is typical for asters as they dynamically form. Our deconvolution method needs to work regardles of the aster centering.

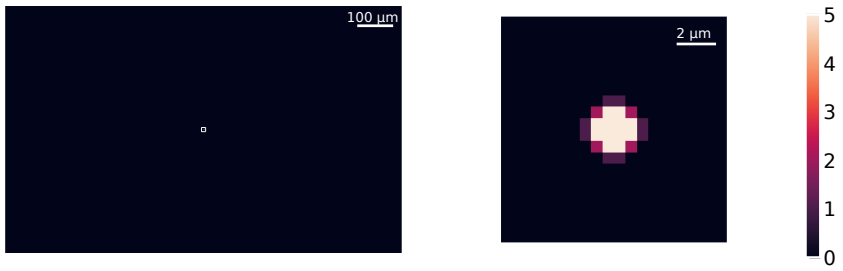

Figure 3.16: **Generated Airy point spread function.** Using the PSF Generator in ImageJ with the Born and Wolf 3D model, we have created a point spread function based on our microscope's optical parameters. The images here are the center slice of the 3D PSF where the left shows the full size of the image and the right is cropped to the center to show the bright center of the PSF.

We generate an Airy PSF using an ImageJ PSF Generator plugin [12]. The plugin requests as inputs the refractive index, which we set to 1 for an air objective, the wavelength of light, which we input as 480 nm, the numerical aperture of the objective, which we set to 0.45, and the nanometer to pixel conversions in each dimension, which for the x and y dimensions, we take to be 578 nm/px and for the z dimension we use 500 nm/px. In Figure 3.16 we show an example of the Airy PSF at the center plane.

Using Deconvolution Lab2, we perform 50 iterations of Richardson-Lucy deconvolution, at first only in 2D, on the sample image shown in Figure 3.15 and deconvolve with the Airy PSF shown in Figure 3.16. In Figure 3.17(A) we show the result of this deconvolution when implemented this way. In Figure 3.17(B) we plot the trace

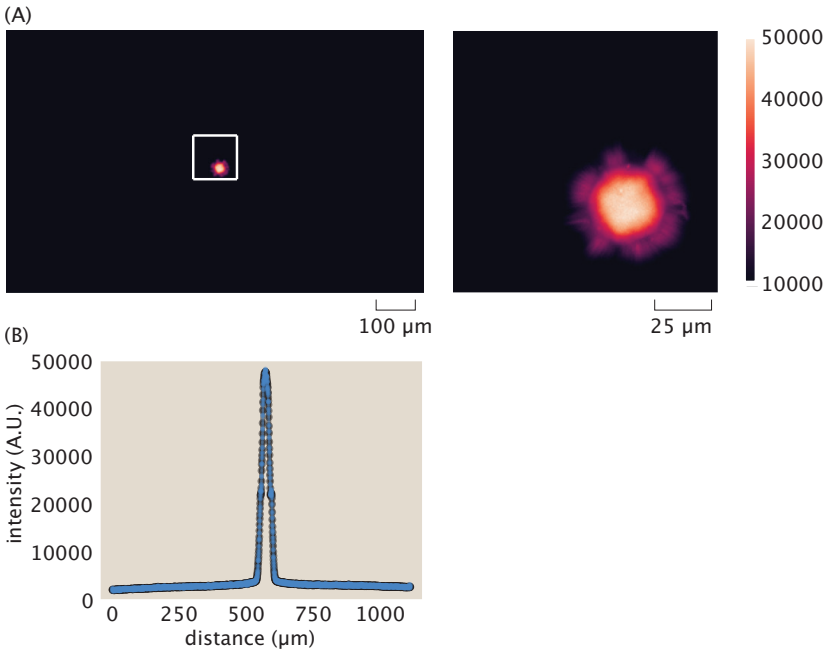

Figure 3.17: **Deconvolving using an Airy PSF in ImageJ reveals a similar output to the raw image input.** (A) The full deconvolution output and cropped deconvolution output are depicted. (B) Taking a cut line through the center of the aster for both the raw image (in black) and the deconvolved output (in blue), we find near perfect agreement in intensity signal. This indicates that the convolution done by the microscope had very little effect on the image.

of a cut line through the center of the aster for the initial raw image in black and the Fiji deconvolved Airy PSF in blue. We find that this deconvolution returns a value practically identical to the raw image trace.

Complementary to using the Airy function, we explore the results of using a Gaussian as already described earlier in the context of synthetic data. In Figure 3.18 we fit the length parameters for the Gaussian to the Airy PSF generated in ImageJ and find that the transverse direction has a length scale of $\sigma_{\text{tr}} = 0.33\ \mu$m and the axial dimension has a length scale of $\sigma_{\text{ax}} = 2.32\ \mu$m. These characteristic widths, and the conceit of Gaussian approximations, to the point spread function are highly consistent with reported values and procedures in related literature; e.g., references [13, 14] report similar widths of $0.3 \sim \mu$m to the transverse character of experimental point spread functions under related conditions.

Upon deconvolving with the Gaussian point spread function, as shown in Figure 3.19, the output again appears nearly identical to the raw image as shown in Figure 3.15.

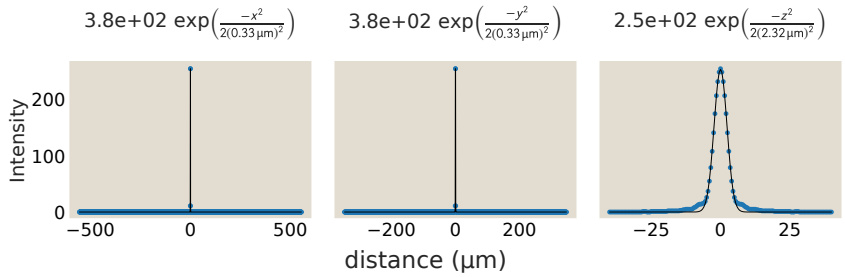

Figure 3.18: **Gaussian length scales are determined by fitting the generated Airy point spread function.** Gaussian functions provide a very good fit to the decay of the point spread function in space. The transverse plane has a small length scale, only 0.33 μm, while the axial direction has a longer, but still small length scale of 2.32 μm.

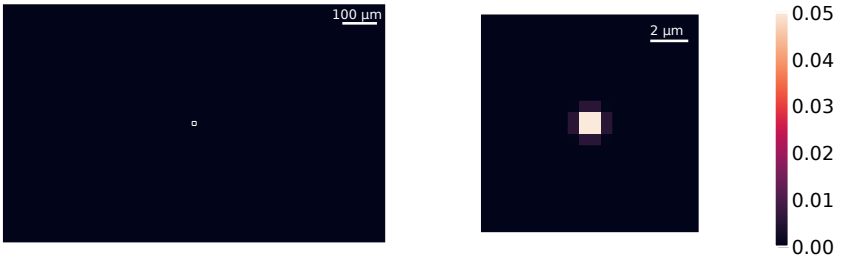

Figure 3.19: **GaussPSF with length scales as determined by the Airy function fits.**

These tests of 2D deconvolutions give us a sense that any effect of convolution by the microscope is minimal. However, it is important to check modifications created by convolutions in the axial dimension, especially since this is the widest dimension of the point spread function, as can be seen in Figure 3.18. To this end, we perform 100 iterations of Richardson-Lucy deconvolution for both the generated Airy PSF and the fit Gaussian PSF. Again, we plot the cut lines through the center of the aster in Figure 3.21 and find little deviation from the raw image. The Gaussian deconvolution again looks identical to the raw image, but for the Airy deconvolution, there is a slight difference at the center of the aster. Here, the Airy deconvolved output produces higher intensities in the aster core and becomes less smooth.

Rather than taking a cut line, we also plot the polar averages of the images centered about the aster with respect to the aster radius shown in Figure 3.22. Once again, we largely see agreement with the raw images. The 3D airy deconvolution is again the only deconvolved output that show any difference with an increased intensity at the aster center.

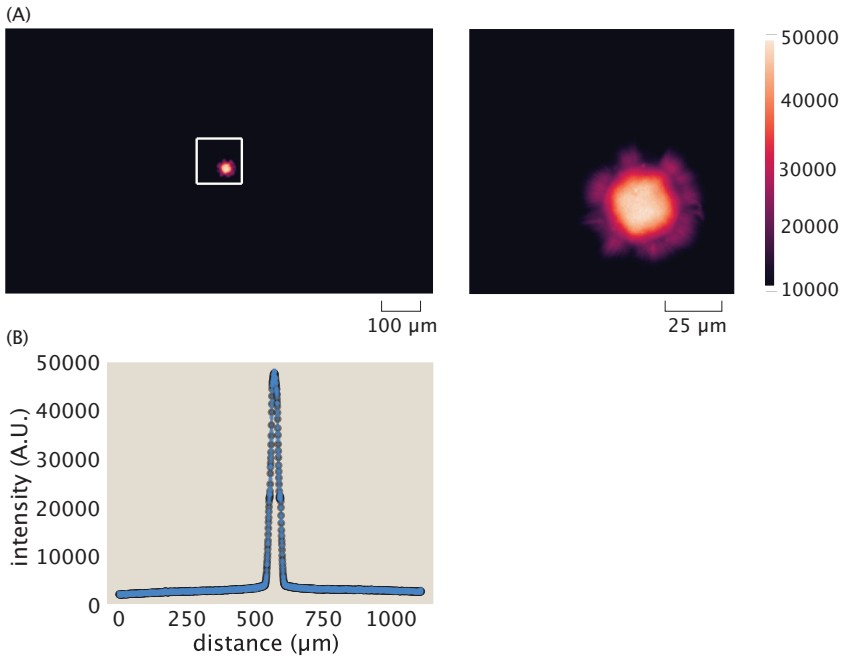

Figure 3.20: **Deconvolving using a Gaussian PSF reveals a similar looking output to the raw image input.** (A) The full deconvolution output and cropped deconvolution output are depicted. (B) Taking a cut line through the center of the aster for both the raw image (in black) and the deconvolved output (in blue), we find near perfect agreement in intensity signal. This indicates that the convolution done by the microscope had very little effect on the image.

Having learned that the quantitative impact of deconvolution in two or three dimensions in real aster images of interest is extremely numerically modest, we now explicitly verify that the ambient background level of fluorescence signal does not change the (small) impact of deconvolution. Figure 3.23 compares how performing background subtraction before or after deconvolution affects the recovered fluorescence profiles. The raw, deconvolved, and background-subtracted then deconvolved traces of Figure 3.23(A) agree up to the background offset, and very small numerical noise. This agreement, arguing that deconvolution and background subtraction largely commute numerically, shows that the presence of an ambient signal background in real aster images leaves the result of deconvolution essentially unchanged (up to exactly the background offset). We further visualize this agreement in Figure 3.23(B) by plotting the difference between the deconvolved image $D[I]$ and the background-subtracted then deconvolved image $D[I - \langle I_{\text{bg}} \rangle]$, relative to the background level $\langle I_{\text{bg}} \rangle$. Over the central line profile of the aster, this difference is very close to unity throughout the image, namely $\frac{D[I]-D[I-\langle I_{\text{bg}} \rangle]}{\langle I_{\text{bg}} \rangle} \approx 1$.

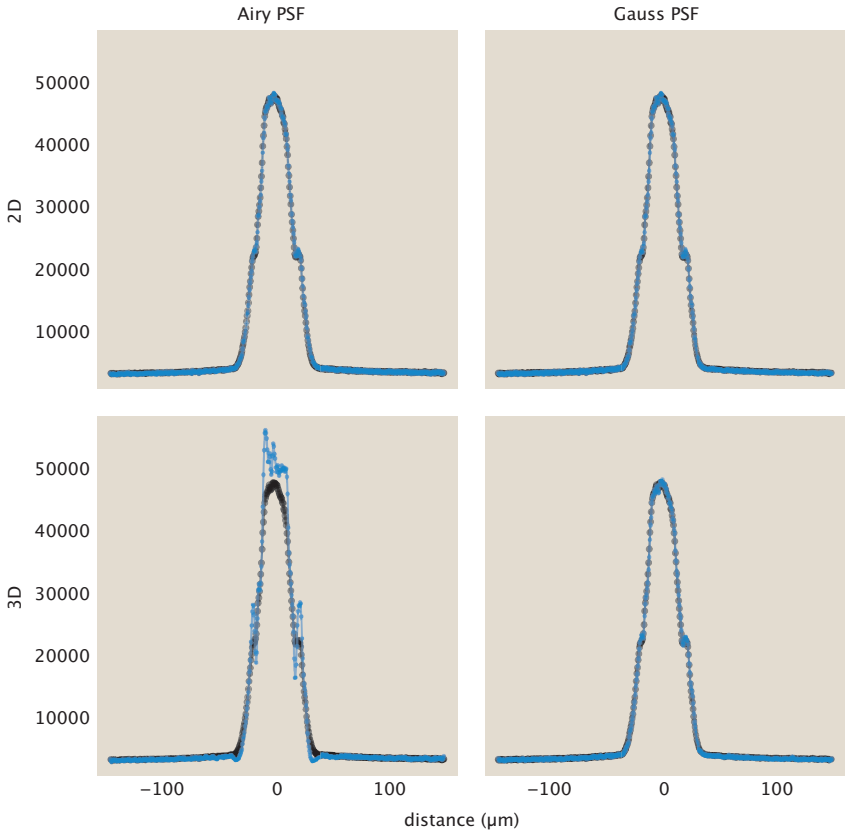

Figure 3.21: **3D deconvolution in ImageJ for Airy or Gaussian PSFs show little deviation from the original image.** For all plots, we include the raw image intensity cutline in black and the deconvolved cutline in blue. The top row highlights the ImageJ 2D deconvolutions while the bottom row highlights their 3D counterparts.

This finding that a background does not nontrivially modify the result of deconvolution (for relevant aster data of interest) complements generic numerical guarantees applying to Richardson-Lucy deconvolution. Studying the deconvolution operation in the context of astronomical images, Prato and coworkers [15] establish that performing Richardson-Lucy deconvolution conserves intensity flux both locally and globally in input images, when the background of the image is zero. Our numerical analysis suggests that the latter proviso that background is zero may not be required for these algorithms on our class of data.

In sum, we find deconvolving has little to no impact on the image. This is especially clear in Figure 3.22 where only the 3D Airy deconvolution shows any discrepancy between the raw and deconvolved images. And even here, there is a maximum of approximately a 10% difference between the intensity values within 15 μm of the aster center. Based on these results, we do not find it imperative to include a

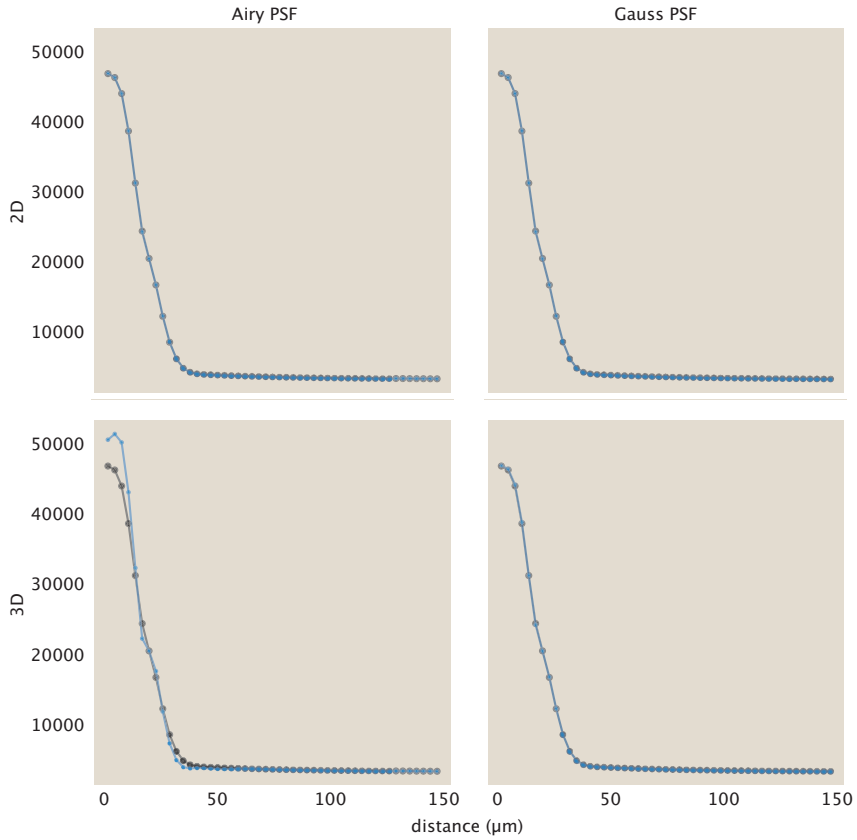

Figure 3.22: **Polar averaging deconvolved outputs also largely agree with the raw polar averages.** We take the averaged intensity of volume normalized radial shells and plot how the intensity changes with respect to the distance from the aster center. In black, we show the traces of the raw image and in blue the traces of the deconvolved output. Largely, the deconvolved images in both 2D, on the top row, and in 3D, on the bottom row, match the raw image.

deconvolution procedure when analyzing aster data.

3.5 Effects of Convolution on Image Formation

We were curious to better understand why the deconvolution algorithms led to very modest changes in our measurements. To investigate these questions more deeply, in this section, we examine synthetic data that we subject to the deconvolution procedure to dissect the physics of the deconvolution process.

As noted in the previous section, the formation of an image in a microscope includes convolution with the microscope's point spread function. The point spread function provides a mathematical description of how light from a point source is affected by diffraction and other optical limitations as it passes through the optical path of the

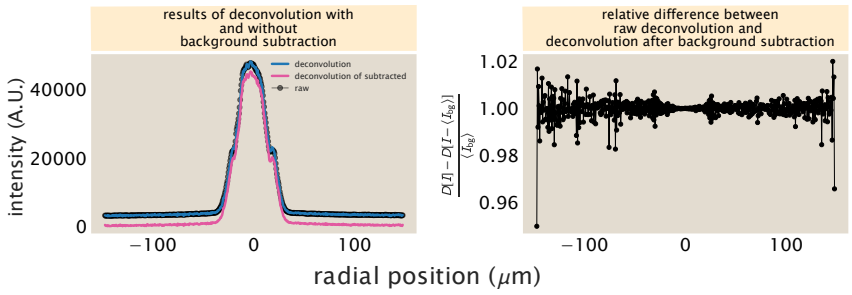

Figure 3.23: **Subtraction of ambient background fluorescence leaves deconvolution results unchanged**. (A) Profiles (slices) of fluorescence along a a line through an aster's center before deconvolution (in black, denoted I); after deconvolution (in blue, denoted $\mathcal{D}[I]$ where $\mathcal{D}$ is the deconvolution operation); and when deconvolution is performed after the ambient $\langle I_{\text{bg}} \rangle$ average level of fluorescence in the regions of space outside the aster is subtracted, $\mathcal{D}[I - \langle I_{\text{bg}} \rangle]$,shown in pink. These traces affirm that the subtraction of ambient fluorescence before or after deconvolution does not affect the shape of the intensity fluorescence profile. These deconvolutions were performed in two dimensions using an Airy-function based point-spread function in DeconvolutionLab2 (via Imagej), as described above. (B) The difference $\frac{D[I]-D[I-\langle I_{\text{bg}} \rangle]}{\langle I_{\text{bg}} \rangle}$ of the blue and black traces in panel (A) relative to the ambient $\langle I_{\text{bg}} \rangle$ level of fluorescence. The fact that this value is consistently very close to unity affirms that $D[I] - D[I - \langle I_{\text{bg}} \rangle] \approx \langle I_{\text{bg}} \rangle$, namely that the background subtraction operation is essentially commutative with respect to deconvolution.

microscope. This convolution causes the resultant image to appear smoother, or blurred, compared to the object itself. As this work measures the number of ATPs at a given location in time via fluorescence, it is important to determine how the PSF spreads and attenuates fluorescence signal, affecting the apparent localization and intensity of ATPs. To get a feeling for the impact of convolution, we mimic the image acquisition procedure on synthetic data. In particular, we specify a symmetric sphere of fluorescent motor proteins whose concentration decays radially. We model the motor concentration field using an exponential decay corresponding to the object

$$\text{obj} = \exp\left(\frac{-\sqrt{x^2 + y^2 + z^2}}{\lambda_o}\right), \tag{3.37}$$

where λ_o is the decay length, which we take to be $\approx 30\,\mu$m for a fully formed aster. For convenience, we do not normalize the object, ensuring that at the origin the intensity value is one.

Our first objective is to explore how convolution modifies the "measured" intensities. To perform a convolution mimicking the imaging process in the microscope, we define a point spread function as a 3D Gaussian. We assume that the point spread

function has different length scales in the transverse (x-y) plane compared to the axial (z) direction. The form of our synthetic point spread function is

$$\mathrm{psf}(x,y,z) = \mathrm{psf}_{\mathrm{tr}}(x,y)\times\mathrm{psf}_{\mathrm{ax}}(z) = \frac{1}{2\pi\sigma_{\mathrm{tr}}^2}\exp\left(\frac{-(x^2+y^2)}{2\sigma_{\mathrm{tr}}^2}\right)\times\frac{1}{\sqrt{2\pi\sigma_{\mathrm{ax}}^2}}\exp\left(\frac{-z^2}{2\sigma_{\mathrm{ax}}^2}\right). \tag{3.38}$$

We estimate the length scale for the transverse point spread function based on the minimum resolvable distance. For a self-luminous light source of incoherent light, which encompasses fluorescent signals, the minimum distance is

$$\sigma_{\mathrm{tr}} \approx \frac{0.61\lambda}{\mathrm{N.A.}}, \tag{3.39}$$

where λ is the wavelength of light and N.A. is the numerical aperture [10]. For our setup, we use a wavelength of 513 nm and our objective has an N.A. of 0.45. These parameters yield the transverse length scale,

$$\sigma_{\mathrm{tr}} = \frac{0.61\times 513\ \mathrm{nm}}{0.45} = 695\ \mathrm{nm} \approx 0.7\,\mu\mathrm{m}. \tag{3.40}$$

For the axial length scale, we compute the depth of focus as

$$\sigma_{\mathrm{ax}} \approx \frac{\lambda\, n}{\mathrm{N.A.}^2}, \tag{3.41}$$

as stated in [16], where n is the index of refraction, which we take as $n = 1$ for an air objective. Plugging in values, we estimate

$$\sigma_{\mathrm{ax}} \approx \frac{0.513\ \mu m\times 1}{(0.45^2)} \approx 2.5\ \mu m. \tag{3.42}$$

Now that we have the parameters describing the point spread function in hand, we now turn to examining its effects. The convolution of the object with the point spread function is characterized by the integral

$$\mathrm{im}(x,y,z) = \int_{-\infty}^{\infty}\int_{-\infty}^{\infty}\int_{-\infty}^{\infty}\mathrm{obj}(x',y',z')\mathrm{psf}(x-x',y-y',z-z')\,\mathrm{d}x'\mathrm{d}y'\mathrm{d}z' \tag{3.43}$$

which amounts to weighting each point in the image with all points in the object, each appropriately multiplied by the point spread function itself.

We use the scipy package, *scipy.signal.convolve* to perform this convolution. We set the "mode" keyword argument to "same" which ensures the returned convolved matrix has the same size as the inputted object. The microscope would acquire an image that reflects the center slice of the convolution. We compare the center slice

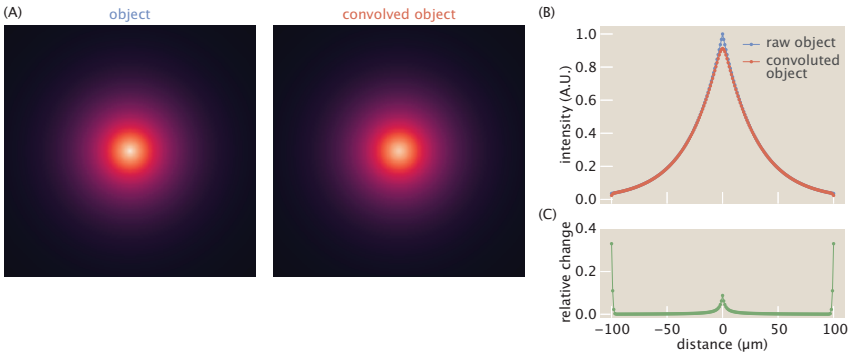

Figure 3.24: **Exploring the effects of convolution with the point spread function for synthetically generated data.** (A) Images of the center plane for both the raw object, a radially decaying exponential sphere of motors, and the convolved image with a Gaussian point spread function. (B) More quantitatively, we plot the intensity of both the object and convolved object along a cut line passing through the object origin. (C) We find most of the relative change, as defined as $\frac{\text{obj}-\text{obj}\star\text{psf}}{\text{obj}}$, occurs in the center of the object. The peaks at the ends are due to edge effects in the convolution.

of the synthetic specified object and the convolved object in figure 3.24(A). By eye it is difficult to distinguish the two slices from one another. To be more precise, we draw a cutline through the center of the object as depicted in figure 3.24(B). The difference after convolution is still quite minimal, though we do see a difference near the center such that the convolved image becomes smoothed and has a lower intensity value. We demonstrate the relative change in figure 3.24(C) as the difference of the convolved object from the raw object divided by the raw object,

$$\Delta I = \frac{\text{obj} - \text{obj} \star \text{psf}}{\text{obj}}. \tag{3.44}$$

There is about a 10% change in the signal at the center of the object and very little change beyond 10 μm outside the center. The spikes at the ends of the plot are due to edge effects occurring from convolution.

The variation in the image intensity as a result of the convolution with the point spread function appears to be minimal, and is only noticeable at the very center. This begs the question: how necessary is incorporating the corrections due to the point spread function in the analysis of our images, and specifically, how will this procedure alter our measured concentrations? To that end, we perform a sweep of sigma values to determine at what Gaussian length scales convolution significantly alters the intensity reported in the image as contrasted with the intensity of the object.

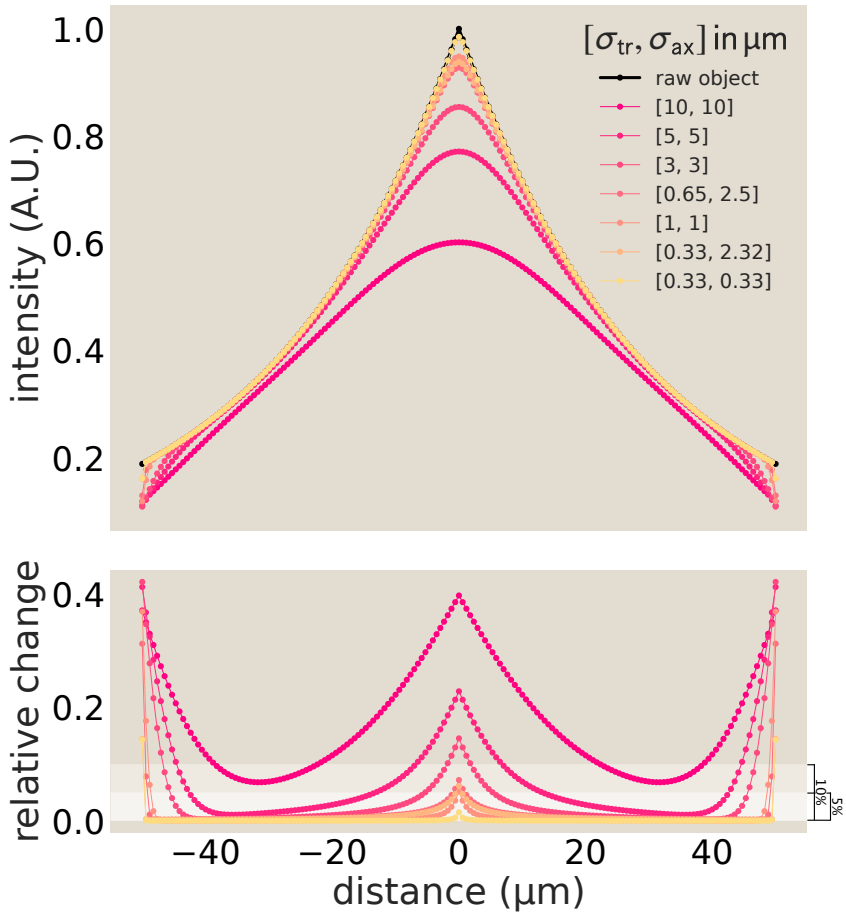

Figure 3.25: **Comparison of object and object convoluted with Gaussian point spread function.** (A) The profile of the synthetic object is plotted in black with convolved "images" with varying PSF length scales overlayed. For small length scales, $\sigma < 3\,\mu$m, the "image" does a good job of approximating the object. The discrepancies are highlighted in (B) where we plot the relative change between the image and object. Most of the variation occurs in the center. Increases at the edges are thought to be boundary effects.

From the data reported in figure 3.25, we find that when convolving with small σ values ($\sigma \leq 3\,\mu$m), the resultant traces are very similar to the original object. The bottom plot gives the relative change of the intensity values after convolving as described in equation 3.44. Except for the edges of the plot, where we believe boundary effects create increases, convolutions with small σ values reveal discrepancies of under ten percent.

3.6 Probe Blurring

It is important to take into account the on/off times of ATP to the ATP reporter to understand how reported ATP gradients may be affected by the probe. We can do an estimate to determine how far a probe can travel while bound to an ATP. We estimate the diffusion constant of the ATP probe to be $D = 45\,\mu\text{m}^2/\text{s}$ in section 3.11. We then need to take into account the binding rates for the ATP reporter. We use the reporter Queen-7μ A81D which has a reported dissociation constant of $K_\text{d} = 7.02 \times 10^{-2}$ mM [17]. The on and off rates for this mutant is not listed, however, the authors do list the rates for other mutants. Queen-2m has a reported on rate of $k_\text{on} = 2.7 \times 10^{-2}\,\text{mM}^{-1}\text{s}^{-1}$ and an off rate of $k_\text{off} = 9.4 \times 10^{-2}\,\text{s}^{-1}$ [18]. Queen-37C has a reported on rate of $k_\text{on} = 3.5 \times 10^{-2}\,\text{mM}^{-1}\text{s}^{-1}$ and an off rate of $k_\text{off} = 1.7 \times 10^{-1}\,\text{s}^{-1}$ [2]. Based on these reported off rates, the bound time of an ATP to a probe is roughly,

$$t_\text{b} = \frac{1}{k_\text{off}} = \frac{1}{0.1\,\text{s}^{-1}} \approx 10\,\text{s}. \tag{3.45}$$

Given that we image the aster every 20 s, the bound time is long. The distance the probe can travel during the bound time of ATP is on the order of

$$l_\text{b} = \sqrt{Dt_\text{b}} = \sqrt{45\,\mu\text{m}^2/\text{s} \times 10\,\text{s}} \approx 20\,\mu\text{m}. \tag{3.46}$$

This length scale is also long since the gradients we measure are also on the order of few $\times\, 10\,\mu$m. Thus, diffusing probes bound to ATP could contribute to a significant smoothing of gradients as bound probes diffuse.

To better understand this, we can write a model for the ATP bound probes over space and time. In this model, we take into account the diffusion of bound probes, the dissociation of the ATP to the probe, and the binding of an ATP to the probe,

$$\frac{\partial Q_\text{b}}{\partial t} = D\nabla^2 Q_\text{b} - k_\text{off} Q_\text{b} + k_\text{on} Q_\text{b} A. \tag{3.47}$$

3.7 Finite Element Simulations of Continuum Models

Our work is predicated on an interplay between experimental measurements and a theoretical description of our results. As seen in the main body of the paper, we have considered an elementary reaction-diffusion model that describes the spatiotemporal evolution of ATP as a result of the consumption of ATP by the motors as well as the diffusion of ATP.

Although the equations are simply stated, for the case in which the motor distribution is varying in space and time, the solution of these equations is prohibitive except in

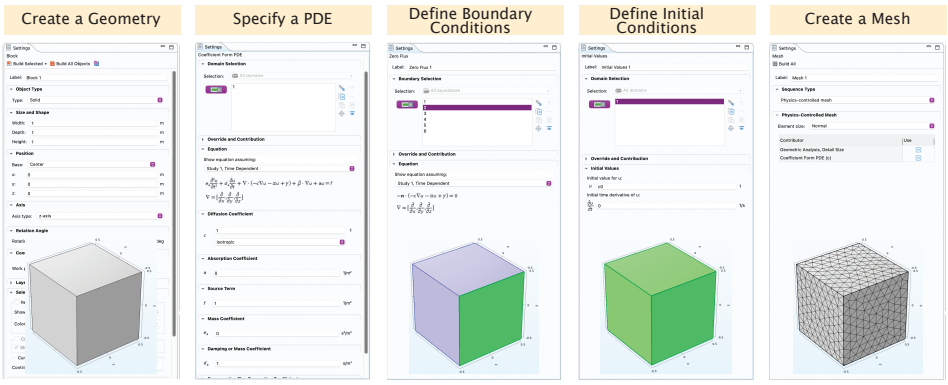

Figure 3.26: **Setting up a finite element calculation in COMSOL.** The use of COMSOL is dependent upon a series of steps that in total make it possible to solve some partial differential equation of interest. The five columns show how to create a geometry, specify which partial differential equation we are solving, how to define boundary conditions and initial conditions and how to set up the finite element mesh.

the most highly idealized circumstances. As a result, we were interested in having a robust numerical approach to solving the continuum equations describing our experiments, including the effects of photobleaching, in the context of the complex geometry of our microscope coverslips and optically activated aster regions.

To that end, in several different contexts we used the finite element method to carry out numerical solutions of our reaction-diffusion-photobleach equations. Part of the power of the finite element method is that it allows us the flexibility to consider arbitrary geometries and to quickly move between different effects by tuning the relevant partial differential equations. In particular, we have used the commercial finite element software known as COMSOL. As seen in Figure 3.26, to carry out a simulation of interest, we need to set up the calculations by describing the geometry, choosing which partial differential equations to solve, what the boundary and initial conditions are and how to mesh our region of interest.

In the main body of the paper, we showed how the finite element method was used to compute the depletion over time of ATP as a result of a gradient in the distribution of motors. Later in the SI, we will discuss how we used the finite element method to make careful simulations of how photobleaching might have influenced our measurement of the ATP concentration.

3.8 Photobleaching

From an experimental perspective, one of the main objectives of the present work is to determine the concentration of ATP at different positions and times within our microtubule-motor system. However, since our method of making that measurement uses fluorescence, it is incumbent upon us to quantify the unwanted effects of photobleaching, which leads to a reduction in fluorescent signal, as opposed to the physical reduction we are really interested in due to ATP consumption.

To understand and account for the character and extent of photobleaching affecting our measurements, we consider these dynamics from several angles. First, we perform control experiments quantifying the intensity reduction in a uniform mixture of fluorescent ATP probes absent any motor activity. We understand the quantitative phenomenology reported by these experiments by building models accounting for the role of a reservoir outside the excitation region, both via simple kinetic and finite element modeling.

Phenomenology of Photobleaching from Control Experiments

We prepare an ATP calibration experiment, as described in section 3.1, such that we pipette a fixed, known quantity of ATP into the same reaction mixture as an aster experiment; however, we do not include motor proteins, thereby preventing any ATP hydrolysis from occurring. We then image the sample using the same time dynamics as aster experiments, namely matching laser intensity currents, 1000 mA, exposure times, 150 – 160 ms, and the interval between image acquisition, 20 s. Upon collecting image data, we process it using the pipeline described in section 3.2 to do background subtraction (section 3.2) and uneven illumination corrections (section 3.2). We then average the intensity value of each image and plot the intensity values over time. This produces scatter plots such as those shown in Figure 3.27. We see empirically from the lines in Figure 3.27 that photobleaching in our system is very well described by fitting a single exponential plus a constant of the form

$$f_p(t) = \frac{I(t)}{I_0} = (1 - I_\infty)e^{-t/\tau} + I_\infty, \tag{3.48}$$

where $I(t)$ is the intensity at time t, I_0 is the intensity at the start of the experiment, I_∞ is the intensity as time approaches infinity, and τ is the characteristic decay constant in time.

To fit this decay due to photobleaching, we first divide all data points by the initial value of the intensity, I_0, which, for a strictly monotonic function, is the

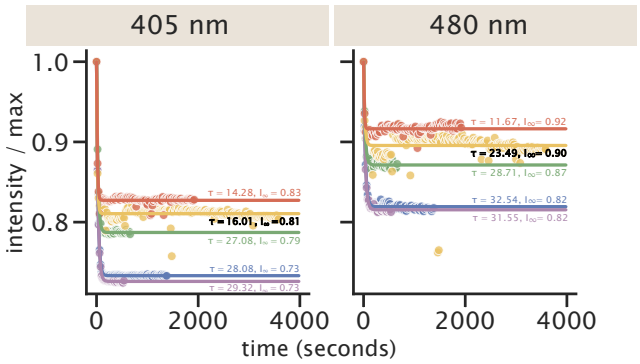

Figure 3.27: **Examples of representative, appreciably-variable, raw photobleaching trajectories across (putatively-identical) experiments, and accompanying fits.** Fluorescence intensities $I(t)$ of 405 nm (left column) and 480 nm (right column) excitation channels were each fit adequately to an exponential decay, Equation 3.48, with a single timescale τ and a long-time offset I_∞ (once normalized by maximum intensity values at time zero, I_0). Lines show best-fit curves and dots are raw data. Each color represents an experimental repeat for data taken at $500\mu M$ ATP and at 20 s intervals.

maximum value of the data. Thus, we pin the time zero intensity to 1. Using scipy.optimize.minimize, we find the parameter set, $\underline{p} = (p_0, p_1, \ldots, p_n)$, for a fitting function, $f_p(t)$, that minimizes the sum of the square of the residuals,

$$\text{SSR} = \sum_t (I(t) - f_p(t))^2, \tag{3.49}$$

where $I(t)$ is the value of the intensity at a time t. From here on, we will define the variables of the parameter set such that $p_0 = \tau$, $p_1 = I_\infty$.

Why does photobleaching adopt this form of an initial exponential decay to a plateau of about 80% of the initial intensity? Ordinarily, photobleaching in a uniformly-illuminated, confined chamber could instead be modeled by a single exponential decay,

$$f_p(t) = e^{-t/\tau}, \tag{3.50}$$

since the only thing that could change the state of the probe is bleaching according to the dynamical equation,

$$\frac{dI}{dt} = -\frac{1}{\tau} I. \tag{3.51}$$

However, our situation is more nuanced because the excitation region is small compared to the size of the chamber, meaning non bleached probes can diffuse in, slowing the time scale of intensity decay. We show that a single exponential indeed fits poorly to our data in Figure 3.28(A). But, as we commented before in

Eq. 3.48, a single exponential plus a constant seems to do the trick. One may be concerned about whether this model is physically reasonable since at sufficiently long timescales, the underlying physical picture would still expect that all the probes to have been bleached. To reckon with this question, in section 3.8, we show that when diffusive replenishment is invoked in a first order kinetic model where probes adopt two (bleached or unbleached) states, the decay of visible (unbleached) probe is modeled by a double exponential,

$$f_p(t) = (1 - I_\infty)e^{-t/\tau} + I_\infty e^{-t/\tau_2}, \tag{3.52}$$

where τ_2 is a second emergent timescale in the physical problem. If this second time constant τ_2 is very long, the behavior describing the photobleaching dynamics is well approximated by a single exponential plus a constant. In Figure 3.28(C), a double exponential fit seems to fit just as well as a single exponential plus a constant as shown in Figure 3.28(B). However, we note that the the solver kept the initial guess for τ_2, the long decay constant. In adjusting initial guesses and solver tolerances, we conclude that experimental data do not offer sufficiently long time courses for the solver to get a good fit for this parameter. However, we do know it is much much longer than the timescale of our experiment. Indeed, in Figure 3.29, we show that for $\tau_2 > 3 \times 10^5$, the squared sum of residuals for most replicates have reached a plateau and there is no further refinement of this parameter to achieve. If our experiment contained data at much longer times, we could more clearly witness the effect of the second decay constant.

Sensitivity of photobleaching to experimental conditions

When correcting for photobleaching in aster data, one of the things we need to check is if the photobleaching decay fits vary with ATP concentration. In Figure 3.30, we plot the fit parameters as a function of ATP concentration. There is no clear trend with ATP, indicating that the probe photobleaching process is not ATP-concentration dependent. Thus, regardless of an aster's ATP concentration, we can process images using appropriate globally-inferred parameters to the photobleaching decay curves.

We also examine how the fit parameters scale with modulating the time interval between light excitations. We expect that for shorter times between pulses, the bleaching of probes will be more continuous leading to shorter decay constants, while for longer intervals between light pulses the time constant should take much longer to see reduction in light intensity, which we have simulated in section 3.8. In Figure 3.31, we find the decay constant, τ, scales about linearly with the interval be-

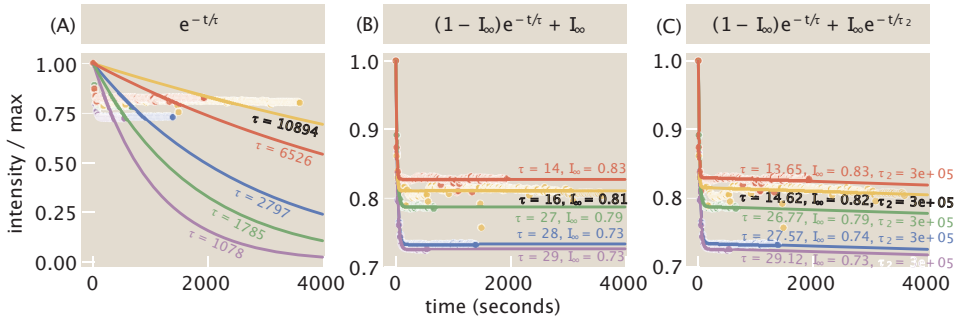

Figure 3.28: **Photobleaching data fit to several functional forms.** (A) Single exponential fits do not do an acceptable job of capturing the intensity depletion due to photobleaching and lead to large values of the decay constant. (B) Fitting to a single exponential plus a constant provides a satisfactory fit to the form of measured intensity reduction. (C) A double exponential plus a constant also fits the measured intensity decline, though the solver does not capture the second, longer decay constant very well. All data in these plots are taken at 500 μM ATP and at 20 s intervals. Each color represents the data from the same experimental repeats as depicted in Figure 3.27. Values for τ and τ_2 have units of seconds and values for I_∞ are unitless, since the intensities are normalized by the maximum intensity I_0 at time zero.

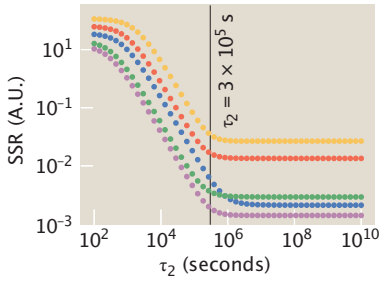

Figure 3.29: **Evaluation of fit for a second decay constant.** Using the fit parameters in Figure 3.27, we plot how the minimization of the sum of the square of the residuals (SSR) to the data depends on the value of a second decay constant, τ_2. For values larger than approximately 3×10^5 seconds, the SSR reaches a minimization limit beyond which there is no further improvement to the fit . Each color represents the data from the same experimental repeats as depicted in Figure 3.27.

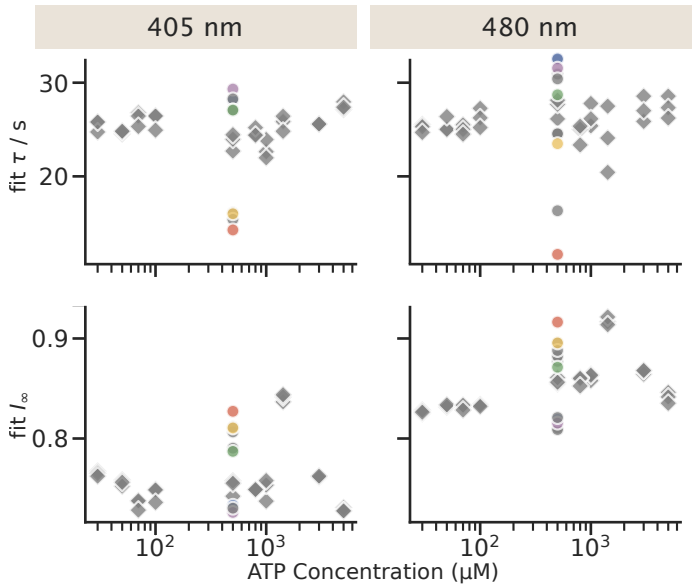

Figure 3.30: **ATP dependence of the fit parameters for photobleaching.** The fit constants, τ and I_∞, of the function, $I(t)/I_0 = (1 - I_\infty)e^{-t/\tau} + I_\infty$, are plotted as a function of ATP concentration. None of the fit parameters seem to have a clear trend as a function of ATP concentration. Circular points and diamond-shaped points display data from experiments conducted on separate dates. All data points are taken with the same imaging parameters. Each color represents the data from the same experimental repeats as depicted in Figure 3.27.

tween light excitations. In contrast, there is only small variation in the I_∞ parameter with respect to the pulsing interval.

Amid the variation in these parameters discussed above, key quantitative regularities emerge. Across experiments, all the photobleaching decay time constants are shorter than $\tau \lesssim 35$ s. In addition, all plateau intensity values I_∞ vary by less than 20%. Together, these two facts have the consequence that the late time behaviors of photobleaching trajectories agree within a few tens of percent of each other. This result can be understood by referring to equation 3.48, $I(t)/I_0 = (1 - I_\infty)e^{-t/\tau} + I_\infty$. After waiting a few decay constants—reached early in the experiment even for the slowest photobleaching trajectory—the first term $(1 - I_\infty)e^{-t/\tau}$ vanishes. Since the remaining plateau constant, I_∞, varies only mildly (by less than 20%), the overall trajectories ultimately agree within a few tens of percent of each other after long enough times.

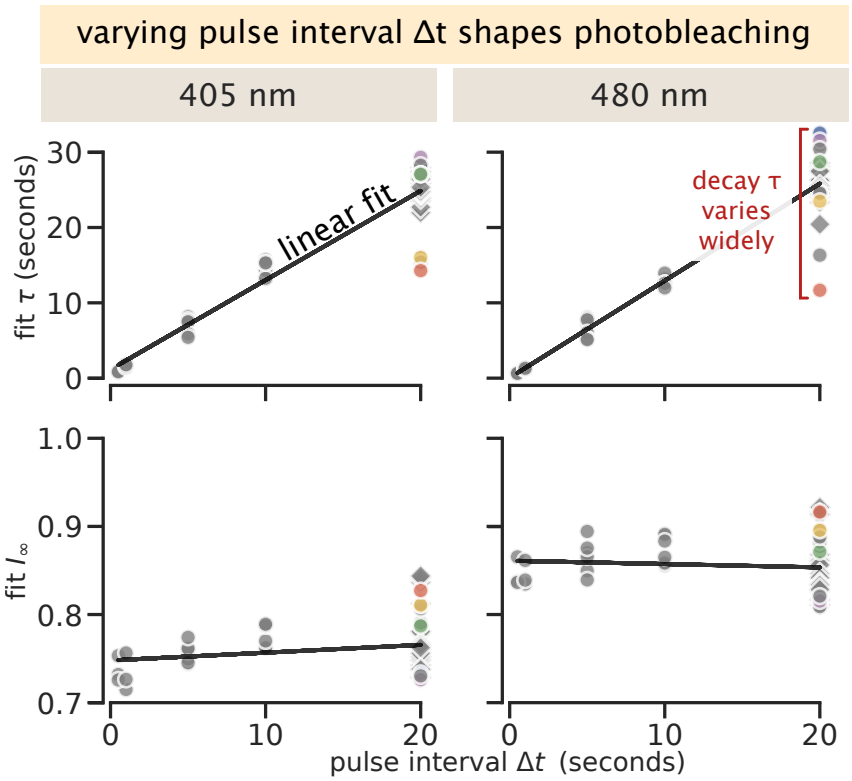

Figure 3.31: **Intrinsic and systematic variability of photobleaching kinetic parameters across days and excitation pulse intervals Δt.** On average, the fit decay time τ and offset I_∞ vary linearly with the interval Δt between excitation pulses in the measurement, as reported by acceptable linear fits between these parameters to the pulse interval Δt (shown as black lines). Five distinctly colored examples, the same experimental repeats as described by Figure 3.27, are taken at the pulse interval of $\Delta t = 20$ s, the interval typically used between frames in aster experiments, are highlighted, evidencing wide and ultimately meaningful variability in photobleaching kinetics across experiments. Circular points and diamond-shaped points display data from experiments conducted on separate dates.

Photobleaching correction procedure

With the form of the time-dependent intensity reduction in hand, we can now account for the amount of depletion due to photobleaching over time to recover the "true" intensity. In particular, we interpret the measured intensity as the product of a weighting function and the true intensity if fluorophores were not bleached. Namely, when $\tilde{I}$ is the true intensity and I is the measured intensity,

$$\tilde{I}(t) = \frac{I(t)}{f_p(t)} = \frac{I(t)}{(1 - I_\infty)e^{-t/\tau} + I_\infty}. \tag{3.53}$$

Since our probe calibrations are ratios of image intensities collected at two wavelengths, we can independently correct images from each wavelength and then take

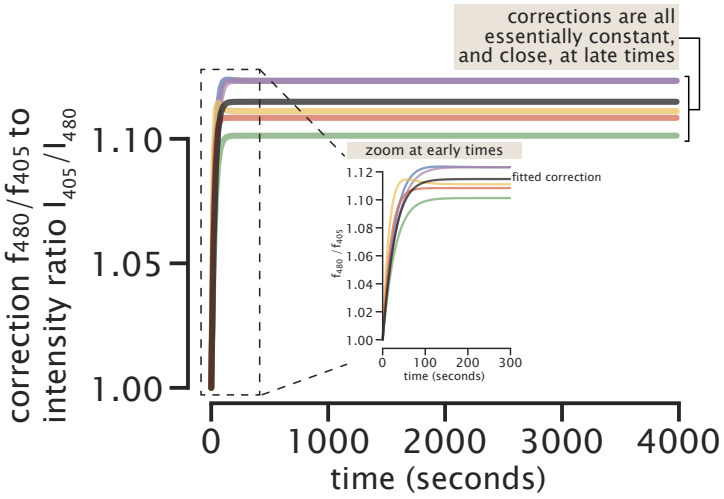

Figure 3.32: **Variation in the ratiometric photobleaching correction implied by variability in photobleaching experimental fits.** Specifically, each fluorescence channel offers a photobleaching fit function $f(t) = I(t)/I_{\max} = (1-I_\infty)\exp[-t/\tau]+I_\infty$. The measured fluorescence intensity ratio $r(t) = I_{405}(t)/I_{480}(t)$ would be corrected by the ratiometric correction $f_{480}(t)/f_{405}(t)$—and then is ultimately transformed to ATP concentration by a separate nonlinear concentration calibration function. Experimental variability in the raw kinetic parameters τ and I_∞ of each fluorescence channel thus propagate in rich ways to the shape of the ratiometric correction function. Notice even the appearance of non-monotonicity in time in the yellow and blue experimental fits' correction curves, which is facilitated by mismatches in the timescales of bleaching in the 405 nm and 480 nm channels. Each line is colored with the same scheme as the repeats described by Figure 3.27 and an additional line, the dark gray, plots the correction function when τ and I_∞ are set by the value of the linear fit at 20 seconds in Figure 3.31.

the ratio. This means the effective correction to the overall ratio is $\frac{f_{480}(t)}{f_{405}(t)}$, yielding,

$$\frac{\tilde{I}_{405}(t)}{\tilde{I}_{480}(t)} = \frac{I_{405}(t)\,f_{480}(t)}{I_{480}(t)\,f_{405}(t)}. \tag{3.54}$$

In Figure 3.32 we plot the correction values over time for five characteristic experimental replicates. In addition, we plot the consensus of the fitted parameters, τ and I_∞, as determined by the linear fit evaluated at the acquisition interval, 20 seconds, in Figure 3.31. The kinetic variability in fit parameters across experiments propagates to implied corrections. The differences are most apparent at early times before the fit functions plateau. We can see how these corrections modify the number of ATP versus time for a sample aster experiment in Figure 3.33.

As expected, the corrected ATP readouts are greater than the uncorrected mea-

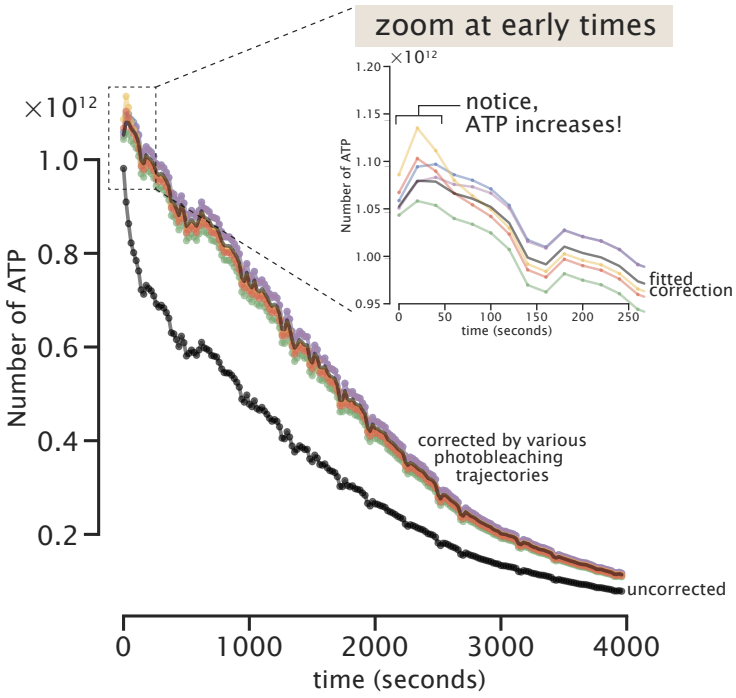

Figure 3.33: **Implications of variability across experimental photobleaching trajectories for inferred ATP abundance over time.** The black trajectory shows the number of ATP molecules over time of a representative aster if photobleaching were left uncorrected. The colored curves above are the same underlying aster data subjected to exemplary but diverse ratiometric photobleaching corrections (ensuing from those in Figure 3.32 and colored correspondingly). The dark gray curve, is the result of correcting using the τ and I_∞ values of the linear fit at 20 seconds in Figure 3.31. Notice that all corrected trajectories show an apparent *increase* in ATP over at least the first pair of data points, with, e.g., the blue and purple trajectories sustaining this apparent increase in ATP over at least two time points. Given that motors are continually consuming ATP, we expect the appearance of such an increase in ATP is pathological/nonphysical, emphasizing how profoundly photobleaching trajectories confound the resolution of ATP dynamics at early time points.

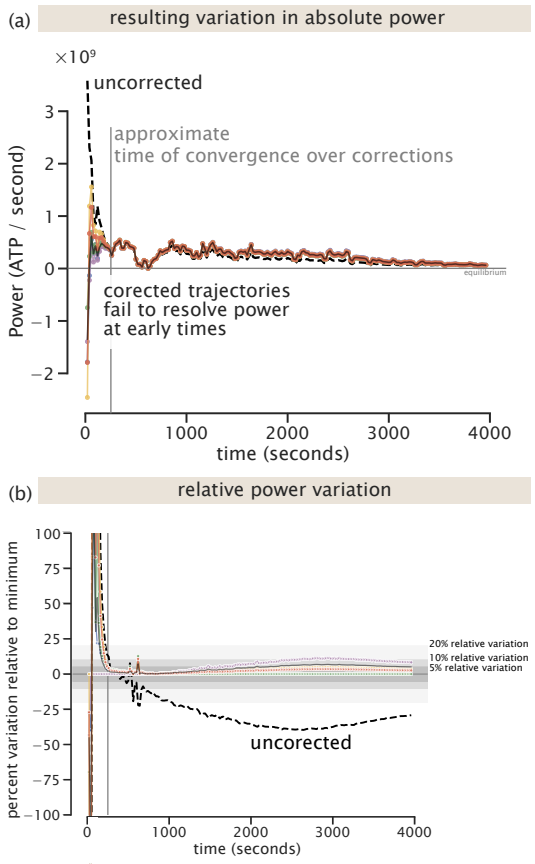

Figure 3.34: **Implications of variability across experimental photobleaching trajectories for inferred power consumption (ATP/second) over time.** (a) The black trajectory shows the consumption rate of ATP molecules over time of a representative aster if photobleaching were left uncorrected. The colored curves are the same underlying aster data subjected to exemplary but diverse ratiometric photobleaching corrections (ensuing from those in Figure 3.32 and colored correspondingly). The dark gray curve, is the result of correcting using the τ and I_∞ values of the linear fit at 20 seconds in Figure 3.31. Notice the dramatic ambiguity in even the *sign* of the ATP consumption rate, atop the quantitative disagreement across corrections, at early times. However, after a few characteristic photobleaching time constants (approximately $t \gtrsim 250\ s$, indicated by the gray line), the diversely-corrected curves closely agree. (b) In determining a cutoff time for where the varied photobleach corrected ATP curves agree, we plot the percent variation at each time for each power curve as compared to the curve with the minimum power. The variation is computed as $\frac{\text{power}_i(t)-\min(t)}{\min(t)} \times 100$, where i indexes over each corrected curve and $\min(t)$ refers to the minimum value of power at a given time t. The variation curves are laid upon three shaded regions depicting 5, 10, and 20 percent variation.

surement, yet still deplete over time as the aster consumes ATP. However, control photobleaching trajectories vary considerably across replicates and conditions at early time points. In Figure 3.33, these discrepancies manifest in corrected ATP trajectories until roughly 250 seconds ($\sim$ 4 min). Further, some candidate corrections could even spuriously show a mild increase in ATP over the earliest time points. (We regard such an apparent increase as nonphysical, given the continual consumption of ATP by motors.) This potential problem is even more apparent when examining power (namely the derivative of ATP over time), as shown in Figure 3.34. Crucially, however, after roughly 250 seconds (nearly ten times longer than the fit decay constant τ values), power trajectories across all candidate corrections align nearly identically. This concordance of the inferred ATP and power trajectories only after 250 seconds recommends that these trajectories are reliably resolvable after this short initial period.

In Figure 3.35, we see that the initial period is early in the meaningful development of the aster structures. Figure 3.35(C) depicts the the state of motor and ATP gradients at the proposed cutoff time. The motor image does not yet show any structure formation, reinforcing our recommendation to start analyzing data after the initial $t \gtrsim 250$ s period. Taking a closer look at amount of gradients developed in ATP, the grey lines in Figure 3.35(A) and (B) show the ATP profiles at all measured time points before the cutoff. After correcting for photobleaching, we find that although ATP does begin depleting, ATP throughout the system is still abundant. Additionally nearly all the gradient formation in ATP occurs after the cutoff. Given that nearly all development of spatial gradients, in both ATP and motors, occur after the cutoff and ATP is still at meaningful abundances, we proceed with our analysis examining data following this practical cutoff.

Theory of the Experiment: Analysis of Photobleach-Diffusion Equations

To develop intuition for the way in which photobleaching alters our fluorescence signal and hence could contaminate our measurement, we worked to develop a "theory of the experiment" to compute how the dynamics of the effect we are trying to measure (i.e. ATP consumption) couple with the unwanted effects of photobleaching. This effort is one of many such examples within our laboratory where we have repeatedly found it very useful to do our best job of writing down a quantitative theoretical description of the experiment and using that description to calibrate our experiments themselves [19, 20]. This is not a substitute for the actual experimental correction described in the previous section 3.8, but rather a

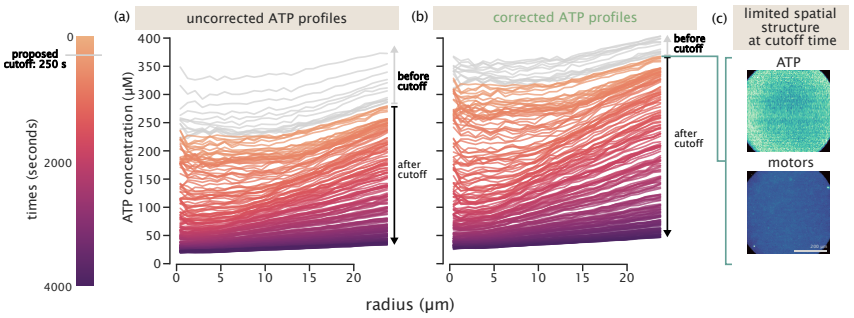

Figure 3.35: **ATP traces over space and time, with and without an exemplary photobleaching correction, relative to a proposed cutoff time—before which we propose deeming ATP dynamics quantiatively-unresolvable.**(a) Spatiotemporal profiles of ATP if no photobleaching correction were applied. (b) Spatiotemporal profiles of ATP under an exemplary photobleaching correction (corresponding to the green example photobleaching trajectory fit in the preceding figures in this section. In panels (a) and (b), profiles before the proposed cutoff time of 250 s—the same cutoff indicated by in Figure 3.34 by the vertical gray line—are colored in grey (leaving the remaining profiles, which we propose retaining, colored by time). (c) For these representative aster data, the spatial profiles of both ATP and motors have developed only modest spatial gradients at the proposed cutoff time (250 seconds, 13 frames). This means the retained data contain the bulk of interesting spatiotemporal gradient formation attending the aster formation.

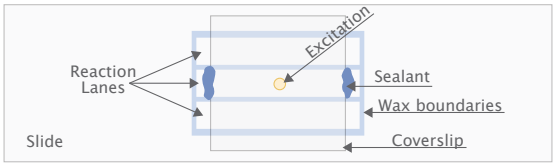

Figure 3.36: **Anatomy of the experimental chamber.** To create our experimental chamber, we cut 3 mm × 18mm lanes out of parafilm wax. We sandwich the wax sheet between a coverslip and a slide leaving the ends of the lanes exposed. This allows us to flow a reaction mixture into each lane. We seal the reaction in the lanes using picodent twinsill speed, a polymeric seal.

complementary approach for developing intuition for the scale and dynamics of the photobleaching effect.

In this section, we show how to set up quantitative models of the photobleaching and diffusion of our fluorescent probes and how the model equations can be solved as the basis of proposed photobleaching corrections in our experiments. First, in the ensuing sections 3.8 and 3.8, we write a model for the fluorescent probe independent of space, where the probe adopts two states, bleached or unbleached. This model can be used to account for the character of photobleaching in our experiments.

Figure 3.36 shows the geometry of one of our experimental devices. As shown, the experimental system is a giant reservoir encompassing a small region where illumination destroys the visibility of some molecules through photobleaching. This geometry sets up conditions for photobleaching to compete with bulk replenishment from the reservoir, as we now explore.

Photobleaching in a reservoir takes the form of a double exponential

When exciting a region of our sample, there is some rate, k_{bleach}, at which probes in this region are photobleached. These probes are then lost from the pool of probes we can account for through fluorescence. Within the excitation region, there is some concentration of fluorescent probes, c_{in}, and outside of this region, there is additional pool of fluorescent probes with concentration, c_{out}. Probes can diffuse between these regions with rates k_{in} and k_{out}. We write a model for the kinetics of probe movement. The time dependence of non-bleached probes in the illumination region is

$$\frac{dc_{\text{in}}(t)}{dt} = -k_{\text{bleach}}c_{\text{in}}(t) - k_{\text{out}}c_{\text{in}}(t) + k_{\text{in}}c_{\text{out}}(t), \tag{3.55}$$

while the time dependence of non-bleached probes outside the illumination region is,

$$\frac{dc_{\text{out}}(t)}{dt} = k_{\text{out}}c_{\text{in}}(t) - k_{\text{in}}c_{\text{out}}(t). \tag{3.56}$$

Writing the system of equations as in matrix form results in

$$\frac{d}{dt}\begin{bmatrix} c_{\text{in}} \\ c_{\text{out}} \end{bmatrix} = \begin{bmatrix} -k_{\text{bleach}} - k_{\text{out}} & k_{\text{in}} \\ k_{\text{out}} & -k_{\text{in}} \end{bmatrix}\begin{bmatrix} c_{\text{in}} \\ c_{\text{out}} \end{bmatrix}, \tag{3.57}$$

and applying the ansatz,

$$\begin{aligned} c_{\text{in}}(t) &= c_{\text{in}}^{(0)}e^{\sigma t} \\ c_{\text{out}}(t) &= c_{\text{out}}^{(0)}e^{\sigma t}, \end{aligned} \tag{3.58}$$

we can solve the system of equations as an eigenvalue problem. Plugging in the ansatz into the matrix form,

$$\sigma e^{\sigma t}\begin{bmatrix} c_{\text{in}}^{(0)} \\ c_{\text{out}}^{(0)} \end{bmatrix} = e^{\sigma t}\begin{bmatrix} -k_{\text{bleach}} - k_{\text{out}} & k_{\text{in}} \\ k_{\text{out}} & -k_{\text{in}} \end{bmatrix}\begin{bmatrix} c_{\text{in}}^{(0)} \\ c_{\text{out}}^{(0)} \end{bmatrix}, \tag{3.59}$$

which we rearrange to find

$$0 = \begin{bmatrix} -k_{\text{bleach}} - k_{\text{out}} - \sigma & k_{\text{in}} \\ k_{\text{out}} & -k_{\text{in}} - \sigma \end{bmatrix}\begin{bmatrix} c_{\text{in}}^{(0)} \\ c_{\text{out}}^{(0)} \end{bmatrix}. \tag{3.60}$$

Taking the determinant,

$$\begin{aligned} 0 &= (-k_{\text{bleach}} - k_{\text{out}} - \sigma)(-k_{\text{in}} - \sigma) - k_{\text{in}}k_{\text{out}} \\ &= \sigma^2 + (k_{\text{bleach}} + k_{\text{in}} + k_{\text{out}})\sigma + k_{\text{in}}(k_{\text{bleach}} + k_{\text{out}}) - k_{\text{in}}k_{\text{out}} \\ &= \sigma^2 + (k_{\text{bleach}} + k_{\text{in}} + k_{\text{out}})\sigma + k_{\text{in}}k_{\text{bleach}}. \end{aligned} \tag{3.61}$$

Solving for the roots of σ,

$$\sigma = -\frac{1}{2}(k_{\text{bleach}} + k_{\text{in}} + k_{\text{out}}) \pm \frac{1}{2}\sqrt{(k_{\text{bleach}} + k_{\text{in}} + k_{\text{out}})^2 - 4k_{\text{in}}k_{\text{bleach}}}. \tag{3.62}$$

Plugging this partial differential equation into Mathematica and solving for $c_{\text{in}}(t)$, we find,

$$c_{\text{in}}(t) = \frac{c_0 \exp\left(-\frac{(\alpha+\gamma)t}{2}\right)}{2\gamma}\left(\beta - \beta\exp(\gamma t) + \gamma + \gamma\exp(\gamma t)\right), \tag{3.63}$$

where, for ease of reading, we define the constants

$$\begin{aligned} \alpha &\equiv k_{\text{bleach}} + k_{\text{in}} + k_{\text{out}}, \\ \beta &\equiv k_{\text{bleach}} - 3k_{\text{in}} + k_{\text{out}}, \\ \gamma &\equiv \sqrt{-4k_{\text{bleach}}k_{\text{in}} + (k_{\text{bleach}} + k_{\text{in}} + k_{\text{out}})^2} = \sqrt{-4k_{\text{bleach}}k_{\text{in}} + \alpha^2}. \end{aligned} \tag{3.64}$$

We simplify the form of $c_{\text{in}}(t)$ by distributing the exponential prefactor,

$$c_{\text{in}}(t) = \frac{c_0}{2\gamma}\left(\beta e^{-(\alpha+\gamma)t/2} - \beta e^{-(\alpha-\gamma)t/2} + \gamma e^{-(\alpha+\gamma)t/2} + \gamma e^{-(\alpha-\gamma)t/2}\right). \tag{3.65}$$

Combining the terms in the parenthesis by exponentials,

$$c_{\text{in}}(t) = \frac{c_0}{2\gamma}\left((\gamma+\beta)e^{-(\alpha+\gamma)t/2} + (\gamma-\beta)e^{-(\alpha-\gamma)t/2}\right). \tag{3.66}$$

This equation establishes that the visible abundance of probes in the monitored region, $c_{\text{in}}(t)$, can be described as a double exponential with two characteristic timescales τ_1 and τ_2, given by,

$$\begin{aligned} \tau_1^{-1} &= (\alpha+\gamma)/2 \\ &= \frac{1}{2}\left(k_{\text{bleach}} + k_{\text{in}} + k_{\text{out}} + \sqrt{-4k_{\text{bleach}}k_{\text{in}} + (k_{\text{bleach}} + k_{\text{in}} + k_{\text{out}})^2}\right) \end{aligned} \tag{3.67}$$

and

$$\begin{aligned} \tau_2^{-1} &= (\alpha-\gamma)/2 \\ &= \frac{1}{2}\left(k_{\text{bleach}} + k_{\text{in}} + k_{\text{out}} - \sqrt{-4k_{\text{bleach}}k_{\text{in}} + (k_{\text{bleach}} + k_{\text{in}} + k_{\text{out}})^2}\right). \end{aligned} \tag{3.68}$$

We remark that since $\gamma \geq 0$, we see that $\tau_1^{-1} \geq \tau_2^{-1}$ and so $\tau_1 \leq \tau_2$. That is, the more rapid decay process is captured by the first timescale τ_1.

In Section 3.8, we find that the predictions of this model do a reasonable job of describing the photobleaching in our experiments. Specifically, our data is best fit to a double exponential with a short and a long time constant, corresponding to $\tau_2 \gg \tau_1$ and yielding an effective plateau in fluorescence on experimental timescales.

To further grapple with other origins of photobleaching, we also explored what modifications to the model are introduced by probes sticking to the glass coverslip or slide. Next, we include our findings here for those practitioners interested.

Photobleaching with surface bound probes in a reservoir takes the form of a triple exponential

As above, we write model for the bleaching dynamics inside and outside the excitation region, but now also take into account an additional effect where probes can be bound to the surface and do not diffuse. These probes can still bleach when inside the excitation region. We denote the concentration of probes inside the excitation region with variable $c_{\text{s-in}}$ and outside the excitation region as, $c_{\text{s-out}}$. We include two more rate constants, k_{on} and k_{off}, for the rates of binding and unbinding to the surface. Thus, our system of equations is now,

$$\begin{aligned}
\frac{dc_{\text{in}}(t)}{dt} &= -k_{\text{bleach}}c_{\text{in}}(t) - k_{\text{out}}c_{\text{in}}(t) + k_{\text{in}}c_{\text{out}}(t) - k_{\text{on}}c_{\text{in}}(t) + k_{\text{off}}c_{\text{s-in}}(t),\\
\frac{dc_{\text{out}}(t)}{dt} &= k_{\text{out}}c_{\text{in}}(t) - k_{\text{in}}c_{\text{out}}(t) - k_{\text{on}}c_{\text{out}}(t) + k_{\text{off}}c_{\text{s-out}}(t),\\
\frac{dc_{\text{s-in}}(t)}{dt} &= -k_{\text{bleach}}c_{\text{s-in}}(t) + k_{\text{on}}c_{\text{in}}(t) - k_{\text{off}}c_{\text{s-in}}(t),\\
\frac{dc_{\text{s}}(t)}{dt} &= k_{\text{on}}c_{\text{out}}(t) - k_{\text{off}}c_{\text{s-out}}(t).
\end{aligned} \tag{3.69}$$

Writing the system of equations as in matrix form, we have

$$\frac{d}{dt}\begin{bmatrix} c_{\text{in}} \\ c_{\text{out}} \\ c_{\text{s-in}} \\ c_{\text{s-out}} \end{bmatrix} = \begin{bmatrix} -k_{\text{bleach}} - k_{\text{out}} - k_{\text{on}} & k_{\text{in}} & k_{\text{off}} & 0 \\ k_{\text{out}} & -k_{\text{in}} - k_{\text{on}} & 0 & k_{\text{off}} \\ k_{\text{on}} & 0 & -k_{\text{bleach}} - k_{\text{off}} & 0 \\ 0 & k_{\text{on}} & 0 & -k_{\text{off}} \end{bmatrix} \begin{bmatrix} c_{\text{in}} \\ c_{\text{out}} \\ c_{\text{s-in}} \\ c_{\text{s-out}} \end{bmatrix}. \tag{3.70}$$

As a first guess, we assume the binding kinetics to the surfaces are very slow, slower than the duration of the experiment. So we simplify this system of equations

such that where surface bound probes are only subject to bleaching and do not communicate with the pool of other probes. Thus our system of equations is,

$$\begin{aligned}
\frac{dc_{\text{in}}(t)}{dt} &= -k_{\text{bleach}}c_{\text{in}}(t) - k_{\text{out}}c_{\text{in}}(t) + k_{\text{in}}c_{\text{out}}(t),\\
\frac{dc_{\text{out}}(t)}{dt} &= k_{\text{out}}c_{\text{in}}(t) - k_{\text{in}}c_{\text{out}}(t),\\
\frac{dc_{\text{s-in}}(t)}{dt} &= -k_{\text{bleach}}c_{\text{s-in}}(t),\\
\frac{dc_{\text{s-out}}(t)}{dt} &= 0.
\end{aligned} \tag{3.71}$$

Thus, the concentration of surface bound probes outside the excitation region is constant in time, and we can ignore the last equation. Now referring to the surface bound probes in the excitation region as c_{s}, we write the system of equations in matrix form,

$$\frac{d}{dt}\begin{bmatrix} c_{\text{in}} \\ c_{\text{out}} \\ c_{\text{s}} \end{bmatrix} = \begin{bmatrix} -k_{\text{bleach}} - k_{\text{out}} & k_{\text{in}} & 0 \\ k_{\text{out}} & -k_{\text{in}} & 0 \\ 0 & 0 & -k_{\text{bleach}} \end{bmatrix}\begin{bmatrix} c_{\text{in}} \\ c_{\text{out}} \\ c_{\text{s}} \end{bmatrix}. \tag{3.72}$$

As above, we prescribe the ansatz that the concentrations of each species change exponentially in time,

$$\begin{aligned}
c_{\text{in}}(t) &= c_{\text{in}}^{(0)}e^{\sigma t}\\
c_{\text{out}}(t) &= c_{\text{out}}^{(0)}e^{\sigma t}\\
c_{\text{s}}(t) &= c_{\text{s}}^{(0)}e^{\sigma t}
\end{aligned} \tag{3.73}$$

we can solve the system of equations as an eigenvalue problem. Plugging in the ansatz into the matrix form,

$$\sigma e^{\sigma t}\begin{bmatrix} c_{\text{in}}^{(0)} \\ c_{\text{out}}^{(0)} \\ c_{\text{s}}^{(0)} \end{bmatrix} = e^{\sigma t}\begin{bmatrix} -k_{\text{bleach}} - k_{\text{out}} & k_{\text{in}} & 0 \\ k_{\text{out}} & -k_{\text{in}} & 0 \\ 0 & 0 & -k_{\text{bleach}} \end{bmatrix}\begin{bmatrix} c_{\text{in}}^{(0)} \\ c_{\text{out}}^{(0)} \\ c_{\text{s}}^{(0)} \end{bmatrix}, \tag{3.74}$$

which we rearrange to find

$$0 = \begin{bmatrix} -k_{\text{bleach}} - k_{\text{out}} - \sigma & k_{\text{in}} & 0 \\ k_{\text{out}} & -k_{\text{in}} - \sigma & 0 \\ 0 & 0 & -k_{\text{bleach}} - \sigma \end{bmatrix}\begin{bmatrix} c_{\text{in}}^{(0)} \\ c_{\text{out}}^{(0)} \\ c_{\text{s}}^{(0)} \end{bmatrix}. \tag{3.75}$$

Taking the determinant,

$$\begin{aligned} 0 &= \Big((-k_{\text{bleach}} - k_{\text{out}} - \sigma)(-k_{\text{in}} - \sigma) - k_{\text{in}}k_{\text{out}}\Big)\Big(- k_{\text{bleach}} - \sigma\Big) \\ &= \Big(\sigma^2 + (k_{\text{bleach}} + k_{\text{in}} + k_{\text{out}})\sigma + k_{\text{in}}(k_{\text{bleach}} + k_{\text{out}}) - k_{\text{in}}k_{\text{out}}\Big)\Big(- k_{\text{bleach}} - \sigma\Big) \\ &= \Big(\sigma^2 + (k_{\text{bleach}} + k_{\text{in}} + k_{\text{out}})\sigma + k_{\text{in}}k_{\text{bleach}}\Big)\Big(- k_{\text{bleach}} - \sigma\Big). \end{aligned} \tag{3.76}$$

Solving for the roots of σ, the first set of big parenthesis is the same quadratic equation as before, giving the two roots,

$$\sigma = -\frac{1}{2}(k_{\text{bleach}} + k_{\text{in}} + k_{\text{out}}) \pm \frac{1}{2}\sqrt{(k_{\text{bleach}} + k_{\text{in}} + k_{\text{out}})^2 - 4k_{\text{in}}k_{\text{bleach}}}. \tag{3.77}$$

And the second big parenthesis yields a third root which is simply,

$$\sigma = -k_{\text{bleach}}. \tag{3.78}$$

Accordingly, very interestingly, bleaching with a population of probes stuck to a surface simply adds an exponential to the model, yielding a triple exponential function. To ask whether our control experiment data showed conspicuous signals of such surface sticking, we also subjected them to the triple exponential model, but concluded the fits were no better than fitting to a double exponential. Given that second time constant values already exceed the duration of the experiment, our data alone do not garner further information about a third timescale, if one should participate.

Time-dependent bleaching rates from periodic excitations

Our models in the preceding sections 3.8 and 3.8 investigated the case where the rate of photobleaching k_{b} is continuous and constant in time. In a real experiment monitoring aster formation, however, the sample is illuminated only in pulses over time, yielding frames of movies. Accordingly, the rate at which probes bleach is time dependent, so that the decay of fluorescence intensity $u(t)$ is given by the ordinary differential equation,

$$\frac{\mathrm{d}u(t)}{\mathrm{d}t} = -k_{\text{b}}(t)u(t), \tag{3.79}$$

where $k_{\text{b}}(t)$ is the rate of photobleaching. Our experiments acquire images every 20 seconds, where light only excites the sample when an image is being taken presenting a fixed exposure time of 150 ms. To understand how such time-varying bleaching

rates shape trajectories of photobleaching, we now explore properties of a simple model evoking the periodic excitations of experiments. Crucially, this understanding also delivers standard benchmark solutions that validate the numerical accuracy and stability of our most realistic, precise, and spatially-explicit simulations from finite element methods that follow next, in section 3.8.

First, to capture pulsatile excitations, we prescribe an example time-dependent photobleaching rate function as,

$$k(t) \equiv k_{\mathrm{b}} \frac{1 + \sin(2\pi t/\tau)}{2}, \tag{3.80}$$

where τ is the period of light pulses. This function is visualized in Figure 3.37(C). The rate of photobleaching is a periodic function between 0 and k_{b}. In this simple test, we do not account for diffusion of probes, only considering a degradation rate due to bleaching. The ODE for the concentration of bright probes is thus,

$$\frac{\mathrm{d}u(t)}{\mathrm{d}t} = -k(t)u(t) = -\frac{k_{\mathrm{b}}u(t)}{2}\left(1 + \sin\left(\frac{2\pi t}{\tau}\right)\right). \tag{3.81}$$

We can solve for $u(t)$ by using the separation of variables technique, resulting in the expression

$$\int_{u(0)}^{u(t)} \frac{\mathrm{d}u(t')}{u(t')} = \int_0^t -\frac{k}{2}\mathrm{d}t' + \int_0^t -\frac{k}{2}\sin\left(\frac{2\pi t'}{\tau}\right)\mathrm{d}t'. \tag{3.82}$$

Integrating both sides, we find

$$\ln\left(\frac{u(t)}{u(0)}\right) = -\frac{k}{2}t + \frac{k\tau}{4\pi}\left(\cos\left(\frac{2\pi t'}{\tau}\right) - 1\right). \tag{3.83}$$

Finally, exponentiating both sides, we arrive at the time dependent concentration given by

$$u(t) = u(0)\exp\left(-\frac{k}{2}t + \frac{k\tau}{4\pi}\left(\cos\left(\frac{2\pi t'}{\tau}\right) - 1\right)\right). \tag{3.84}$$

We plot this result as the black lines in Figure 3.37.

We can compare the numerical solution to the ODE in Equation 3.81 using the forward Euler method,

$$u(t + \Delta t) = u(t) - \frac{k_{\mathrm{b}}}{2}\Delta t\, u(t)\left(1 + \sin\left(\frac{2\pi t}{\tau}\right)\right). \tag{3.85}$$

Computing the numerical solution in python, we plot the result as the green circles in Figure 3.37(A). Both the numerical and analytic solutions are indistinguishable.

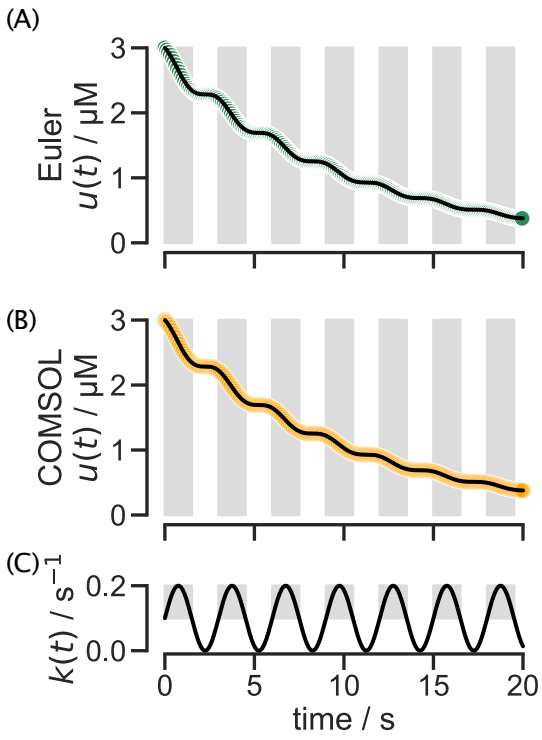

Figure 3.37: **Numerically solving the intensity decay due to photobleaching when pulsing light matches the analytic solution for both the forward Euler method and FEM.** (A) The numerical solution, via the forward Euler method, for Equation 3.81 is plotted by the green circles under the analytical solution represented with a black line. (B) The numerical solution, via the finite element method, for Equation 3.81 is plotted by the orange circles under the analytical solution represented with a black line. (C) The driving pulse of the form of Equation 3.80 is plotted with the gray shading highlighting the half periods of greater bleaching contributions.

In general, we remark that this sinusoidally-varying bleaching rate is a special case of an integrating factor behavior, namely, Eq. 3.79 has the solution,

$$u(t) = u_0 \exp\left[-\int_0^{t'} dt' k(t')\right] \tag{3.86}$$

$$\equiv u_0 \exp\left[-\langle k(t)\rangle t\right], \tag{3.87}$$

where u_0 is the value of the intensity at time zero, and in the second line we defined $\langle k(t)\rangle$ as a time averaged bleaching rate, $\langle k(t)\rangle \equiv \frac{1}{t}\int_0^t dt' k(t')$ up to time t. This behavior makes explicit that the observed intensity decay due to some time-varying photobleaching rate up to a time t can be understood as effectively an exponential decay with a time-averaged bleaching rate. Thus, the overall effect of illumination by pulses is largely to trace out a softened decay curve set by an effective duty cycle of the illumination over the experimental timescale.

Finite element simulations of our photobleaching models

Having understood how a first-order kinetic description of bleaching balanced with reservoir replenishment (sections 3.8 and 3.8) and time-varying bleaching rates (section 3.8) manifest effectively plateauing intensity trajectories, we now graduate our modeling to a full description that explicitly accounts for the depletion and transport of fluorescent probes across space. We move from the ordinary differential equations of sections 3.8 and 3.8 to a partial differential equation treatment of the full reaction diffusion equations underlying our experimental conditions.

To develop both this full theory of our experiment and develop an understanding for the continuum mechanics of our system, we harness the power of the finite element method (FEM) already introduced in section 3.7. To validate our simulations, in the next section 3.8, we perform benchmarking checks with analytic solutions to the pulsatile dynamical context discussed in section 3.8. Afterwards, in section 3.8, we thoroughly explore the effects of modulating the diffusion constant and bleach rate on the time dynamics of intensity depletion.

Validating finite element numerical conditioning with pulsing model benchmark

Before examining the full three-dimensional complexity of our problem, we first do numerical "controls" by comparing analytic and FEM solutions to the same simplified problem discussed in section 3.8. Importantly, this verifies that these simulations are numerically well conditioned and behaved for experimentally relevant conditions.

In COMSOL, we defined a cylindrical geometry in which we applied Equation 3.81. We specify a uniform concentration initial condition and impose zero flux on the boundaries. Using the time dependent solver, we specify the start time, stop time and step size with the relative tolerance set to match the step size. We plot the results of the simulation, averaged over the cylinder, in Figure 3.37(B) as the orange circles. Again we find that the numerical solution using FEM is indistinguishable from the analytical solution.

Adding a layer of complexity, we now include diffusion in our COMSOL model and ensure that our simulations accurately describe the pulsing nature of our experiment. We now add a larger cylinder to the geometry which contains the reservoir of ATP probes but is never excited by light. Probes from this larger cylinder can diffuse into the smaller cylinder where light excitation can bleach the probes. We simulate

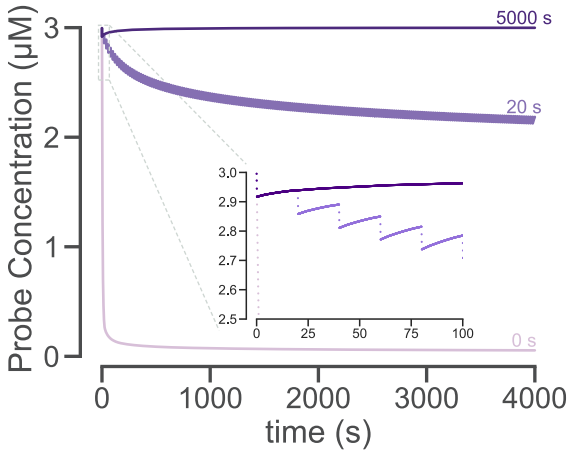

Figure 3.38: **Examining the limits of interval times, we find simulations agree with expectations.** We simulate the depletion of bright probe concentration due to photobleaching with a diffusion constant of $40\,\mu m^2/s$ and a bleaching rate of $0.02\,s^{-1}$ with three different intervals of time between pulses. In the limit of having an infinite time between pulses, or just a single pulse, we set the interval to be longer than the simulation time. The resultant curve (the darkest purple) initially undergoes decay with the other two curves, but after 20 seconds, recovers and plateaus back at the starting concentration. The middle trace plots the depletion when the light pulses every 20 seconds. The zoomed in inset of early times show a drop in concentration during each pulse and recovery for the interval between pulses. The second limit, having no time between light pulses (the lightest purple), shows monotonic depletion of bright probe concentration where a steady photobleaching smoothly depletes the bright probes regardless of their ability to diffuse.

two limits for which we already know the solutions, infinitely long and short times between pulses. When the interval between pulses is infinitely large, we would expect that as soon as the light turns off, we see recovery in the concentration of bright probes that remains constant for the rest of time. This is a FRAP experiment. The darkest line in Figure 3.38 shows just this. After one pulse which ends at 20 seconds, the concentration smoothly increases and then plateaus at about the starting concentration. In the opposite limit, when there is no interval between pulses, meaning the light is continuously on, the concentration of bright probes decays monotonically with no recovery, as seen by the lightest curve in Figure 3.38. Our experiment exists in an intermediate range, where light is pulsed every 20 seconds. The medium purple curve depicts this in Figure 3.38. We can see periodic intensity depletion and then recovery in the time between depletion. This is apparent in the zoomed-in inset.

Finite element simulations of photobleaching and transport

We now use the finite element analysis to more precisely understand the dynamics of photobleaching in our experiments, acknowledging all relevant experimental effects. In particular, our experimental setup demands a "bleach-diffusion" equation treatment since the cover slip forms a "reservoir" of fluorescent molecules that can diffuse into the bleaching region. As a result, we have two competing time scales, namely, that of the photobleaching itself and the time scale over which diffusion of molecules from the reservoir can replenish the photobleached region. In the simulations that follow, we examine the dynamics that results from tuning these two time scales independently.

We set up a COMSOL simulation with the geometric constraints of our experiment. We model the excitation region as a small cylinder, with the depth of the chamber and diameter of the light pulse, inside a larger cylinder, with a diameter of the width of the chamber, see Figure 3.39. The use of the cylindrical geometry is simply a matter of convenience for the calculations since it makes it easier to set up and visualize when the problem has this symmetry.

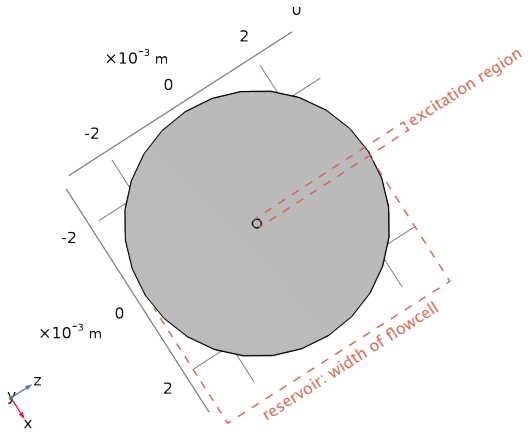

Figure 3.39: **Aerial view of cylindrical geometry in COMSOL for photobleaching simulations.** We model photobleaching experiments with two concentric cylinders. The larger has a diameter of the width of the flow cell where the sample is deposited. This larger cylinder acts as a reservoir of ATP probes. The much smaller cylinder is the region where we pulse light excitations. It is inside this region where bleachign occurs.

This simulation explores the change of concentration $u(\mathbf{r}, t)$ of bright probes through space and time when there is no aster formation. We create a reaction containing microtubules, ATP, the ATP probe, but no motor proteins to prevent ATP hydrolysis

and any structure formation. In this scenario, probes should be allowed to freely diffuse everywhere. Probes in the excitation region are subject to bleaching at a constant rate. Hence, in our simulations of this problem, we define two coefficient form partial differential equations, one to act in each region of the geometry. In the central region, there is both bleaching and diffusion, while in the exterior region, there is simply diffusion. The COMSOL form of "coefficient form partial differential equations" is

$$e_a \frac{\partial^2 u}{\partial t^2} + d_a \frac{\partial u}{\partial t} + \nabla \cdot (-c\nabla u - \alpha u + \gamma) + \beta \cdot \nabla u + au = f. \tag{3.88}$$

Inside the excitation region, probes can diffuse and undergo bleaching. Thus, we set $d_a = 1$, $c = D$, $a = -k_{\text{bleach}}$, and all other constants to zero such that

$$\frac{\partial u}{\partial t} - D\nabla^2 u + k_{\text{bleach}} = 0. \tag{3.89}$$

Outside the excitation region, probes cannot be bleached, so as a second coefficient form PDE, we set $d_a = 1$ and $c = D$, with all other constants set to zero, such that

$$\frac{\partial u}{\partial t} - D\nabla^2 u = 0. \tag{3.90}$$

We set the boundary conditions of the outer cylinder to have zero flux. At time zero, we fix the concentration across the geometry to a constant concentration, c_0.

When setting up our simulation, there are further technical specifications needed to fully describe the physical model. For those interested in precisely repeating our numerical simulations, we report the specific details of our COMSOL implementation of this problem in the following shaded box.

Specifics of Simulation Set-up:

- To capture the discrete on/off nature of pulsing the excitation light, we utilize the Events Interface in COMSOL. Events trigger the solver to reassess the step size at specified times.
  - There are two event types, explicit and implicit, available in COMSOL. Here we use two explicit events, since we know the precise timings of the light stage. Implicit events should be used when the event of interest is a response to the simulation dynamics.
  - We create a discrete states variable called ONOFF, which we initially set to a value of 1. This corresponds to the light being on.

We then create an explicit event, which turns the light off such that ONOFF = 0, which is set at time $t_{\text{excite}} = 150$ ms and repeats with an interval $t_{\text{int}} = 20$ s. A second explicit event is set to turn the light back on at $t_{\text{int}} = 20$ s, by setting ONOFF = 1, and repeats with the interval $t_{\text{int}} = 20$ s.

- We use the Coefficient Form PDE physics to describe our model. We define two separate PDEs to simulate the bright probe concentrations in each cylinder.
  - Our first PDE is defined to act upon the smaller cylinder. In this region, probes can diffuse and also be bleached by the light pulses thus, our model is
  $$\frac{\partial c}{\partial t} = D\nabla^2 c - k_{\text{bleach}} \times \text{ONOFF}. \tag{3.91}$$
  - The second PDE acts upon the larger cylinder excluding the inner smaller cylinder's volume. Here probes can only diffuse, thus we use the model
  $$\frac{\partial c}{\partial t} = D\nabla^2 c. \tag{3.92}$$
- We use a physics controlled mesh with a “Fine" element size.
- To solve the equation, we use the Time Dependent Solver with output times from 0 – 4000 s at a step size of 0.05 s. We apply a user controlled relative tolerance of 0.01. For the absolute tolerance, we use a "Scaled" global method with the "Factor" tolerance method set to a tolerance factor of 0.1. We leave the derivative tolerance method to be "Automatic."

One goal of this simulation is to understand how the parameter values for k_{bleach} and D change the time dynamics of photobleaching. We run a variety of simulations sweeping the parameter values of k_{bleach} and D as shown in Figures 3.40 and 3.41. We find that as we increase k_{bleach} and as we increase D, the steepness of the decay decreases and there is a higher concentration of bright probes at the end of the simulation. We fit the simulation curves to a single exponential plus a constant as seen in Figure 3.40. The fits are described by the equations

$$\frac{u}{u_0} = (1 - I_\infty)\exp(-t/\tau_1) + I_\infty, \tag{3.93}$$

in Figure 3.40 and a double exponential in Figure 3.41 which is described by

$$\frac{u}{u_0} = (1 - I_\infty)\exp(-t/\tau_1) + I_\infty \exp(-t/\tau_2), \tag{3.94}$$

where u_0 is the initial concentration of bright probes. We find a better agreement to the double exponential fit. Regardless of the fit type, we find the fit parameters for the fast decay constant, τ_1, and the infinite time value of the concentration, I_∞, reflect the trends in the bleaching rate and diffusion constants. The increasing steepness that results from increasing k_{bleach} and D is reflected by a decreasing τ_1. Similarly the higher ending concentration of bright probes that correlates with higher k_{bleach} and D values is reflected by an increasing I_∞ value.

Complementing our exploration of the form of the decay in probe brightness with time, we can take a more granular look into the spatial depletion profile as shown in Figures 3.42 and 3.43. Here, we draw a straight line the length of the larger cylinder diameter which passes through the center point of the geometry. Plotting the bright probe concentration as a function of position on the line, we can observe the form of depletion throughout the simulation. We find that as the diffusion constant increases, the well created by light pulsing in the inner circle becomes shallower. This makes sense because a higher diffusion constant allows bright probes to quickly replenish the darkened well. As the bleaching rate increases, the well becomes deeper. With more probes bleached per shot of light, the deficit of bright probes in the well is more significant. The simulations with zero diffusion, $D = 0$ show some noise due to numerical instability, especially at the discontinuous edges of the region of light excitation. These plots may raise concern that when treating images for photobleaching, there may need to be a spatial dependence on the corrective function. However, we find in the regions of the images we use, the spatial effects are minimal. Figure 3.43 zooms in on the light excitation region and also shows the width of the approximate final aster size. At early times, when the aster is first contracting and is about the size of the light excitation region, the concentration profile is mostly flat with little spatial dependence. At later times when there more curvature in the well, we highlight the percent change in bright probe concentration in the aster size region is maximally one percent. Thus, we do not believe applying a spatially-explicit correction to photobleaching is necessary for these experiments.

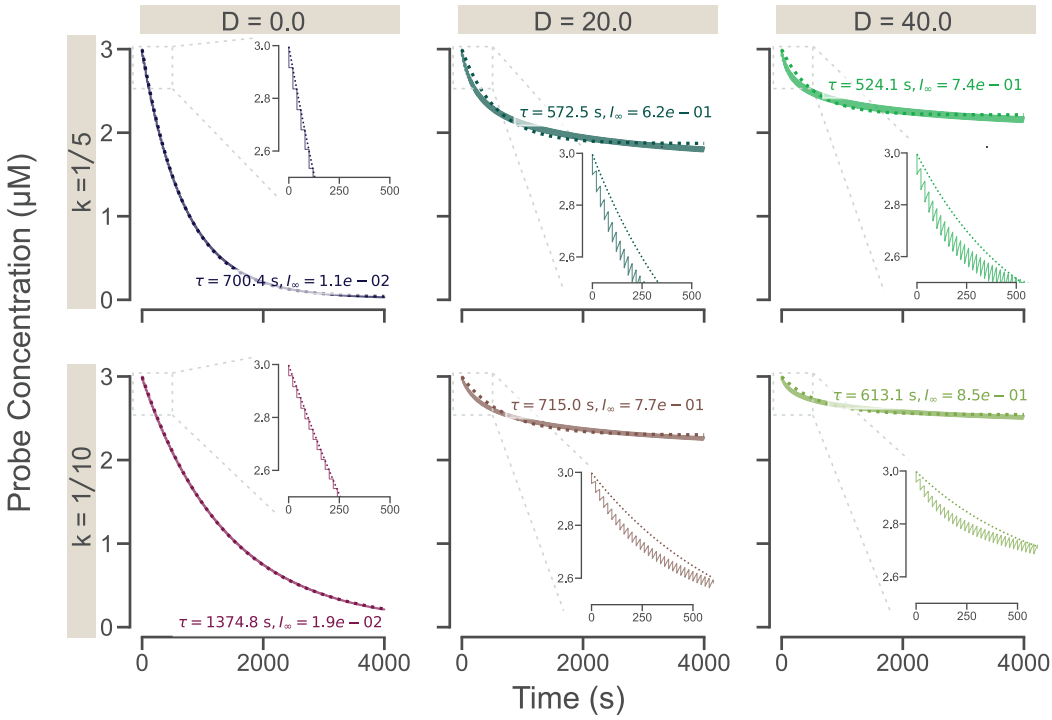

Figure 3.40: **Fitting COMSOL simulations of the bright ATP probe intensity to a single exponential plus a constant.** We simulate the depletion of bright probes due to photobleaching for a sweep of bleaching rates and diffusion constants. Fitting the time traces, which report the concentration of bright probes averaged over the light excitation region, we find a single exponential plus a constant, equation 3.93, fits the traces moderately well. We witness trends in the fit parameters such that the decay constant τ increases with increasing k_{bleach} and D, while I_∞ increases with increasing D but decreases with increasing k_{bleach}. The insets for each plot show a zoomed in blow up of the early times to visualize the initial depletion and recovery cycles corresponding to the pulses. The single exponential plus constant fits don't capture the initial decay well for non-zero diffusion.

Estimates of Photobleaching Dynamics

We conclude this section with a series of estimates aimed to give intuition into the dynamics of photobleaching in our system. Specifically, towards a sense of scale for the extent of photobleaching under these conditions, we approximate the number of fluorescent probes that might be subject to different scenarios of photophysically-challenging illumination. These estimates are based on simplifying assumptions, but we find they provide useful context by suggesting a feeling for the scales of the problem. We have included these results here and urge the reader to attempt their own version of these estimates.

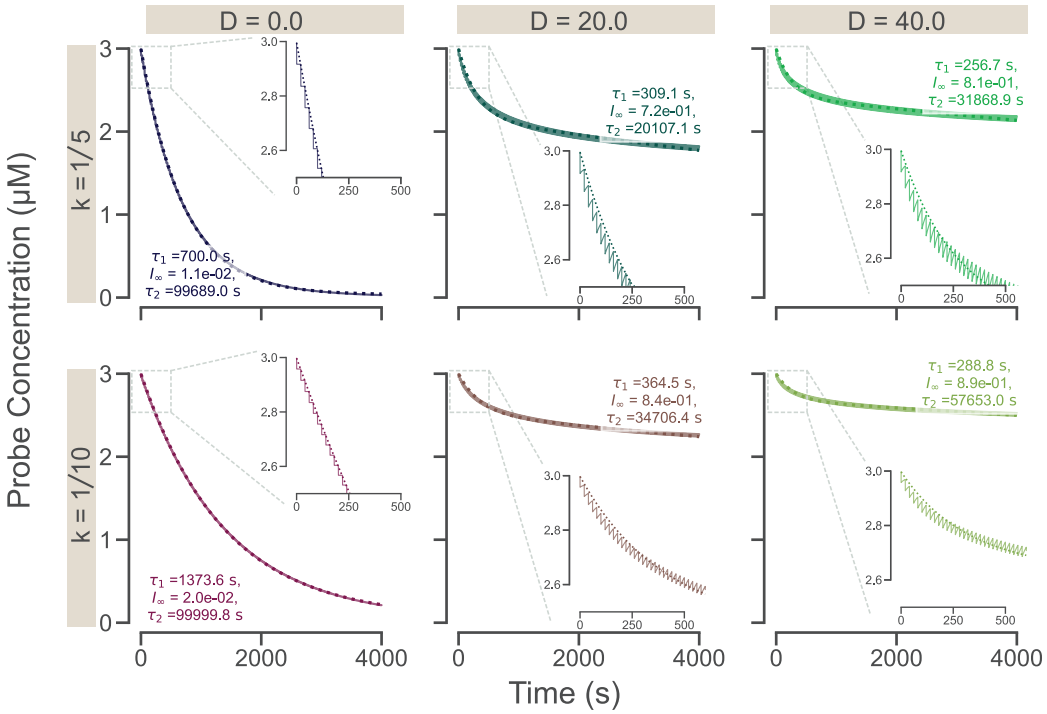

Figure 3.41: **Fitting COMSOL simulations of the ATP probe intensity decay due to photobleaching to a double exponential.** We simulate the depletion of bright probes due to photobleaching for a sweep of bleaching rates and diffusion constants. Fitting the time traces, which report the concentration of bright probes averaged over the light excitation region, we find a double exponential plus a constant, equation 3.94, fits the traces quite well, and better than the single exponential plus a constant. We witness trends in the fit parameters such that the decay constant τ_1 increases with increasing k_{bleach} and D, while I_∞ increases with increasing D but decreases with increasing k_{bleach}. The insets for each plot show a zoomed in blow up of the early times to visualize the initial depletion and recovery cycles corresponding to the pulses. The double exponential fits well capture the initial decay.

How many photons are emitted per excitation pulse?

As measured by a power meter, the power of our microscope's light excitation is $\approx 200\,\mu$W. The power meter's collection area is larger than the size of the pulse, so we take the area of illumination to be the area over which the power is distributed. The area of illumination is

$$A = 1920\,\text{px} \times 1200\,\text{px} \times \left(\frac{0.59\,\mu\text{m}}{\text{px}}\right)^2 \approx 10^6\,\mu\text{m}^2. \tag{3.95}$$

Thus, the incident power per area is

$$\frac{P}{A} = \frac{200\,\mu\text{W}}{10^6\,\mu\text{m}^2} = 2 \times 10^{-10}\,\frac{\text{W}}{\mu\text{m}^2}. \tag{3.96}$$

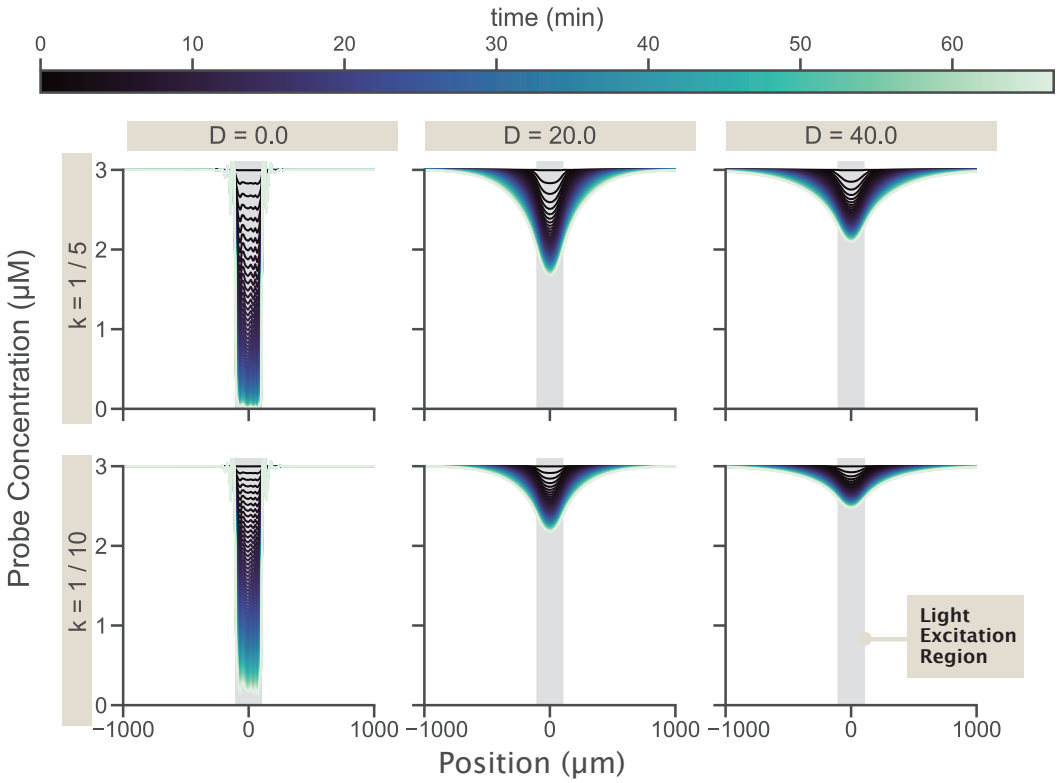

Figure 3.42: **Plotting the bright probe concentration across space shows how simulation parameters impact the depletion well formed.** We draw a cut line that spans the diameter of the larger cylinder at the midpoint of the cylinder height. Each line in the figure represents the concentration of bright probes in space for a given timepoint. We find the depth of the well depleted correlates with increasing bleaching rates and decreasing diffusion constants.

Each pulse is emitted for $\approx 150\,\text{ms}$, thus the energy per area of each pulse is,

$$\sigma_{\text{pulse}} \equiv \frac{P\Delta t}{A} = 2 \times 10^{-10}\,\frac{\text{W}}{\mu\text{m}^2} \times 0.15\,\text{s} = 3 \times 10^{-11}\,\frac{\text{J}}{\mu\text{m}^2}. \tag{3.97}$$

The wavelength of the light pulse is $\lambda \approx 400\,\text{nm}$, giving a single photon energy of

$$E_{\text{photon}} = \frac{hc}{\lambda} = \frac{(7 \times 10^{-34}\,\text{J}\cdot\text{s})(3 \times 10^{8}\,\text{m/s})}{4 \times 10^{-7}\,\text{m}} \approx 5 \times 10^{-19}\,\frac{\text{J}}{\text{photon}}. \tag{3.98}$$

Thus, the number of photons per μm^2 of a light pulse is,

$$\frac{\sigma_{\text{pulse}}}{E_{\text{photon}}} = \frac{3 \times 10^{-11}\,\text{J}/\mu\text{m}^2}{5 \times 10^{-19}\,\text{J/photon}} = 6 \times 10^{7}\,\frac{\text{photons}}{\mu\text{m}^2}. \tag{3.99}$$

For an illumination area of $A \sim 10^6\ \mu\text{m}^2$, this implies there are a total of about 6×10^{13} total emitted photons per pulse.

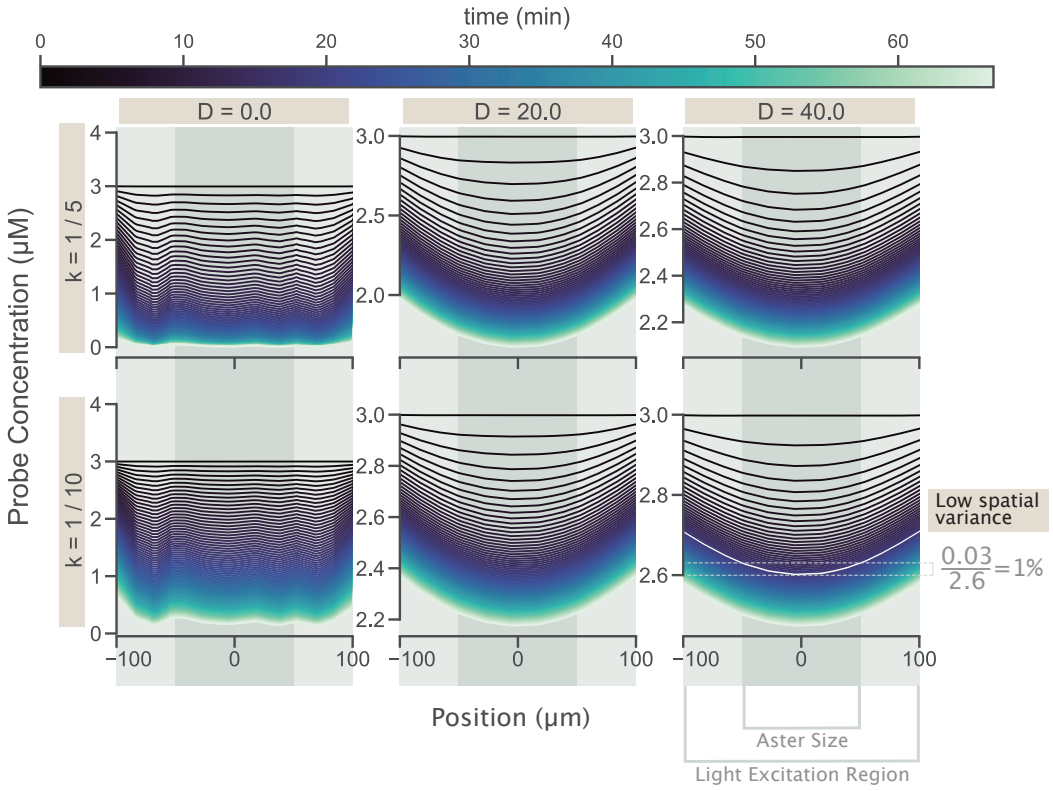

Figure 3.43: **Zooming in on the spatial depletion well created by photobleaching, there is little variation within the region of interest.** If there is high levels of variation throughout space in concentration of bright probe, we would need to correct for photobleaching with a spatial dependent function. Zooming in on the light excitation region, where our analysis occurs, we find that the extent of spatial variation is small. At early times (blacker lines), the aster is approximately the size of light excitation region, but the concentration traces are mostly flat, implying little variation. For later times (bluer lines), the traces are curvier. But during these times the aster is smaller, around the width of the dark grey region. In the bottom right plot, we show for a given time around 20 minutes (highlighted by the white trace), the variation is still small, only one percent in the aster region.

How many fluorescent probes are in the illumination area?

The concentration of ATP probes in our experiment is 2.8 μM. Given the illumination area of the excitation pulse in equation 3.95 and the depth of the experimental chamber as $d \approx 100\,\mu$m, the volume of illumination is

$$V = Ad = 10^6\,\mu\text{m}^2 \times 100\,\mu\text{m} = 10^8\,\mu\text{m}^3. \tag{3.100}$$

Thus, the number of probes illuminated is

$$\#\text{ of probes} = 2.8\,\mu\text{M}\left(\frac{10^3\mu\text{m}^3}{\mu\text{M}}\right)\left(10^8\,\mu\text{m}^3\right) \approx 3\times 10^{11}\text{ probes}. \tag{3.101}$$

How many photons are absorbed by probes according to the concentration of the sample?

The Beer-Lambert Law models the intensity reduction due to light passing through a solution. For some incident light intensity, I_0, the transmitted light intensity I, can be computed by solving

$$\log_{10}\left(\frac{I_0}{I}\right) = \epsilon l c, \tag{3.102}$$

where ϵ is the molar extinction coefficient of the solute, l is the depth of the sample chamber, and c is the concentration of solute. The extinction coefficient of QUEEN ATP reporters is listed as $\epsilon = 24,870\ \text{M}^{-1}\,\text{cm}^{-1} \approx 2\times 10^{-6}\ \mu\text{M}^{-1}\,\mu\text{m}^{-1}$ [2]. Our flow cell chambers have a depth on the order of 100 μm and the concentration of probes are about 3 μM. Inputting these values, we find the fraction of intensity that is transmitted,

$$\frac{I_0}{I} \approx 10^{(2\times 10^{-6}\,\mu\text{M}^{-1}\,\mu\text{m}^{-1})(3\,\mu\text{M})(100\,\mu\text{m})} = 10^{6\times 10^{-4}} = 1.001. \tag{3.103}$$

This means only 1 out of every 1000 incident photons are actually absorbed by fluorescent probes.

If the probes were to queue, such that one probe receives all incoming photons until it bleaches before the next probe receives any photons, how many probes die in a single pulse?

On average, common fluorescent proteins exhibit photobleaching quantum yields of order 10^{-5} (see references [21, 22]), meaning they can photobleach once they have received of order 10^5 photons. Given that a single pulse emits 6×10^{13} photons, which the adsorption fraction of the previous section implies gives 6×10^{10} adsorbed

photons, the number of probes that can be bleached in a single pulse may be very roughly estimated as,

$$\#\text{ of bleached probes} = \frac{6\times10^{13}\text{ incident photons}\frac{1\text{ adsorbed photon}}{10^3\text{ incident photons}}}{10^5\text{ photons per bleached probe}} = 6{\times}10^5\text{ bleached probes.} \tag{3.104}$$

From this, we find the fraction of bleached probes,

$$p_b = \frac{6\times10^5\text{ bleached probes}}{3\times10^{11}\text{ total probes}} = 2\times10^{-6}. \tag{3.105}$$

This is an upper bound assuming the photons are not distributed evenly. However it implies that a single pulse does little to deplete the probe intensity.

How does the intensity of the sample change as a function of the fraction of bleached probes per excitation assuming instantaneous diffusion?

In reality, the transport of fresh unbleached probes from the reservoir into the illuminated (bleached) region is neither instantaneous nor infinitely slow, but somewhere in between. Since these limiting idealized cases bound the real behavior in experiments, it is useful to get a sense of how they each behave. To wit, consider the first case where diffusive replenishment is infinitely fast. What would be the corresponding shape and quantitative rate of the resulting intensity decay?

Assuming diffusion is instantaneous, the intensity of the sample after a single pulse is the weighted average of the illuminated and not illuminated areas, A_{illum} and $A_{\text{not illum}}$, weighted by the fraction of bleached probes, p_b,

$$\langle I(n=1)\rangle = \frac{(1-p_b)I_0A_{\text{illum}} + I_0A_{\text{not illum}}}{A_{\text{illum}} + A_{\text{not illum}}} = I_0\left(1 - \frac{p_b}{1+\frac{A_{\text{not illum}}}{A_{\text{illum}}}}\right). \tag{3.106}$$

For multiple pulses, the average intensity of the sample will be

$$\langle I(n)\rangle = I_0\left(1 - \frac{p_b}{1+\frac{A_{\text{not illum}}}{A_{\text{illum}}}}\right)^n. \tag{3.107}$$

In our system, $A_{\text{illum}} = 10^6\,\mu\text{m}^2$, as defined in equation 3.95 and the not illuminated area (size of the chamber minus the illuminated area) is

$$A_{\text{not illum}} = (3\times10^3\,\mu\text{m})(18\times10^3\,\mu\text{m}) - 10^6\,\mu\text{m}^2 = 53\times10^6\,\mu\text{m}^2. \tag{3.108}$$

So, the ratio of areas is $\approx \frac{1}{50} = 0.02$. Thus any changes to the sample's average intensity occur very slowly. We can see this more clearly by noting that $1-x \approx e^{-x}$

for small x. This limit is true given that

$$\frac{p_b}{1+\frac{A_{\text{not illum}}}{A_{\text{illum}}}} \approx \frac{2\times10^{-6}}{1+0.02} \approx 2\times10^{-6}. \tag{3.109}$$

Thus, we can rewrite Equation 3.110 as,

$$\langle I(n)\rangle = I_0 \exp\left(-\frac{np_b}{1+\frac{A_{\text{not illum}}}{A_{\text{illum}}}}\right), \tag{3.110}$$

where the decay constant as a function of the number of pulses is long,

$$\frac{1+\frac{A_{\text{not illum}}}{A_{\text{illum}}}}{p_b} \approx 5\times10^5 \text{ pulses}. \tag{3.111}$$

If the short timescale of photobleaching we fit in the experiment is entirely due to surface bound probes, what area of the surface would be covered in probes?

To inform the physical possibility that probes may stick to the surface of the experimental chamber and be subject to photobleaching but not replenishment, as discussed with the model in section 3.8, we ask about the number of probes associated with a cross-sectional area of the surface. The rapid initial decay in photobleaching as measured by our control experiments drops by 20 percent. Assuming this is all due to probes stuck to the surface photobleaching, we estimate the number of probes required to create this effect. The concentration of probe in the reaction mix is 2.8 μM. The illumination region is 1920x1200 pixels with a scaling of 0.59 um per pixel. And, the height of the flow cell is 100 um. Thus, the per micron cubed number of probe molecules is,

$$N_{\text{per}\,\mu\text{m}^3} = f\,\mu\text{M}\times\frac{1000/\mu\text{m}^3}{\mu\text{M}} = f\times10^3/\mu\text{m}^3. \tag{3.112}$$

The area of illumination is

$$A = 1920\,\text{px}\times1200\,\text{px}\times\left(\frac{0.59\,\mu\text{m}}{\text{px}}\right)^2 \approx 10^6\,\mu\text{m}^2 \tag{3.113}$$

and the volume is

$$V = 10^6\,\mu\text{m}^2\times100\,\mu\text{m} = 10^8\,\mu\text{m}^3 \tag{3.114}$$

so the number of probes in the excitable region is

$$N = N_{\text{per}\,\mu\text{m}^3}\times V = f\times10^{11}. \tag{3.115}$$

For the rapid decay in the empirical photobleaching curves to be fully accounted for by surface-mediated probe bleaching, how many probes must be stuck to the surface? Since the total fluorescence decay observed is on the order of 20 percent, there would need to be

$$N_{\text{surf}} = 0.2 \times N \approx 10^{11} \tag{3.116}$$

probes stuck to the surfaces of the experimental chamber to fully account for the observed decay. We estimate the radius of each probe to be 2 nm in equation 3.204, so we approximate the area of each probe as $4 \times 10^{-5}\ \mu\text{m}^2$. Thus the total area taken up by surface bound probes is

$$A_{\text{surf probes}} = 4 \times 10^{6}\ \mu\text{m}^2, \tag{3.117}$$

implying the surface would be fully decorated in probes. We find this surface-associated density physically highly implausible.

Center Tracking

To accurately determine how concentrations change with the aster radius, it is important to accurately identify the center of an aster. Images of fluorescently labeled motor proteins in asters generally show a bright core region with fainter arms. Especially while developing, asters show diffuse, ovular boundaries. These boundaries of asters are not always geometrically contiguous or universally high in contrast with the background over the aster region. These features fundamental to real asters deeply complicate the use of automated segmentation and tracking of asters using even sophisticated image analysis pipelines and thresholding procedures. Specifically, for instance, we built and assessed a battery of semisupervised thresholding and tracking pipelines, but all methods failed to achieve satisfactory identification of asters and positions across the experimental conditions and replicates we measured. Accordingly, to ensure that this segmentation and tracking is performed robustly for every dataset, we performed manual segmentation and tracking of all asters as they formed across all data. Specifically, to accomplish this, we drew elliptical boundaries of asters over a dense number of key frames in each aster movie (using an instance of the open source Computer Vision Annotation Tool (CVAT)), and where relevant performed simple temporal interpolation of these aster boundaries between explicitly tracked key frames. This produced excellent and internally consistent tracking results. Since every ellipse furnishes both a minor and major axis for the aster, to summarize the overall radial size of the aster (e.g., as reported in the main text figures), we report the geometric mean of these two axis lengths.

3.9 Effects of Competitive Inhibition by ADP and Phosphate on ATP Hydrolysis Rates

States and Weights Modeling of ATP Hydrolysis

To quantitatively dissect the relationship between motor proteins and ATP, we develop a model describing the concentration of ATP throughout space and time. ATP can diffuse and undergo hydrolysis due to motor proteins throughout our system; however, ATP cannot regenerate. The diffusive term is straight forward and takes the form of Fick's Law, $D\nabla^2 A$. The reaction term needs to take into account the rate at which ATP can bind to a motor, along with the probability of binding. As a first pass, we model this reaction term just taking into account the statistical mechanics of ATP binding to a motor. However, this fails to acknowledge the dynamics of ATP being converted to ADP and phosphate. We elaborate on the ATP only model to include competitive inhibition resulting from ADP, as well as phosphate.

ATP Only Model – Assume No Products Present

We use a states and weights approach, as outlined in reference [23], to determine the probability of an ATP molecule binding to a motor protein for T ATP molecules in a lattice with Ω sites, one of which is the motor protein binding site. In this case, there are two states for the motor protein, as depicted in Figure 3.44. It can be unbound with energy $E = 0$ and multiplicity $\frac{\Omega!}{T!(\Omega-T)!} \approx \frac{\Omega^T}{T!}$ for $\Omega >> T$. Alternatively the motor protein can be bound, with an energy of $E = \epsilon_T$ and multiplicity $\approx \frac{\Omega^{(T-1)}}{(T-1)!}$. Putting this together, we find the probability of binding is

$$p_{\text{bound}} = \frac{\frac{\Omega^{(T-1)}}{(T-1)!}e^{-\beta\epsilon_T}}{\frac{\Omega^T}{T!} + \frac{\Omega^{(T-1)}}{(T-1)!}e^{-\beta\epsilon_T}}. \tag{3.118}$$

We simplify the probability by multiplying the numerator and denominator by $\frac{T!}{\Omega^T}$ to get

$$p_{\text{bound}} = \frac{\frac{T}{\Omega}e^{-\beta\epsilon_T}}{1 + \frac{T}{\Omega}e^{-\beta\epsilon_T}}. \tag{3.119}$$

To convert Ω, the number of "lattice sites", to a volume, we multiply the numerator and denominator by $\frac{\Delta V}{\Delta V}$, the small volume each lattice site represents. By specifying $c_0 = \frac{1}{\Delta V}$ and $[\text{ATP}] = \frac{T}{\Omega\Delta V}$, our probability now depends on concentrations and becomes

$$p_{\text{bound}} = \frac{\frac{[\text{ATP}]}{c_0} e^{-\beta\epsilon_T}}{1 + \frac{[\text{ATP}]}{c_0} e^{-\beta\epsilon_T}}. \tag{3.120}$$

Lastly, we define a constant $K_\text{T} = c_0 e^{\beta\epsilon_\text{T}}$ which gives the result

$$p_{\text{bound}} = \frac{\frac{[\text{ATP}]}{K_\text{T}}}{1 + \frac{[\text{ATP}]}{K_\text{T}}}, \tag{3.121}$$

in the form of a Michaelis-Menten (Langmuir) binding curve. Thus the constant K_T is interpreted as the concentration at which the chance of an ATP binding to a motor is fifty percent.

State	Energy	Multiplicity	Weight
	0	$\frac{\Omega^\text{T}}{T!}$	$\frac{\Omega^\text{T}}{T!}$
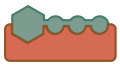	ϵ_T	$\frac{\Omega^{(\text{T}-1)}}{(T-1)!}$	$\frac{\Omega^{(\text{T}-1)}}{(T-1)!}\exp\left(-\beta\epsilon_\text{T}\right)$

Figure 3.44: **States and weights of ATP binding to motors.** Energy, multiplicity and weights for the binding states of a single motor in a lattice with Ω sites and T ATP molecules.

ADP Competitive Inhibition – Assume a Single Product

We now add in the effect of accumulating ADP into our model. If ADP binds to the motor, ATP cannot bind which creates competitive inhibition. Similar to our treatment of the ATP only system, we write down probability in terms of the weights of each state. This system has three states: the motor protein is unbound, ATP is bound, or ADP is bound, as shown in Figure 3.45. Once again, we denote the lattice sites as Ω, the number of ATP molecules as T, and the number of ADP molecules as D. We write the probability of the ATP bound state as

$$p_{\text{bound}} = \frac{\frac{\Omega^{T-1}\Omega^D}{(T-1)!D!}\exp\left(-\beta\epsilon_\text{T}\right)}{\frac{\Omega^T\Omega^D}{T!D!} + \frac{\Omega^{T-1}\Omega^D}{(T-1)!D!}\exp\left(-\beta\epsilon_\text{T}\right) + \frac{\Omega^T\Omega^{(D-1)}}{T!(D-1)!}\exp\left(-\beta\epsilon_\text{D}\right)}. \tag{3.122}$$

Multiplying the numerator and denominator by $\frac{T!D!}{\Omega^T\Omega^D}$ simplifies the expression to

$$p_{\text{bound}} = \frac{\frac{T}{\Omega}\exp\left(-\beta\epsilon_\text{T}\right)}{1 + \frac{T}{\Omega}\exp\left(-\beta\epsilon_\text{T}\right) + \frac{D}{\Omega}\exp\left(-\beta\epsilon_\text{D}\right)}. \tag{3.123}$$

We can convert this into a concentration friendly equation through the substitutions $[\text{ATP}] = \frac{T}{\Omega\Delta V}$, $[\text{ADP}] = \frac{D}{\Omega\Delta V}$, and $K_{T,D} = \frac{1}{\Delta V} e^{\beta\epsilon_{T,D}}$, which results in

$$p_{\text{bound}} = \frac{\frac{[\text{ATP}]}{K_T}}{1 + \frac{[\text{ATP}]}{K_T} + \frac{[\text{ADP}]}{K_D}}. \tag{3.124}$$

Equation 3.124 is of a similar form to equation 3.121, but has an extra term in the denominator corresponding to the likelihood of binding ADP. Thus as more ATP turns to ADP, the probability of ATP binding to the motor decreases.

Note that if we consider a model of ATP and phosphate with no ADP present, the form should be the same as in Equation 3.124 where [ADP] is replaced with $[\text{P}_i]$ and K_D is replaced with K_P.

State	Energy	Multiplicity	Weight
	0	$\frac{\Omega^\text{T}}{T!}\frac{\Omega^\text{D}}{D!}$	$\frac{\Omega^\text{T}}{T!}\frac{\Omega^\text{D}}{D!}$
	ϵ_T	$\frac{\Omega^{(\text{T-1})}}{(T-1)!}\frac{\Omega^\text{D}}{D!}$	$\frac{\Omega^{(\text{T-1})}}{(T-1)!}\frac{\Omega^\text{D}}{D!}\exp\left(-\beta\epsilon_\text{T}\right)$
	ϵ_D	$\frac{\Omega^\text{T}}{T!}\frac{\Omega^{(\text{D-1})}}{(D-1)!}$	$\frac{\Omega^\text{T}}{T!}\frac{\Omega^{(\text{D-1})}}{(D-1)!}\exp\left(-\beta\epsilon_\text{D}\right)$

Figure 3.45: **States and weights for competitive inhibition of ADP on a motor.** Energy, multiplicity and weights for three binding states: unbound motor, bound ATP, and bound ADP. Assume a lattice with Ω sites, one of which is the motor protein, T ATP molecules and D ADP molecules.

ADP and Phosphate Competitive Inhibition – Assume Both Products are Present

We can go a step further with this model by considering both hydrolysis products, ADP and phosphate, to be present in solution. This creates two new inhibition states: phosphate is bound, or phosphate and ADP are bound. We follow a similar procedure as in the ADP only model, though now we must take into account three species, ATP (T), ADP (D), and phosphate (P). As depicted in Figure 3.46, let us define the energies of the bound phosphate, and the ADP and phosphate bound states, as ϵ_P and $\epsilon_{\text{D·P}} = \epsilon_\text{D} + \epsilon_\text{P} + \sigma'$, respectively. Here we guess the energy of both

species binding is the sum of the individual binding energies, plus or minus some interaction energy, σ'. For, again, Ω binding sites, the probability of an ATP being bound to the motor is:

$$p_{\text{bound}} = \underbrace{\frac{\Omega^{T-1}\Omega^{D}\Omega^{P}}{(T-1)!D!P!}\exp\big(-\beta\epsilon_{\text{T}}\big)}_{\text{ATP Bound}} \cdot \Bigg[\underbrace{\frac{\Omega^{T}\Omega^{D}\Omega^{P}}{T!D!P!}}_{\text{Unbound}} + \underbrace{\frac{\Omega^{T-1}\Omega^{D}\Omega^{P}}{(T-1)!D!P!}\exp\big(-\beta\epsilon_{\text{T}}\big)}_{\text{ATP Bound}} + \underbrace{\frac{\Omega^{T}\Omega^{(D-1)}\Omega^{P}}{T!(D-1)!P!}\exp\big(-\beta\epsilon_{\text{D}}\big)}_{\text{ADP Bound}} + \underbrace{\frac{\Omega^{T}\Omega^{D}\Omega^{(P-1)}}{T!D!(P-1)!}\exp\big(-\beta\epsilon_{\text{P}}\big)}_{\text{P Bound}} + \underbrace{\frac{\Omega^{T}\Omega^{(D-1)}\Omega^{(P-1)}}{T!(D-1)!(P-1)!}\exp\big(-\beta(\epsilon_{\text{D}}+\epsilon_{\text{P}}+\sigma')\big)}_{\text{ADP and P Bound}} \Bigg]^{-1}. \tag{3.125}$$

We can simplify this expression by multiplying the numerator and denominator by $\frac{T!D!P!}{\Omega^{T}\Omega^{D}\Omega^{P}}$, which gives us

$$p_{\text{bound}} = \frac{\frac{T}{\Omega}\exp\left(-\beta\epsilon_{\text{T}}\right)}{1+\frac{T}{\Omega}\exp\left(-\beta\epsilon_{\text{T}}\right)+\frac{D}{\Omega}\exp\left(-\beta\epsilon_{\text{D}}\right)+\frac{P}{\Omega}\exp\left(-\beta\epsilon_{\text{P}}\right)+\frac{DP}{\Omega\Omega}\exp\left(-\beta(\epsilon_{\text{D}}+\epsilon_{\text{P}}+\sigma')\right)}. \tag{3.126}$$

Once more converting to units of concentration, we take $[\text{ATP}] = \frac{T}{\Omega\Delta V}$, $[\text{ADP}] = \frac{D}{\Omega\Delta V}$, $[\text{P}] = \frac{P}{\Omega\Delta V}$, $K_{T,D,P} = \frac{1}{\Delta V}e^{\beta\epsilon_{T,D,P}}$, and define $\sigma = e^{\beta\sigma'}$ which results in

$$p_{\text{bound}} = \frac{\frac{[\text{ATP}]}{K_T}}{1+\frac{[\text{ATP}]}{K_T}+\frac{[\text{ADP}]}{K_D}+\frac{[\text{P}]}{K_P}+\frac{[\text{ADP}][\text{P}]}{\sigma K_D K_P}}. \tag{3.127}$$

This model demonstrates how products of ATP hydrolysis compete with the motor binding sites. As more possible states emerge, the probability of ATP will binding to the motor protein reduces. We can directly see an impact on ATP hydrolysis by defining the hydrolysis rate as the probability of binding ATP multiplied by the maximum hydrolysis rate. This is written as

$$\Gamma\left([\mathrm{ATP}],[\mathrm{ADP}],[\mathrm{P}_i]\right) = \gamma \cdot \frac{\frac{[\mathrm{ATP}]}{K_\mathrm{T}}}{1 + \frac{[\mathrm{ATP}]}{K_\mathrm{T}} + \frac{[\mathrm{ADP}]}{K_\mathrm{D}} + \frac{[\mathrm{P}]}{K_\mathrm{P}} + \frac{[\mathrm{ADP}][\mathrm{P}]}{\sigma K_\mathrm{D} K_\mathrm{P}}}, \tag{3.128}$$

where γ is the ATP hydrolysis per motor per second for saturating ATP conditions with zero product concentrations.

State	Energy	Multiplicity	Weight
	0	$\frac{\Omega^\mathrm{T}}{T!}\frac{\Omega^\mathrm{D}}{D!}\frac{\Omega^\mathrm{P}}{P!}$	$\frac{\Omega^\mathrm{T}}{T!}\frac{\Omega^\mathrm{D}}{D!}\frac{\Omega^\mathrm{P}}{P!}$
	ϵ_T	$\frac{\Omega^{(\mathrm{T}-1)}}{(T-1)!}\frac{\Omega^\mathrm{D}}{D!}\frac{\Omega^\mathrm{P}}{P!}$	$\frac{\Omega^{(\mathrm{T}-1)}}{(T-1)!}\frac{\Omega^\mathrm{D}}{D!}\frac{\Omega^\mathrm{P}}{P!}\exp\left(-\beta\epsilon_\mathrm{T}\right)$
	ϵ_D	$\frac{\Omega^\mathrm{T}}{T!}\frac{\Omega^{(\mathrm{D}-1)}}{(D-1)!}\frac{\Omega^\mathrm{P}}{P!}$	$\frac{\Omega^\mathrm{T}}{T!}\frac{\Omega^{(\mathrm{D}-1)}}{(D-1)!}\frac{\Omega^\mathrm{P}}{P!}\exp\left(-\beta\epsilon_\mathrm{D}\right)$
	ϵ_P	$\frac{\Omega^\mathrm{T}}{T!}\frac{\Omega^\mathrm{D}}{D!}\frac{\Omega^{(\mathrm{P}-1)}}{(P-1)!}$	$\frac{\Omega^\mathrm{T}}{T!}\frac{\Omega^\mathrm{D}}{D!}\frac{\Omega^{(\mathrm{P}-1)}}{(P-1)!}\exp\left(-\beta\epsilon_\mathrm{P}\right)$
	$\epsilon_{\mathrm{D}\cdot\mathrm{P}}$	$\frac{\Omega^\mathrm{T}}{T!}\frac{\Omega^{(\mathrm{D}-1)}}{(D-1)!}\frac{\Omega^{(\mathrm{P}-1)}}{(P-1)!}$	$\frac{\Omega^\mathrm{T}}{T!}\frac{\Omega^{(\mathrm{D}-1)}}{(D-1)!}\frac{\Omega^{(\mathrm{P}-1)}}{(P-1)!}\exp\left(-\beta\epsilon_{\mathrm{DP}}\right)$

Figure 3.46: **States and weights for competitive inhibition of ADP and phosphate on a motor.** Energy, multiplicity and weights for five binding states: unbound motor, bound ATP, bound ADP, bound phosphate, and bound ADP and phosphate. Once more, assume a lattice with Ω sites, one of which is the motor protein, T ATP molecules, D ADP molecules, and P phosphate molecules.

Testing Our Model Against Published Data

Fitting Motor Speeds Versus ATP Concentrations

The paper *Inhibition of kinesin motility by ADP and phosphate supports a hand-over-hand mechanism* by Schief et al. [24], examines how the speed of kinesin motors vary with ADP and phosphate concentrations. This measurement is very useful to us because speed is proportionally related to ATP hydrolysis rates through the motor step size. The authors define the speed of motors as

$$S = d \cdot k_\mathrm{cat} \frac{[\mathrm{ATP}] - \frac{[\mathrm{ADP}][\mathrm{P_i}]}{K_\mathrm{eq}}}{K_\mathrm{M} + [\mathrm{ATP}]}, \tag{3.129}$$

where d is the motor step size, k_{cat} is the per second hydrolysis rate, K_M is the Menten constant, K_{eq} is the equilibrium constant for hydrolysis, and all terms in brackets are concentrations. Hydrolysis of ATP highly favors the forward direction with $K_{eq} = 4.9 \cdot 10^{11}$ µM [24], thus the second term in the numerator is negligible, as no concentrations considered exceed 10^6 µM. We now write the speed as

$$S = d \cdot k_{cat} \frac{[ATP]}{K_M + [ATP]}. \tag{3.130}$$

We scan the measured data from Schief et al. and test if our model fits to it. We first examine Figure 2 from Schief et al., which depicts motor speeds versus ATP concentrations for different levels of hydrolysis products. We fit the data to equation 3.130, where k_{cat} and K_M are the fitting parameters. We determine k_{cat} for the no product data (Figure 3.47 black curve) and then keep it fixed for all other data sets, thus all other data only has one fitting parameter, K_M.

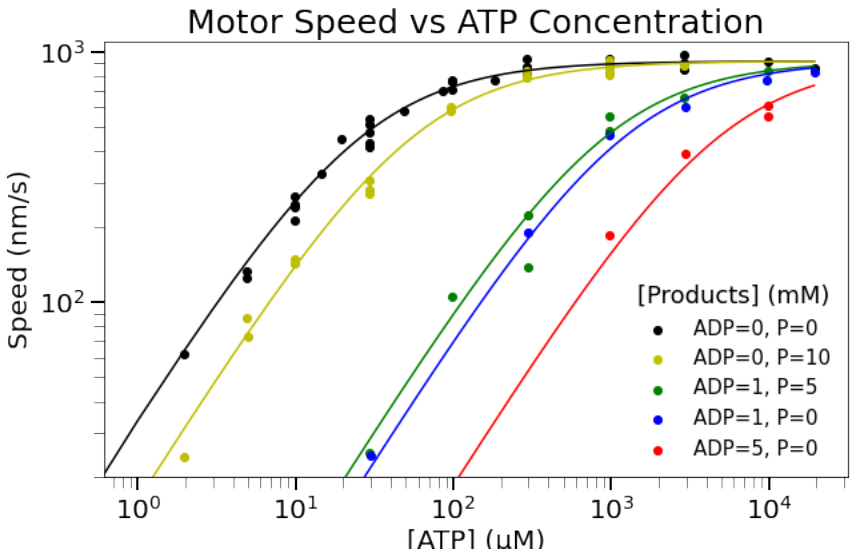

Figure 3.47: **Motor speeds for a given ATP concentration depends on the concentrations of ADP and phosphate.** Here, we replicate Figure 2 from Schief et al. The data points were determined by scanning the original figure with WebPlotDigitizer. The lines are fit to a Michaelis-Menten function. For the black curve (where the product concentrations are zero), we fit both k_{cat} and K_T parameters. For all other curves where products are present, we fit a single parameter, K_M, and use k_{cat}, from the no product condition, as an input for this function.

We can express our hydrolysis expression from equation 3.128 in the form of equation 3.130 with the following substitutions:

$$\begin{aligned}\Gamma &= \frac{S}{d},\\ k_{\text{cat}} &= \gamma,\\ K_{\text{M}} &= K_{\text{T}}\left[1+\frac{[\text{ADP}]}{K_{\text{D}}}+\frac{[\text{P}]}{K_{\text{P}}}+\frac{[\text{ADP}][\text{P}]}{\sigma K_{\text{D}}K_{\text{P}}}\right].\end{aligned} \tag{3.131}$$

With these substitutions, we can determine the binding constants for each species. We find K_{T} from the no products experiment (Figure 3.47 black curve), which is simple,

$$K_{\text{M}} = K_{\text{T}}. \tag{3.132}$$

To determine $K_{\text{D,P}}$, we use the equation

$$K_{\text{D,P}} = [\text{ADP, P}]\left(\frac{K_{\text{M}}}{K_{\text{T}}}-1\right)^{-1}, \tag{3.133}$$

(Figure 3.47 blue, red, and yellow curves). Finally to determine sigma, we write

$$\sigma = \frac{[\text{ADP}][\text{P}]}{K_{\text{D}}K_{\text{P}}}\left(\frac{K_{\text{M}}}{K_{\text{T}}}-1-\frac{[\text{ADP}]}{K_{\text{D}}}-\frac{[\text{P}]}{K_{\text{P}}}\right)^{-1}, \tag{3.134}$$

(Figure 3.47 green curve). This means the equation to find $K_{\text{D·P}}$ is

$$K_{\text{D·P}} = [\text{ADP}][\text{P}]\left(\frac{K_{\text{M}}}{K_{\text{T}}}-1-\frac{[\text{ADP}]}{K_{\text{D}}}-\frac{[\text{P}]}{K_{\text{P}}}\right)^{-1}. \tag{3.135}$$

The tabulated parameters are listed in Table 3.1

Through this analysis, we find that the values of K_{T} and K_{D} are about equivalent, perhaps this is due to similar chemical structure. It can thus be expected that the presence of ADP in our assay will cause significant slowing in the motor hydrolysis rate. On the other hand, K_{P} is two orders of magnitude larger than K_{T}, implying a small chance of phosphate binding to the motor protein. While we can expect some inhibition due to phosphate, it appears that competitive inhibition due to ADP dominates.

Strangely, $K_{\text{D·P}}$, and thus σ, is negative. It is also very large, four orders of magnitude larger than K_{T}. A negative binding constant would mean that the presence of both ADP and phosphate reduces competitive inhibition for the motor protein, while only having one of the species present creates increases the inhibition. This does not

Figure 3.47 Parameter Fits		
Parameter	Value	Description
γ	$114.5s^{-1}$	Fitted Parameter
$K_{\text{M (Black)}}$	26.2µM	Fit for 0 mM ADP, 0 mM P
$K_{\text{M (Yellow)}}$	55.8µM	Fit for 0 mM ADP, 10 mM P
$K_{\text{M (Blue)}}$	1.2mM	Fit for 1 mM ADP, 0 mM P
$K_{\text{M (Red)}}$	4.9mM	Fit for 5 mM ADP, 0 mM P
$K_{\text{M (Green)}}$	930µM	Fit for 1 mM ADP, 5 mM P
K_{T}	26.2µM	Equation 3.132
K_{D}	24.5µM	Equation 3.133
K_{P}	8.9mM	Equation 3.133
$K_{\text{D·P}}$	−714mM	Equation 3.135
σ	−3.3µM	Equation 3.134

Table 3.1: All the fitted parameters from Figure 3.47 are reported, along with the resulting Menten constants for each species.

seem physical. At best we would expect that the ADP and phosphate always bind together, so the total inhibition is equivalent to inhibition of ADP alone, as this is the more dominant inhibitor. Mathematically, this value for $K_{\text{D·P}}$ does not jibe with our model because it requires that σ is a negative value. We defined $\sigma = e^{-\beta\sigma'}$, where σ' is an interaction energy for the duel binding of ADP and phosphate. A negative σ implies an imaginary σ'.

Regardless of the sign, the magnitude of $K_{\text{D·P}}$ indicates that the inhibition due to ADP and P being bound is much smaller than the effect of either product alone and could possibly be negligible. Schief et al. only present one data set (green) with both products present in solution. These experiments seem worth replicating to understand if there is some behavior that is incorrectly incorporated into our model.

Figure 3.48 examines how the fit changes for different values of $K_{\text{D·P}}$. Setting $K_{\text{D·P}} = \infty$, thereby neglecting the interaction term, is the next best fit to the data after setting $K_{\text{D·P}} = \sigma \cdot K_{\text{D}} \cdot K_{\text{P}}$. Both taking the absolute value of σ and setting $\sigma = 1$ produce worse fits.

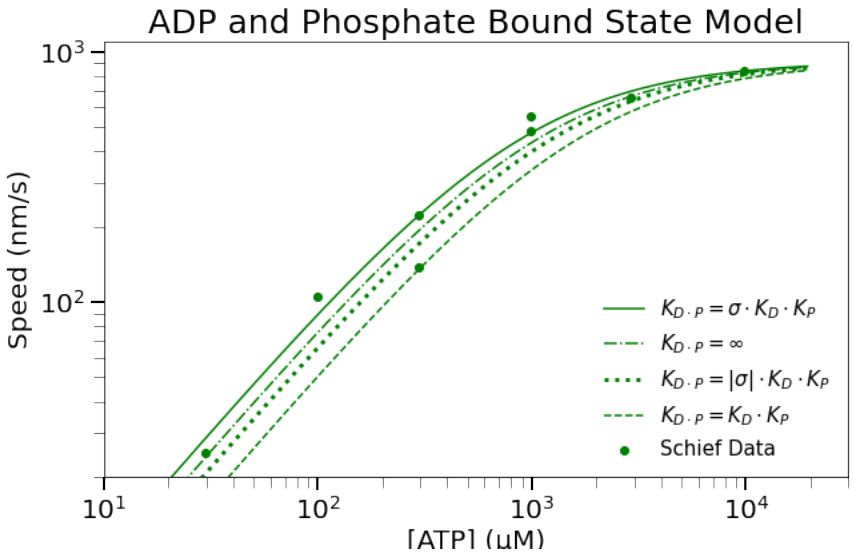

Figure 3.48: **Exploration of $K_{\mathrm{D\cdot P}}$ values for the ADP and phosphate bound state**. We examine the fits from varying the σ value in $K_{\mathrm{D\cdot P}}$. Using $\sigma = -713$ mM as found from our model, we get the best fit to the data. However, because a negative σ does not seem physical, we explore how setting σ to 713 mM, 1, and ∞ change the fits. We find that entirely neglecting the ADP/Phosphate bound state, setting $\sigma = \infty$ is the next best fit to the data. This is followed by taking $|\sigma| = 713$ mM, as the magnitude reduces the amount of inhibition experienced. Lastly, ignoring an interaction energy, setting $\sigma = 1$ produces the worst fit, as it maximizes the inhibition due to each product.

Additionally from Table 3.1, we learn about the hydrolysis rate of the motors in question. Our model quotes a rate of 114.5 ATP hydrolyzed per second per motor, for saturating ATP conditions with no products in solution. Previous work also using full length *Drosophila* conventional kinesin measures consistent hydrolysis rates with our fitted rate [25].

Fitting Motor Speeds Versus Product Concentrations

The authors took additional data investigating motor speeds versus various levels of products at various ATP levels. Using our model, we fit the data to

$$S = d \cdot \gamma \frac{\frac{[\mathrm{ATP}]}{K_T}}{1 + \frac{[\mathrm{ATP}]}{K_\mathrm{T}} + \frac{[\mathrm{ADP, P}]}{K_{\mathrm{D,\,P}}}}, \tag{3.136}$$

where we fit one parameter, $K_{\mathrm{D,\,P}}$. The first set of data, depicted in Figure 3.49, illustrates the variation in motor speed for different phosphate concentrations. Motor

speeds drop with increasing phosphate, especially as ATP concentrations drop, which implies inhibition is occurring.

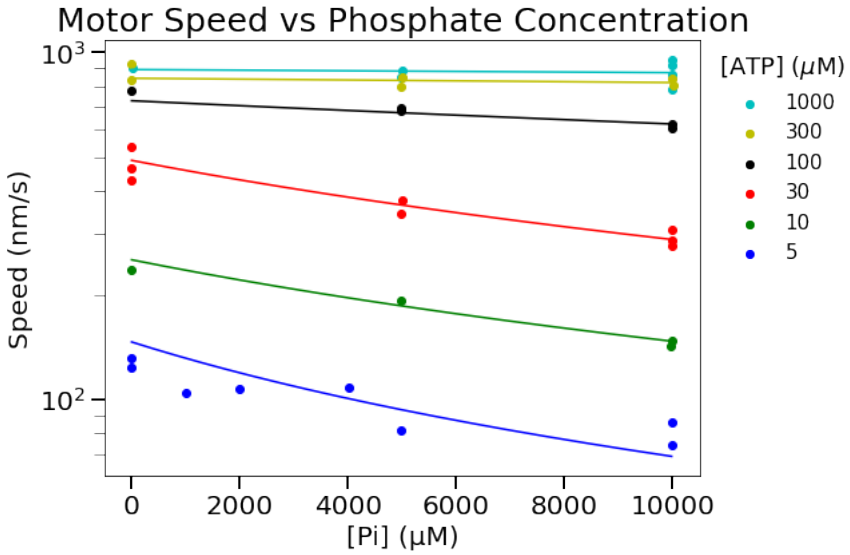

Figure 3.49: **Motor speeds are reduced with increasing phosphate concentrations.** Here, we replicate Figure 4A from Schief et al. The data points were determined by scanning the original figure with WebPlotDigitizer. The lines are fit to a Michaelis-Menten function. For each curve we fit a single parameter, K_P , and use k_{cat} and K_T, from Table 3.1, as inputs.

Our fits result in the K_P values quoted in Table 3.2. This data set produces an average K_P of 11.3 mM, comparable to the 8.9 mM value found from the previous data set in Table 3.1. There does not appear to be a trend in the K_P value with ATP concentration.

K_P Fitted Values for Various ATP Concentrations	
ATP Concentration (μM)	K_P (mM)
1000	12.2
300	27.9
100	12.5
30	6.8
10	10.1
5	7.4
Average	11.3

Table 3.2: Here we report upon the fits of K_P from the data in Figure 3.49. We do not find a correlation with ATP concentrations, as expected from our model.

The authors also examined the variation in speed with ADP concentration, as depicted in Figure 3.50. Once again, we have plotted the digitized data from Schief et al. and fit the points to our model in equation 3.136. Motor speeds drop significantly with higher levels of ADP present. Again, this is more drastic for lower ATP concentrations.

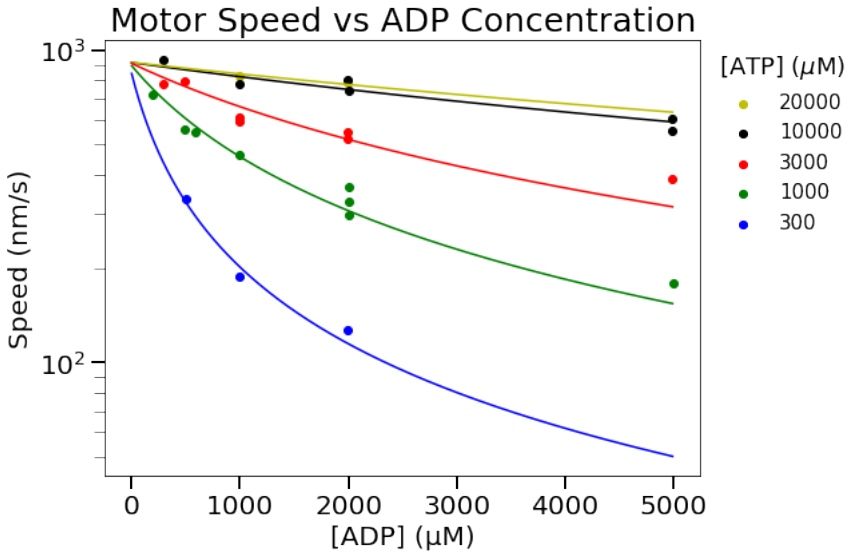

Figure 3.50: **Motor speeds are significantly reduced with increasing ADP concentrations.** Here, we replicate Figure 4B from Schief et al. The data points were determined by scanning the original figure with WebPlotDigitizer. The lines are fit to a Michaelis-Menten function. For each curve we fit a single parameter, K_D, and use k_{cat} and K_T, from Table 3.1, as inputs.

Table 3.3 reports the fitted K_D values. On average, $K_D = 23.6$ matching the $K_D = 24.5$ from table 3.1. Again, K_D values do not appear correlated with ATP concentration.

Comparison of Our Model to the Schief Model

We now compare our model with the model used in Schief et al. (2004) The authors defined k_{cat} and K_M as

$$k_{cat} = \frac{k_{cat}^{00}}{1 + \frac{[ADP]}{K_{ii}^{ADP}} + \frac{[P_i]}{K_{ii}^{P}} + \frac{[ADP][P_i]}{K_{ii}^{ADP\cdot P}}}, \tag{3.137}$$

and

$$\frac{K_M}{k_{cat}} = \frac{K_M^{00}}{k_{cat}^{00}} \left[1 + \frac{[ADP]}{K_i^{ADP}} + \frac{[P_i]}{K_i^{P}} + \frac{[ADP][P_i]}{K_i^{ADP\cdot P}}, \right] \tag{3.138}$$

K_D Fitted Values for Various ATP Concentrations	
ATP Concentration (mM)	K_D (μM)
20	14.7
10	23.8
3	23.0
1	26.7
0.3	25.4
Average	23.6

Table 3.3: Here we report upon the fits of K_D from the data in Figure 3.50. We do not find a correlation with ATP concentrations, as expected from our model.

respectively. The subscript 00 denotes the constants when the products are at zero concentration. The subscript i describes competitive inhibition by the products on the motor protein impacting the Menten term. The subscript ii is described as non-competitive inhibition which modifies the overall stepping rate and the Menten constant. Inputting equations 3.137 and 3.138 into equation 3.130, we find

$$S = d \cdot \frac{k_{\text{cat}}^{00}}{1 + \frac{[\text{ADP}]}{K_{\text{ii}}^{\text{ADP}}} + \frac{[\text{P}_\text{i}]}{K_{\text{ii}}^{\text{P}}} + \frac{[\text{ADP}][\text{P}_\text{i}]}{K_{\text{ii}}^{\text{ADP·P}}}} \cdot \frac{[\text{ATP}]}{\frac{K_{\text{M}}^{00} k_{\text{cat}}^{00}}{k_{\text{cat}}^{00}} \frac{1 + \frac{[\text{ADP}]}{K_{\text{i}}^{\text{ADP}}} + \frac{[\text{P}_\text{i}]}{K_{\text{i}}^{\text{P}}} + \frac{[\text{ADP}][\text{P}_\text{i}]}{K_{\text{i}}^{\text{ADP·P}}}}{1 + \frac{[\text{ADP}]}{K_{\text{ii}}^{\text{ADP}}} + \frac{[\text{P}_\text{i}]}{K_{\text{ii}}^{\text{P}}} + \frac{[\text{ADP}][\text{P}_\text{i}]}{K_{\text{ii}}^{\text{ADP·P}}}} + [\text{ATP}]}. \quad (3.139)$$

Simplifying the denominator and dividing the numerator and denominator by K_{M} yields

$$S = \frac{d \cdot k_{\text{cat}}^{00} \cdot \frac{[\text{ATP}]}{K_{\text{M}}^{00}}}{1 + \frac{[\text{ATP}]}{K_{\text{M}}^{00}} + \frac{[\text{ADP}]}{K_{\text{i}}^{\text{ADP}}} + \frac{[\text{P}_\text{i}]}{K_{\text{i}}^{\text{P}}} + \frac{[\text{ADP}][\text{P}_\text{i}]}{K_{\text{i}}^{\text{ADP·P}}} + \frac{[\text{ATP}]}{K_{\text{M}}^{00}} \left(\frac{[\text{ADP}]}{K_{\text{ii}}^{\text{ADP}}} + \frac{[\text{P}_\text{i}]}{K_{\text{ii}}^{\text{P}}} + \frac{[\text{ADP}][\text{P}_\text{i}]}{K_{\text{ii}}^{\text{ADP·P}}} \right)}. \quad (3.140)$$

Comparing the Schief et al. model (equation 3.140) with our model of binding (equation 3.127), we note many parallels. Dividing $d \cdot k_{\text{cat}}^{00}$, from the Schief model gives the probability of ATP binding to the motor. Note that the hydrolysis rate k_{cat}^{00} is what we denote γ. The numerators are of the same form with $K_T = K_{\text{M}}^{00}$. The Schief model contains three additional terms in the denominator, as compared to our model. These three terms imply three additional binding states, ATP and ADP bound, ATP and phosphate bound, or all three species bound.

Model Comparisons		
Parameter	Schief Model	Our Model
k_{cat}^{00}	$113.2s^{-1}$	$114.5s^{-1}$
K_M^{00}	28.1μM	26.2μM
K_i^P	9mM	8.9mM
K_i^{ADP}	34.6μM	24.5μM
$K_i^{ADP\cdot P}$	95mM	−714mM
K_{ii}^P	200mM	-
K_{ii}^{ADP}	23mM	-
$K_{ii}^{ADP\cdot P}$	30mM	-

Table 3.4: We compare the fitted parameters from our model versus the fitted parameters found by the Schief model. Overall the fits are in agreement with the exception of the Menten constant for the ADP and phosphate bound state.

We report the fitted parameters found by the Schief model, as well as the comparable values we determined in table 3.1, in table 3.4.

The values found by both models are very similar with the exception of the $K_{D\cdot P}$ value. The Schief model yields a positive value about an order of magnitude lower than our model. The low Schief value results in a larger overall K_M, which in our model pushes the fit farther away from the measured data. This makes the Schief $K_{D\cdot P}$ the worst of all the fits for both species present according to figure 3.48. However, with this exception, we have excellent agreement with all of our other parameters. Finally, the Schief model has three additional parameters, the K_{ii}. These are all very large, in the tens to hundreds of millimolar, and are multiplied by $K_T = 23$ μM, as seen in equation 3.140. This renders the cross terms effectively negligible to the model and causes the Schief model to be equivalent to our model.

3.10 Power Estimates

For decades, the question of how energy is invested in cellular processes has been of great interest. In the 1970s, several independent threads converged on these same questions with one set of efforts focused on the cost of cytoplasm [26, 27], others focused on the apparently futile cycles of GTP hydrolysis in protein translation [28] and yet others investigating the role of GTP hydrolysis in the context of microtubules [29, 30]. Our aim in this section is to build on these early efforts (and many others) to carefully characterize the power cost of a variety of processes that attend the rearrangements of the motors and microtubules that occur during aster formation in our experiments. Broadly speaking, the philosophy of the approach is

to make a list of various processes that we know take place during aster formation and to examine quantitative estimates of the power associated with these processes. Conceptually, the structure of all of the estimates will be the same, with the generic functional form

$$\text{power of process} = J_{process} \times \Delta\mu_{process}. \tag{3.141}$$

Here we have defined the quantity $\Delta\mu_{process}$ as the free energy cost of a unit process such as a single step of a motor or the movement of a single molecule up a gradient. $J_{process}$ refers to the flux associated with the process of interest, meaning how many unit processes occur per unit time. For example, in the context of constantly pumping ions up a concentration gradient, $\Delta\mu_{process}$ refers to the free energy cost of taking a single ion from one side of the membrane to the other. Similarly, the flux in that case would be given by a phenomenological linear transport law relating the concentration jump across the membrane to the flux itself. Using this quantitative structure, we carry out a series of estimates for each of the processes we think is implicated in the structural rearrangements of our motor-microtubule systems.

Experimentally Measured Power

During aster formation, we measure $\approx f \times 10^8$ ATPs are consumed per second, as shown in the main text Figure 2.3. As noted above, we aim to put this measured value into context through a series of estimates geared towards understanding the power of various processes that attend the formation of an aster. In particular, we are intrigued by the relative costs of processes such as the entropy of orientational ordering, the reduction in volume (i.e., pV work), the maintenance of gradients and so on. Each of the sections below examines one such process in detail.

Estimate of the Power of Stepping Motors

At the mechanistic level, we know what is happening to the ATP. It is being consumed by motors. Hence, the simplest statement about the ATP consumption is that every time a motor takes a step it hydrolyzes an ATP. As a proof of principle check, we ask if the power expenditure based on the measured motor hydrolysis rate matches the experimentally measured power. We measure a motor hydrolysis rate of $\gamma \approx 0.5 \frac{\text{ATP}}{\text{s·motor}}$. If all motor proteins consume ATP at this rate, we can multiply the hydrolysis rate by the number of motors in the system to find the expected power. Our experiments contain 1 μM motors, in an initial cylindrical volume of

$$V_i = \pi R^2 d = \pi \times (125\,\mu\text{m})^2 \times (70\,\mu\text{m}) \approx 3 \times 10^6\,\mu\text{m}^3, \tag{3.142}$$

which translates to

$$N_{\text{mot}} = C_i V_i = 10^{-6}\,\frac{\text{mol}}{\text{L}} \times \left(10^3\,\frac{\text{L}}{\text{m}^3}\right) \times \left(3 \times 10^{-12}\,\text{m}^3\right) \times \left(6 \times 10^{23}\,\frac{\text{MT}}{\text{mol}}\right) \approx 2{\times}10^9\ \text{motors}. \tag{3.143}$$

Thus the power expected of the system is

$$P = N_{\text{mot}}\gamma = 0.5\frac{\text{ATP}}{\text{s}\cdot\text{motor}} \times \left(2 \times 10^9\ \text{motors}\right) \approx 10^9\,\frac{\text{ATP}}{\text{s}}. \tag{3.144}$$

Compared to the $f \times 10^8\,\frac{\text{ATP}}{\text{s}}$ measured in our experiment, this estimate is within a factor of a few of the measured ATP consumption rate. In this sense, the experimental measurements are coherent with what we know about the agents that are consuming ATP. But our question is really a deeper one. We ask what is it that the motors are doing with their capacity to do work through the application of forces?

Estimate of the Power of Aster Contraction via pV Work

During the process of aster formation, the volume occupied by the microtubules that make up that aster decreases. Initially, microtubules of fixed length are uniformly distributed in a cylinder with a height, h, and radius, R. This cylinder corresponds to the region where we project light to induce motor dimerization, which drives aster formation. Some time after turning on the light, $\Delta\mathcal{T}$, the microtubules are organized in a sphere with radius, r, where $R > r$. This process is illustrated in Figure 3.51. Here, we perform a simple estimate to determine the pressure-volume work to contract an ideal gas of microtubules into a smaller aster volume. We are cognizant that a collection of microtubules is not a gas, but we suspect this the entropic cost will exceed the value we estimate here. We express the pressure of the microtubule gas as a function of volume based on the ideal gas law as

$$PV = Nk_{\text{B}}T \Rightarrow P = \frac{Nk_{\text{B}}T}{V}, \tag{3.145}$$

and input it into the equation for pressure-volume work

$$W = -\int_{V_i}^{V_f} P dV = -\int_{V_i}^{V_f} \frac{Nk_{\text{B}}T}{V} dV = -Nk_{\text{B}}T \ln\left(\frac{V_f}{V_i}\right), \tag{3.146}$$

where V_f is the aster sphere volume and V_i is the cylindrical microtubule gas volume. Note that V_f is smaller than V_i which implies that $V_f/V_i < 1$, and hence the work done is positive since the system is compressed. We now use numbers characteristic of our experiments to calculate the amount of work performed in the process of contracting the network into its final shape. First, we take the initial cylindrical

volume to be

$$V_i = \pi R^2 d = \pi \times (125\,\mu\text{m})^2 \times (70\,\mu\text{m}) \approx 3 \times 10^6\,\mu\text{m}^3, \tag{3.147}$$

and the final spherical aster volume to be

$$V_f = \frac{4}{3}\pi r^3 = \frac{4}{3}\pi \times (30\,\mu\text{m})^3 \approx 10^5\,\mu\text{m}^3. \tag{3.148}$$

Given the initial concentration of microtubules $C_i = 1$ nM, we can find the number of microtubules as

$$N_{\text{MT}} = C_i V_i = 10^{-9}\frac{\text{mol}}{\text{L}} \times \left(10^3 \frac{\text{L}}{\text{m}^3}\right) \times \left(3 \times 10^{-12}\,\text{m}^3\right) \times \left(6 \times 10^{23}\,\frac{\text{MT}}{\text{mol}}\right) \approx 2 \times 10^6\,\text{MT}. \tag{3.149}$$

We can now combine all of these results to find the pressure-volume work as

$$W = -2 \times 10^6 \times \ln\left(\frac{1}{30}\right)\, k_{\text{B}}T \approx 7 \times 10^6\, k_{\text{B}}T. \tag{3.150}$$

Under physiological conditions the energy derived from an ATP hydrolysis event is $\approx 20\, k_{\text{B}}T$ [31]. Thus, in ATP units the work is equivalent to

$$W \approx 7 \times 10^6\, k_{\text{B}}T \times \frac{\text{ATP}}{20\, k_{\text{B}}T} = 4 \times 10^5\ \text{ATP}. \tag{3.151}$$

We can also compute the power of volume contraction by dividing the work by the time it takes to form the aster. In our experiments, asters form in approximately 10 minutes, thus

$$P = \frac{W}{\Delta \mathcal{T}} = \frac{4 \times 10^5 \text{ATP}}{600\ \text{s}} \approx 10^3\,\frac{\text{ATP}}{\text{s}}. \tag{3.152}$$

From this estimate, we find that the pressure-volume contribution to the power of aster contraction is negligible since the pV work effect is five orders of magnitude smaller than measured powers. We will approach this same question differently using ideas of nematohydrodynamics in a later section.

The Entropy Cost of Bundling

Here we investigate the power to reduce the entropy of the system by dimerizing motor proteins. For this simple thought experiment suggested to us in conversations with Erwin Frey, we compare the number of microstates of a pair of independent microtubules, not bridged by motors, in comparison to linked microtubules by a dimerized motor pair. Say that two independent microtubules of length l are placed on separate one dimensional tracks with lattice sites at a spacing a, the step size of the motor. If each track is twice the length of a microtubule, $2l$, then there are

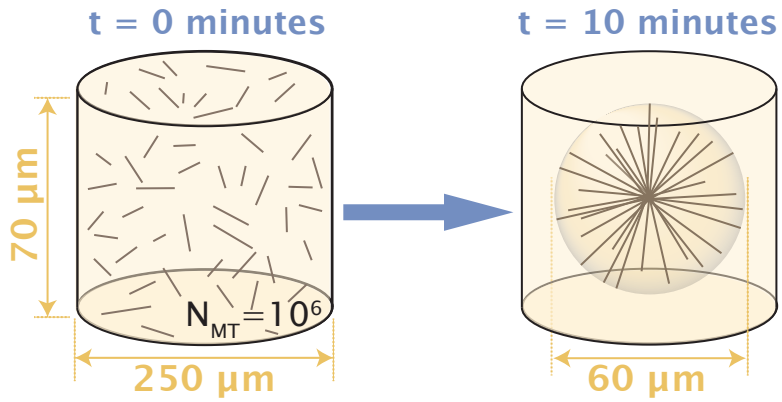

Figure 3.51: **The work of aster compression.** At the beginning of the experiment, microtubules are uniformly mixed throughout a cylinder of projected light. After some time, $\mathcal{T}$, microtubules organize into a spherical aster with a volume smaller than the initial cylinder volume.

l/a lattice sites that the microtubule center can occupy, see Figure 3.52. For two independently moving microtubules, this amounts to $(l/a)^2$ microstates. Thus the entropy of the independent microtubule case is

$$S_{\text{indep}} = 2k_{\text{B}} \ln\left(\frac{l}{a}\right). \tag{3.153}$$

If we now imagine a motor protein aligning the two microtubules, we now consider both microtubules to be on the same track. The microtubules now must move together. For the sake of this estimate, lets say that the microtubules are perfectly aligned with their ends at the same positions. The number of microstates of the coupled system is now only l/a, giving an entropy of

$$S_{\text{coup}} = k_{\text{B}} \ln\left(\frac{l}{a}\right). \tag{3.154}$$

We can compute the free energy of the microtubule coupling as

$$\begin{aligned} \Delta G = -T\Delta S = -T(S_{\text{coup}} - S_{\text{indep}}) \\ \Delta G = k_{\text{B}}T \ln\left(\frac{l}{a}\right). \end{aligned} \tag{3.155}$$

The length of stabilized microtubules in our experiment are $1\,\mu$m and the size of a motor step is 8 nm. Plugging in numbers, we find the free energy to couple two microtubules is

$$\Delta G = k_{\text{B}}T \ln\left(\frac{1000\text{ nm}}{8\text{ nm}}\right) \approx 5\,k_{\text{B}}T \approx 0.25\text{ ATP}, \tag{3.156}$$

where ATP $= 20\,k_{\mathrm{B}}T$ [31]. Say we wanted all of the microtubules in our aster system to fo rm one aligned bundle. Calculating the energy to couple all 2×10^6 microtubules together, the total energy is

$$\Delta G_{\mathrm{tot}} = \Delta G \times N_{\mathrm{MT}} = 5 \times 10^5 \text{ ATP}. \tag{3.157}$$

If the bundle is formed on the same timescale as the aster, about 10 minutes, the power of bundling is

$$P = \frac{\Delta G}{t} = \frac{5 \times 10^5 \text{ ATP}}{600 \text{ s}} \approx 10^3 \frac{\text{ATP}}{\text{s}}. \tag{3.158}$$

This estimate is five orders of magnitude smaller that the measured power, indicating that the entropic cost of microtubule coupling through motor dimerization is negligible.

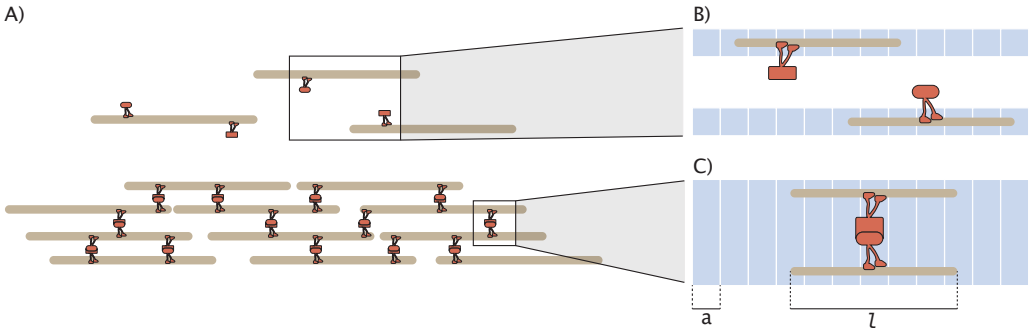

Figure 3.52: **Microtubule coupling.** A) Cross-linked microtubules form a bundle. B) Two microtubules on separate 1D tracks moving independently. C) Two microtubules aligned on the same track moving in unison.

Estimate of Power Associated with Dragging a Microtubule

One of the ways in which motors act is by producing motion. Like with most all real world motions, these processes dissipate energy. That is, some of the energy is transferred from the center of mass of the motor-cargo complex to the microscopic motions of the molecules making up the surrounding medium. This is revealed as dissipation. Here we ask what fraction of the ATP being consumed by each motor is converted into heat energy. In particular, we compute the power of a motor protein dragging a microtubule into an aster. This power can be expressed as

$$P = F_{\mathrm{D}} v, \tag{3.159}$$

where F_{D} is the drag force and v is the velocity of the motor.

To estimate the magnitude of this dissipation, we use the Stokes law to compute the drag force. Before making the calculation itself, we first examine the Reynolds number which gives us a measure of the dissipative forces and tells us whether we are in the regime of validity of the Stokes law. Since Stokes' law requires the system to be at low Reynolds number, we first make the following upper bound calculation for the Reynolds number in our experiment, namely,

$$Re = \frac{\rho v l}{\mu} = \frac{\left(10^3 \, \frac{\text{kg}}{\text{m}^3}\right) \times \left(10^{-7} \, \frac{\text{m}}{\text{s}}\right) \times \left(3 \times 10^{-5} \, \text{m}\right)}{10^{-3} \frac{\text{N}\cdot\text{s}}{\text{m}^2}} \approx 10^{-6}, \tag{3.160}$$

where $\rho = 1000\,\text{kg/m}^3$ is the fluid density, $v = 10^{-7}\,\text{m/s}$ is the measured motor speed of our NCD motors, $l = 3 \times 10^{-5}\,\text{m}$ is the measured aster radius, and $\mu = 0.003\,\text{N}\cdot\text{s/m}^2$ is the viscosity [32]. We see that the Reynolds number satisfies $Re << 1$. Since our experiment meets the low Reynolds number criterion, we can use the Stokes law ($F_D = 6\pi\mu r v$) for the drag force in equation 3.159, resulting in a power of the form

$$P_{\text{per MT}} = 6\pi\mu r v^2, \tag{3.161}$$

where r is an effective radius as we will describe below.

We begin with the most extreme model of the drag force which is to imagine a microtubule as a sphere. This approach gives us a first order-of-magnitude look at the scale of the mechanical power associated with fluid drag. This calculation provides an upper bound as it assumes the moving object to be a sphere, which we will take to a have a radius of half the length of a microtubule, as depicted in Figure 3.53. Using our measurements for microtubule length, $1\,\mu\text{m}$, and motor speed, $100\,\text{nm/s}$, we find the power for a single motor to drag a microtubule is

$$P_{\text{per MT}} = 6\pi \times \left(3 \times 10^{-3} \, \frac{\text{N}\cdot\text{s}}{\text{m}^2}\right) \times \left(5 \times 10^{-7} \, \text{m}\right) \times \left(10^{-7} \, \frac{\text{m}}{\text{s}}\right)^2 \approx 0.3 \, \frac{\text{pN}\cdot\text{nm}}{\text{s}}. \tag{3.162}$$

Taking $k_\text{B}T = 4\,\text{pN}\cdot\text{nm}$ and the energy of ATP hydrolysis $\Delta\mu_{\text{ATP}} = 20\,k_\text{B}T$, we can convert to units of ATP/s, resulting in

$$P_{\text{per MT}} = 4 \times 10^{-3} \, \frac{\text{ATP}}{\text{MT}\cdot\text{s}}. \tag{3.163}$$

The concentration of motor proteins to microtubules is 1000-fold, so if every single microtubule was being dragged into the aster at the same time, the maximum power from dragging microtubules would be the power per microtubule, as found in equation 3.162, multiplied by the number of microtubules, as estimated in equation 3.149,

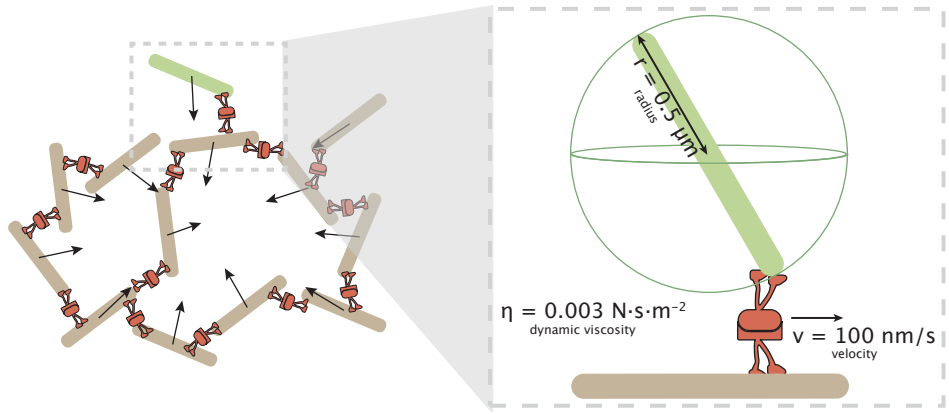

Figure 3.53: **Drag on a Microtubule.** This figure illustrates the set up to calculate the drag on a motor protein carrying a microtubule. On the left, many microtubules are dragged into the center of mass to create an aster. The inset shows the force of drag due to pulling a single microtubule. As an upper bound, the microtubule is depicted as a sphere with a diameter of the microtubule length, allowing the application of Stokes' law.

resulting in

$$P = P_{\text{per MT}} \times N_{\text{MT}} = \left(4 \times 10^{-3} \frac{\text{ATP}}{\text{s} \cdot \text{MT}}\right) \times \left(2 \times 10^{6}\ \text{MT}\right) \approx 10^{4} \frac{\text{ATP}}{\text{s}}. \quad (3.164)$$

Again, we find that this estimate is far lower than our measured power by four orders of magnitude. Note that we can go farther and more precisely treat the fluid drag on a cylinder, taking care to distinguish motion parallel or perpendicular to the long axis of the microtubule. But these estimates lead to an even smaller power and we leave them as an exercise for the reader.

Though it will result in an even smaller estimate, we now refine our previous estimates. We refine our sphere estimate, to more accurately represent the surface area of a cylinder. Our previous estimate significantly overestimates the size of the microtubule by taking the sphere diameter to be the length of the microtubule. Now we will compute the spherical drag for a sphere with the same surface area as our microtubule. For a cylindrical microtubule of length $l = 1\ \mu$m as measured, and a radius $r_{\text{cyl}} = \frac{25\text{ nm}}{2} \approx 10$ nm [31], the surface area is

$$S_{\text{cyl}} = 2\pi r_{\text{cyl}} l + 2\pi r_{\text{cyl}}^2 \approx 2\pi \times 10^{-2}\ \mu\text{m}^2. \quad (3.165)$$

We now find the spherical radius for a sphere with the same surface area as a cylinder,

$$\begin{aligned} S_{\text{sph}} &= 4\pi r_{\text{sph}}^2 = 2\pi(r_{\text{cyl}} l + r_{\text{cyl}}^2) = S_{\text{cyl}} \\ \Rightarrow r_{\text{sph}} &= \left(\frac{1}{2}(r_{\text{cyl}} l + r_{\text{cyl}}^2)\right)^{-2} = \left(\frac{1}{4\pi} S_{\text{cyl}}\right)^{-2}. \end{aligned} \quad (3.166)$$

Thus in our case,

$$r_{\text{sph}} = \left(5 \times 10^{-3}\right)^{-2} \, \mu\text{m} \approx 7 \times 10^{-2} \, \mu\text{m}. \tag{3.167}$$

Applying Stokes' Law for the new radius, we find

$$P_{\text{per MT}} = -6\pi \left(3 \times 10^{-3} \, \frac{\text{N} \cdot \text{s}}{\text{m}^2}\right) \left(7 \times 10^{-8} \, \text{m}\right) \left(10^{-7} \, \frac{\text{m}}{\text{s}}\right)^2 \tag{3.168}$$

$$\approx f \times 10^{-2} \, \text{pN} \cdot \text{nm} \approx f \times 10^{-4} \, \frac{\text{ATP}}{\text{s} \cdot \text{MT}}, \tag{3.169}$$

for each microtubule and

$$P = P_{\text{per MT}} \times N_{\text{MT}} = \left(f \times 10^{-4} \, \frac{\text{ATP}}{\text{s} \cdot \text{MT}}\right) \left(2 \times 10^6 \, \text{MT}\right) \approx 10^3 \, \frac{\text{ATP}}{\text{s}}, \tag{3.170}$$

for the process of dragging all microtubules. This is one order of magnitude lower than our previous estimate.

Nematic Order Parameter

Here, we attempt to find the free energy of organizing a two dimensional aster using the order parameter, $\mathbf{Q}$. We denote the orientation of each microtubule as

$$\mathbf{u} = (\cos\theta, \, \sin\theta) \tag{3.171}$$

and the order tensor as

$$Q_{ij} = \langle u_i u_j \rangle - \frac{1}{2}\delta_{ij} = \left\langle \begin{pmatrix} \cos^2\theta - \frac{1}{2} & \cos\theta \sin\theta \\ \cos\theta \sin\theta & \sin^2\theta - \frac{1}{2} \end{pmatrix} \right\rangle. \tag{3.172}$$

We assert that the aster is perfectly ordered, as locally all the microtubules point at the same θ. This eliminates the average surrounding the order parameter resulting in,

$$Q_{ij} = \begin{pmatrix} \cos^2\theta - \frac{1}{2} & \cos\theta \sin\theta \\ \cos\theta \sin\theta & \sin^2\theta - \frac{1}{2} \end{pmatrix}. \tag{3.173}$$

In the form written, Q_{ij} is in Cartesian coordinates, however the matrix elements are written in terms of θ, a polar coordinate. We write the elements in terms of Cartesian elements, where $\cos\theta = \frac{x}{\sqrt{x^2+y^2}}$ and $\sin\theta = \frac{y}{\sqrt{x^2+y^2}}$,

$$Q_{ij} = \begin{pmatrix} \frac{x^2}{x^2+y^2} - \frac{1}{2} & \frac{xy}{x^2+y^2} \\ \frac{xy}{x^2+y^2} & \frac{y^2}{x^2+y^2} - \frac{1}{2} \end{pmatrix}. \tag{3.174}$$

Note that this tensor is both traceless,

$$\begin{aligned} Q_{11} + Q_{22} &= \frac{x^2}{x^2+y^2} - \frac{1}{2} + \frac{y^2}{x^2+y^2} - \frac{1}{2} = 0 \\ \Rightarrow Q_{11} &= -Q_{22}, \end{aligned} \tag{3.175}$$

and symmetric,

$$Q_{ij} = \begin{pmatrix} Q_{11} & Q_{12} \\ Q_{21} & Q_{22} \end{pmatrix} = \begin{pmatrix} Q_{11} & Q_{21} \\ Q_{12} & Q_{22} \end{pmatrix} = Q_{ji} \tag{3.176}$$

given that,

$$Q_{12} = \frac{xy}{x^2+y^2} = Q_{21}. \tag{3.177}$$

Free Energy Density

With the nematic order parameter in toe, we can now compute the free energy density gradient using the Landau-Ginsberg theory. According to Julia Yeomans' lecture notes [33], there are two components to the free energy density: the bulk free energy density, which follows the Landau-de Gennes expression,

$$F_{\text{bulk}} = \frac{A}{2}(Q_{ij}Q_{ji}) + \frac{B}{3}(Q_{ij}Q_{jk}Q_{ki}) + \frac{C}{4}(Q_{ij}Q_{ji})^2, \tag{3.178}$$

and the elastic free energy density, which in 2D is,

$$F_{\text{el}} = \underbrace{\frac{L_1}{2}(\partial_k Q_{ij})^2}_{\text{splay}} + \underbrace{\frac{L_3}{2}Q_{ij}(\partial_i Q_{kl})(\partial_j Q_{kl})}_{\text{bend}}. \tag{3.179}$$

All together, the free energy density in terms of Q_{ij} is,

$$\begin{aligned} F = F_{\text{bulk}} + F_{\text{el}} =& \frac{A}{2}(Q_{ij}Q_{ji}) + \frac{B}{3}(Q_{ij}Q_{jk}Q_{ki}) + \frac{C}{4}(Q_{ij}Q_{ji})^2 + \cdots \\ &+ \frac{L_1}{2}(\partial_k Q_{ij})^2 + \frac{L_3}{2}Q_{ij}(\partial_i Q_{kl})(\partial_j Q_{kl}) + \cdots. \end{aligned} \tag{3.180}$$

Here, we will evaluate each listed term. We begin with the power series and examine up to fourth order. First expanding the summation notation of the quadratic term, we find

$$\begin{aligned} Q_{ij}Q_{ji} &= \sum_j \sum_i Q_{ij}Q_{ji} \\ &= \sum_j (Q_{1j}Q_{j1} + Q_{2j}Q_{j2}) \\ &= Q_{11}Q_{11} + Q_{21}Q_{12} + Q_{12}Q_{21} + Q_{22}Q_{22}. \end{aligned} \tag{3.181}$$

Due to the tracelessness of Q_{ij}, $Q_{11}^2 = Q_{22}^2$, and due to the matrix being symmetric, $Q_{12} = Q_{21}$, thus, we can simplify the result to

$$Q_{ij}Q_{ji} = 2Q_{11}^2 + 2Q_{12}^2. \tag{3.182}$$

Plugging in the matrix elements of equation 3.190, the quadratic term evaluates to

$$\begin{aligned} Q_{ij}Q_{ji} &= 2\left(\frac{x^2}{x^2+y^2} - \frac{1}{2}\right)^2 + 2\left(\frac{xy}{x^2+y^2}\right)^2 \\ &= 2\left(\frac{x^4}{(x^2+y^2)^2} - \frac{x^2}{x^2+y^2} + \frac{1}{4} + \frac{x^2y^2}{(x^2+y^2)^2}\right) \\ &= 2\left(\frac{x^4}{(x^2+y^2)^2} - \frac{x^4+x^2y^2}{(x^2+y^2)^2} + \frac{1}{4} + \frac{x^2y^2}{(x^2+y^2)^2}\right) \\ &= \frac{1}{2}. \end{aligned} \tag{3.183}$$

Let us now compute the cubic term,

$$\begin{aligned} Q_{ij}Q_{jk}Q_{ki} &= \sum_k \sum_j \sum_i Q_{ij}Q_{jk}Q_{ki} \\ &= \sum_k \sum_j (Q_{1j}Q_{jk}Q_{k1} + Q_{2j}Q_{jk}Q_{k2}) \\ &= \sum_k (Q_{11}Q_{1k}Q_{k1} + Q_{21}Q_{1k}Q_{k2} + Q_{12}Q_{2k}Q_{k1} + Q_{22}Q_{2k}Q_{k2}) \\ &= Q_{11}Q_{11}Q_{11} + Q_{21}Q_{11}Q_{12} + Q_{12}Q_{21}Q_{11} + Q_{22}Q_{21}Q_{12} \\ &\quad + Q_{11}Q_{12}Q_{21} + Q_{21}Q_{12}Q_{22} + Q_{12}Q_{22}Q_{21}Q_{22}Q_{22}Q_{22} \\ &= Q_{11}^3 + 3Q_{11}Q_{12}^2 + 3Q_{22}Q_{12}^2 + Q_{22}^3. \end{aligned} \tag{3.184}$$

By the symmetry of Q_{ij},

$$Q_{ij}Q_{jk}Q_{ki} = Q_{11}^3 + 3Q_{11}Q_{12}^2 + 3Q_{22}Q_{12}^2 + Q_{22}^3, \tag{3.185}$$

and given that the matrix is traceless,

$$Q_{ij}Q_{jk}Q_{ki} = Q_{11}^3 + 3Q_{11}Q_{12}^2 - 3Q_{11}Q_{12}^2 + (-Q_{11})^3 = 0, \tag{3.186}$$

so the cubic term vanishes. We now compute the quartic term using the result from equation 3.182

$$\begin{aligned} (Q_{ij}Q_{ji})^2 &= \left(\sum_j \sum_i Q_{ij}Qji\right)^2 \\ &= \left(2Q_{11}^2 + 2Q_{12}^2\right)^2. \end{aligned} \tag{3.187}$$

Thus, the quartic term is simply the square of the quadratic term, which evaluates to

$$(Q_{ij}Q_{ji})^2 = \left(\frac{1}{2}\right)^2 = \frac{1}{4}. \tag{3.188}$$

We now compute the derivative terms. We write the partial first derivatives of Q_{ij} as follows.

First Derivatives:

$$\frac{\partial}{\partial x}Q_{ij} = \begin{pmatrix} \partial_1 Q_{11} & \partial_1 Q_{12} \\ \partial_1 Q_{21} & \partial_1 Q_{22} \end{pmatrix} = \begin{pmatrix} \frac{2xy^2}{(x^2+y^2)^2} & \frac{y(-x^2+y^2)}{(x^2+y^2)^2} \\ \frac{y(-x^2+y^2)}{(x^2+y^2)^2} & -\frac{2xy^2}{(x^2+y^2)^2} \end{pmatrix} \tag{3.189}$$

$$\frac{\partial}{\partial y}Q_{ij} = \begin{pmatrix} \partial_2 Q_{11} & \partial_2 Q_{12} \\ \partial_2 Q_{21} & \partial_2 Q_{22} \end{pmatrix} = \begin{pmatrix} -\frac{2x^2y}{(x^2+y^2)^2} & \frac{x(x^2-y^2)}{(x^2+y^2)^2} \\ \frac{x(x^2-y^2)}{(x^2+y^2)^2} & \frac{2x^2y}{(x^2+y^2)^2} \end{pmatrix}. \tag{3.190}$$

Note that the matrices representing the first derivatives are also traceless and symmetric, meaning $\partial_k Q_{11} = -\partial_k Q_{22}$ and $\partial_k Q_{12} = \partial_k Q_{21}$.

Computing the first term in the elastic free energy density, we find

$$\begin{aligned}(\partial_k Q_{ij})^2 &= \sum_k \sum_j \sum_i (\partial_k Q_{ij})^2 \\ &= \sum_k \sum_j (\partial_k Q_{1j})^2 + (\partial_k Q_{2j})^2 \\ &= \sum_k (\partial_k Q_{11})^2 + (\partial_k Q_{12})^2 + (\partial_k Q_{21})^2 + (\partial_k Q_{22})^2 \\ &= (\partial_1 Q_{11})^2 + (\partial_2 Q_{11})^2 + (\partial_1 Q_{12})^2 + (\partial_2 Q_{12})^2 + (\partial_1 Q_{21})^2 + (\partial_2 Q_{21})^2 + (\partial_1 Q_{22})^2 + (\partial_2 Q_{22})^2.\end{aligned} \tag{3.191}$$

By the properties $Q_{11} = -Q_{22}$, and $Q_{12} = Q_{21}$,

$$(\partial_k Q_{ij})^2 = 2(\partial_1 Q_{11})^2 + 2(\partial_2 Q_{11})^2 + 2(\partial_1 Q_{12})^2 + 2(\partial_2 Q_{12})^2. \tag{3.192}$$

Plugging in the matrix elements,

$$\begin{aligned}(\partial_k Q_{ij})^2 &= \frac{8x^2y^4}{(x^2+y^2)^4} + \frac{8x^4y^2}{(x^2+y^2)^4} + \frac{2y^2(-x^2+y^2)^2}{(x^2+y^2)^4} + \frac{2x^2(x^2-y)^2}{(x^2+y^2)^4} \\ &= \frac{2}{x^2+y^2}.\end{aligned} \tag{3.193}$$

We now compute the second term in the elastic free energy density and use the simplifications that Q_{ij} is symmetric and traceless,

$$\begin{aligned}
Q_{ij}(\partial_i Q_{kl})(\partial_j Q_{kl}) &= \sum_l \sum_k \sum_j \sum_i Q_{ij}(\partial_i Q_{kl})(\partial_j Q_{kl}) \\
&= \sum_l \sum_k Q_{11}(\partial_1 Q_{kl})^2 + 2Q_{12}(\partial_1 Q_{kl})(\partial_2 Q_{kl}) + Q_{22}(\partial_2 Q_{kl})^2 \\
&= Q_{11}(\partial_1 Q_{11})^2 + 2Q_{11}(\partial_1 Q_{12})^2 + Q_{11}(\partial_1 Q_{22})^2 \\
&\quad + 2Q_{12}(\partial_1 Q_{11})(\partial_2 Q_{11}) + 4Q_{12}(\partial_1 Q_{12})(\partial_2 Q_{12}) + 2Q_{12}(\partial_1 Q_{22})(\partial_2 Q_{22}) \\
&\quad + Q_{22}(\partial_2 Q_{11})^2 + 2Q_{22}(\partial_2 Q_{12})^2 + Q_{22}(\partial_2 Q_{22})^2 \\
&= 2Q_{11}(\partial_1 Q_{11})^2 + 2Q_{11}(\partial_1 Q_{12})^2 \\
&\quad + 4Q_{12}(\partial_1 Q_{11})(\partial_2 Q_{11}) + 4Q_{12}(\partial_1 Q_{12})(\partial_2 Q_{12}) \\
&\quad - 2Q_{11}(\partial_2 Q_{11})^2 - 2Q_{11}(\partial_2 Q_{12})^2 \\
&= 2Q_{11}\Big[(\partial_1 Q_{11})^2 + (\partial_1 Q_{12})^2 - (\partial_2 Q_{11})^2 - (\partial_2 Q_{12})^2\Big] \\
&\quad + 4Q_{12}\Big[(\partial_1 Q_{11})(\partial_2 Q_{11}) + (\partial_1 Q_{12})(\partial_2 Q_{12})\Big].
\end{aligned} \tag{3.194}$$

Plugging in matrix values and simplifying with Mathematica, this term reduces to

$$Q_{ij}(\partial_i Q_{kl})(\partial_j Q_{kl}) = -\frac{1}{x^2+y^2}. \tag{3.195}$$

Putting everything together, we reveal an equation for the free energy density throughout an ordered aster

$$F = \frac{A}{2}\left(\frac{1}{2}\right) + \frac{C}{4}\left(\frac{1}{4}\right) + \cdots + \frac{L_1}{2}\frac{2}{x^2+y^2} - \frac{L_3}{2}\frac{1}{x^2+y^2} + \cdots . \tag{3.196}$$

We can translate this back into polar coordinates using the transforms $r = \sqrt{x^2+y^2}$, $\cos\theta = \frac{x}{\sqrt{x^2+y^2}}$ and $\sin\theta = \frac{y}{\sqrt{x^2+y^2}}$

$$F = \frac{4A+C}{16} + \frac{2L_1 - L_3}{2}\frac{1}{r^2} + \cdots . \tag{3.197}$$

Now it is left to find the energy of the aster state by integrating the free energy density over the area of the aster. We integrate over all angles from $0 \leq \theta \leq 2\pi$ and

radius values from a core cutoff, R_c to the aster radius R,

$$\begin{aligned} E &= \int_0^{2\pi} \int_{R_c}^{R} F\, r\, \mathrm{d}r\, \mathrm{d}\theta \\ &= \int_0^{2\pi} \int_{R_c}^{R} \left(\frac{4A + C}{16} r + \frac{2L_1 - L_3}{2r} \right) \mathrm{d}r\, \mathrm{d}\theta \\ &= \frac{4A + C}{8} \pi (R^2 - R_c^2) + (2L_1 - L_3)\pi \ln\left(\frac{R}{R_c}\right). \end{aligned} \tag{3.198}$$

Now that we have solved the equation for the energy of the ordered state, we can input parameters to find the energy scale of perfect order.

Order of Magnitude Estimate

To get a sense of scale of the energy in equation 3.198, we explore literature values for the constants in front of each term. Zhang et al. use modeling, simulations, and experiments to find how the elasticity of a liquid crystal (LC) depends on filament length, density, and rigidity. Their system, a thin film nematic of actin and microtubules, follows the same free energy density form as equation 3.197. In their study, they measure elastic constants, K, using elastic beam theory. They find that $L_1 = \frac{K}{2q_0^2}$, where L_1 is the coefficient of the $(\partial_k Q_{ij})^2$, same as us, and q_0 is the scalar order parameter. Thus, if we assume the L_1 term is at least of the same order as the other terms, we can get an order of magnitude estimate for the ordered energy of the aster. Since our aster is assumed to be perfectly ordered, we take $q_0 = 1$. Zhang et al. find $K \sim f \times 10^{-1}$ pN [34]. Thus, $L_1 \approx 0.1$ pN. Note that for the constant L_1 to have units of piconewtons, the free energy density must be integrated over a volume rather than an area. Since their system was a very thin film of $\delta_z = 300$ nm, their system is still quasi 2D in comparison to their large film area $4\,\mathrm{mm}^2$. While the thickness of the aster is non-trivial, we will simply proceed with this estimate to find the energy scale of ordering. Thus, we will integrate over z, the thickness of the aster, in our estimate,

$$E = \frac{4A + C}{8} \pi z (R^2 - R_c^2) + (2L_1 - L_3)\pi z \ln\left(\frac{R}{R_c}\right). \tag{3.199}$$

Taking the aster radius to be $R \approx f \times 10\,\mu$m, the cutoff radius to be $R_c \approx 1\,\mu$m, and the thickness to be $z \approx 100\,\mu$m, we find the value of the L_1 term of the energy,

$$E \sim 2\pi L_1 z \ln\left(\frac{R}{R_c}\right) = 2\pi \times 10^{-1}\ \text{pN} \times 10^5\ \text{nm} \times \ln(f \times 10) \approx f \times 10^5\ \text{pN} \cdot \text{nm}. \tag{3.200}$$

With the conversion ATP $= 20\, k_B T \left(\frac{4\,\text{pN}\cdot\text{nm}}{k_B T}\right) = 80\,\text{pN}\cdot\text{nm}$, the free energy of the ordered aster is $f \times 10^3$ ATP. If an aster takes around 10 minutes to form, then the power of organization is

$$P = \frac{f \times 10^3\ \text{ATP}}{600\ \text{s}} = f\,\frac{\text{ATP}}{\text{s}}. \tag{3.201}$$

This is VERY low in comparison with our measured power of $10^8\ \frac{\text{ATP}}{\text{s}}$. While other studies have found K constant values as large as 10 pN [35], this would only increase our power by a factor of 100, still six orders of magnitude smaller than the measured value. Thus, the power of ordering microtubules appears to be negligible.

3.11 Key Numbers

Size of a protein

The volume of a protein is thought to scale linearly with the number of amino acids in the sequence [31]. When a sequence is unavailable, the average amino acid (a.a.) weighs 100 Da, providing an easy conversion from molecular weight. Rubisco is a well characterized protein with a molecular weight of 55 kDa, a sequence length of 500 a.a., and a diameter of $3 - 6$ nm. Thus if we want to create a rule for scaling protein radii, we can write

$$r \approx 2\ \text{nm} \times \left(\frac{\#\ \text{a.a.}}{500\ \text{a.a.}}\right)^{1/3} \approx 2\ \text{nm} \times \left(\frac{\text{MW}}{55\ \text{kDa}}\right)^{1/3}. \tag{3.202}$$

Our experiments contain two proteins, motors and the ATP probe. Our motor proteins weigh approximately 100 kDa, giving a radius of

$$r_{\text{motor}} \approx 2\ \text{nm} \times \left(\frac{100\ \text{kDa}}{55\ \text{kDa}}\right)^{1/3} \approx 2.4\ \text{nm}. \tag{3.203}$$

The ATP probe has a sequence length of 1800 base pairs, which corresponds to 600 a.a. since each amino acid contains three base pairs. Thus, the radius of the ATP probe is

$$r_{\text{probe}} \approx 2\ \text{nm} \times \left(\frac{600\ \text{a.a.}}{500\ \text{a.a.}}\right)^{1/3} \approx 2.1\ \text{nm}. \tag{3.204}$$

Reynold's Number

We can show that our system is at low Reynold's number, meaning viscous forces dominate using the definition,

$$Re = \frac{\rho v l}{\mu}, \tag{3.205}$$

where ρ is the density, v is the velocity, l is the characteristic length scale, and μ is the viscosity. Our reaction mix contains 30% glycerol in water based reagents at room temperature. We take the density of our mix to be $\rho \sim 1000\,\frac{\text{kg}}{\text{m}^3}$ and the viscosity to be $\mu = 2.4 \times 10^{-3}\,\text{N}\cdot\text{s}/\text{m}^2$ based on a calculator developed at the University of Reading [32]. For the velocity, we will take an upper bound for motor speeds, $v = 1\frac{\mu\text{m}}{\text{s}}$ [36]. And for the characteristic length scale, we will take the motor decay length as previously measured in our lab, $l = 15\,\mu\text{m}$ [37]. This evaluates to a Reynold's number of

$$Re \approx 6 \times 10^{-6} << 1. \tag{3.206}$$

Diffusion Constants

Given that our system is at low Reynold's number (Equation 3.206), we can compute an expected diffusion constant for molecules in our system using the Stokes-Einstein equation,

$$D = \frac{k_\text{B}T}{6\pi\mu r}, \tag{3.207}$$

where μ is the viscosity of the media and r is the radius of the molecule. Using the viscosity of our system ($\mu = 2.4 \times 10^{-3}\,\text{N}\cdot\text{s}/\text{m}^2$ [32]), the diffusion constant of a species only depends on its radius,

$$D = \frac{k_\text{B}T}{6\pi\mu r} = \frac{4\,\text{pN}\cdot\text{nm}}{6\pi r(2.4 \times 10^{-3}\,\text{pN}\cdot\text{s}/\mu\text{m}^2)} \approx \frac{90\text{ nm}}{r}\,\frac{\mu\text{m}^2}{\text{s}}, \tag{3.208}$$

given that $k_\text{B}T \approx 4\,\text{pN}\cdot\text{nm}$. We can now compute the relevant diffusion constants for each molecule in the experiment: ATP has a radius of 0.7 nm, (BNID 106798), which leads to a diffusion coefficient of

$$D_\text{ATP} \approx 130\,\mu\text{m}^2/\text{s}. \tag{3.209}$$

Our motor proteins have a radius of about 2.4 nm (equation 3.203), giving a diffusion constant of

$$D_\text{motor} \approx 40\,\mu\text{m}^2/\text{s}. \tag{3.210}$$

Tubulin has a length of 4 nm [31], so we will take a radius of 2 nm, giving a diffusion constant of

$$D_\text{tubulin} \approx 45\,\mu\text{m}^2/\text{s}. \tag{3.211}$$

Microtubules have an experimentally measured length of 1 μm, so we will take a radius of 500 nm giving a diffusion constant of

$$D_\text{MT} \approx 0.2\,\mu\text{m}^2/\text{s}. \tag{3.212}$$

The ATP probe (Queen A81D) has a radius of about 2 nm (equation 3.204), same as tubulin, giving the diffusion constant of the probe

$$D_{\text{Queen A81D}} \approx 45\,\mu\text{m}^2/\text{s}. \tag{3.213}$$

Binding Rates and Bound Fractions

If we know the on/off rates or the equilibrium constant for two species and the total initial concentrations of each species, we can determine the bound fraction of a ligand to a receptor at equilibrium. Taking $[L]$ and $[R]$ for the concentrations of free ligands and receptors respectively, and $[LR]$as the bound concentration of ligands and receptors, we write the chemical equation,

$$[L] + [R] \underset{k_{\text{off}}}{\overset{k_{\text{on}}}{\rightleftharpoons}} [LR], \tag{3.214}$$

with an equilibrium constant defined as

$$K_{\text{eq}} = \frac{k_{\text{off}}}{k_{\text{on}}} = \frac{[\text{L}][\text{R}]}{[\text{LR}]}. \tag{3.215}$$

Assuming we know the total concentration of the ligand and receptor species, regardless of their binding states, we specify the total concentration of ligands as,

$$l = [\text{L}] + [\text{LR}] \tag{3.216}$$

and of receptors as,

$$r = [\text{R}] + [\text{LR}]. \tag{3.217}$$

The probability of ligands being bound to receptors is,

$$p_b = \frac{[LR]}{l}, \tag{3.218}$$

which we can write in terms of the equilibrium constant using Equation 3.215,

$$p_b = \frac{[L][R]}{K_{\text{eq}} l}. \tag{3.219}$$

Substituting equations 3.216 and 3.217, we can solve for the bound probability in terms of the total ligand and receptor concentrations and the equilibrium constant as follows,

$$p_b = \frac{(l - [LR])(r - [LR])}{K_{\text{eq}} l}. \tag{3.220}$$

Expanding the numerator,

$$p_b = \frac{lr - [LR]r - l[LR] + [LR]^2}{K_{\text{eq}} l} = \frac{1}{K_{\text{eq}}}\left(r - \frac{[LR]}{l}(r + l) + l\frac{[LR]^2}{l^2}\right), \tag{3.221}$$

and substituting $\frac{[LR]}{l} = p_b$,

$$p_b = \frac{1}{K_{\text{eq}}}\left(r - p_b(r+l) + l p_b^2\right). \tag{3.222}$$

We are left with a quadratic equation in terms of p_b,

$$l p_b^2 - p_b(K_{\text{eq}} + r + l) + r = 0 \tag{3.223}$$

solving for the fraction of bound species, we employ the quadratic formula,

$$p_b = \frac{K_{\text{eq}} + r + l - \sqrt{(-K_{\text{eq}} - r - l)^2 - 4lr}}{2l}, \tag{3.224}$$

noting that we must chose the "minus," square root subtracted, form to ensure that $p_b > 0$. Using this equation, the fraction of bound species at equilibrium can easily be determined!

Motor to Microtubule

Reference [37] measured the equilibrium constant for NCD Kinesin motors to be approximately 50 μM. In our experiment, we add approximately 1 μM of tubulin. If each tubulin has 13 binding sites, we will take 13 μM of tubulin binding sites as the total receptor concentration, r. For the ligand, we add approximately 1 μM of motor proteins, which we take as the total ligand concentration, l. Plugging these values into equation 3.224, we find the bound fraction of motor proteins is,

$$\begin{aligned} p_b &= \frac{50 + 13 + 1 - \sqrt{(-50 - 13 - 1)^2 - 4 \times 1 \times 13}}{2 \times 1} \\ &= \frac{64 - \sqrt{4044}}{2} \\ &= \frac{64 - 63.6}{2} \\ &= 0.2, \end{aligned} \tag{3.225}$$

indicating that approximately 20% of motor proteins are bound at equilibrium.

ATP to Probe

The ATP probe we use, Queen A81D [2], is a mutant of the Queen-7µ probe, developed in 2014 by the same group [2], using the epsilon subunit of *Bacillus* PS3. The authors characterized the dissociation constant of ATP to the probe at room temperature and found $K_{\text{d}} \sim 7\,\mu$M [18]. If we allowed the ATP probe to equilibrate

with our initial concentration of ATP, before any motor hydrolysis, we can compute an upper bound for the bound fraction of ATP. Initially, we pipette 500 μM of ATP into the reaction with approximately 3 μM of the ATP probe. Using equation 3.224, we solve for the bound fraction of ATP at equilibrium,

$$\begin{aligned} p_b &= \frac{7+3+500-\sqrt{(-7-3-500)^2-4\times 500\times 3}}{2\times 500} \\ &= \frac{510-\sqrt{254100}}{1000} \\ &= \frac{510-504}{1000} \\ &= 0.006, \end{aligned} \tag{3.226}$$

so only 0.6% of ATP is bound to the probe at equilibrium at a given time. Thus, at high ATP conditions, the effect of ATP binding to the probe should not impact the binding dynamics of ATP to motor proteins. However, as the experiment runs, ATP is hydrolyzed by the motor proteins. We can compute the binding fraction in the limit that the concentration approaches zero. Plugging $l = 0$ into equation 3.224, we find $p_b = \frac{0}{0}$, which invites us to envoke l'hôpital's rule. The first derivative of the numerator with respect to l is

$$1-\frac{1}{2}\frac{-2(-K_{\text{eq}}-r-l)-4r}{\sqrt{(-K_{\text{eq}}-r-l)^2-4lr}} = 1-\frac{K_{\text{eq}}-r}{\sqrt{(-K_{\text{eq}}-r-l)^2-4lr}} \tag{3.227}$$

and the first derivative of the denominator with respect to l is simply 2. Thus,

$$\lim_{l\to 0} p_{\text{b}} = \frac{1}{2}-\frac{1}{2}\frac{K_{\text{eq}}-r}{K_{\text{eq}}+r}. \tag{3.228}$$

Plugging in the dissociation constant and total concentration of ATP probe,

$$\lim_{l\to 0} p_{\text{b}} = \frac{1}{2}-\frac{7-3}{2\times 10} = 0.5-0.2 = 0.3. \tag{3.229}$$

Hence, as ATP becomes scarce in the system, we can expect the binding to the ATP probe to slow the motor dynamics. Plotting equation 3.224 as a function of ATP concentration when $K_{\text{eq}} + r = 10\,\mu$M, we find agreement in the limit of $l \to 0$, as shown in figure.

References

[1] Bibi Najma et al. "Competing instabilities reveal how to rationally design and control active crosslinked gels." In: *Nature Communications* 13.1 (2022), p. 6465.

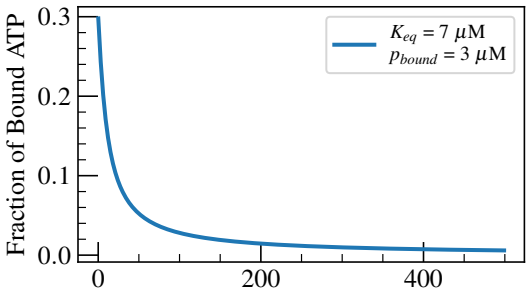

Figure 3.54: **Fraction of ATP bound to the ATP reporter as function of ATP.** At high ATP concentrations, the fraction of ATP bound to the probe is small, not impacting the amount of available ATP in the bulk.

[2] Hideyuki Yaginuma and Yasushi Okada. "Live cell imaging of metabolic heterogeneity by quantitative fluorescent ATP indicator protein, QUEEN-37C." In: *BioRxiv* (2021), pp. 2021–10.

[3] Bibi Najma et al. "Microscopic interactions control a structural transition in active mixtures of microtubules and molecular motors." In: *Proceedings of the National Academy of Sciences* 121.2 (2024), e2300174121.

[4] Teledyne Photometrics. *Camera Test Protocol*. https://www.photometrics.com/learn/camera-test-protocol. Accessed: (2024). 2019.

[5] Nilanjan Dey. "Uneven illumination correction of digital images: A survey of the state-of-the-art." In: *Optik* 183 (2019), pp. 483–495.

[6] Hernan G Garcia and Rob Phillips. "Quantitative dissection of the simple repression input–output function." In: *Proceedings of the National Academy of Sciences* 108.29 (2011), pp. 12173–12178.

[7] L Montgomery Smith, Dennis R Keefer, and SI Sudharsanan. "Abel inversion using transform techniques." In: *Journal of Quantitative Spectroscopy and Radiative Transfer* 39.5 (1988), pp. 367–373.

[8] Stephen Gibson et al. *PyAbel/PyAbel: v0.9.0*. Version v0.9.0. Dec. 2022. DOI: 10.5281/zenodo.7438595. URL: https://doi.org/10.5281/zenodo.7438595.

[9] Daniel Sage et al. "DeconvolutionLab2: An open-source software for deconvolution microscopy." In: *Methods* 115 (2017), pp. 28–41.

[10] Max Born and Emil Wolf. *Principles of optics: electromagnetic theory of propagation, interference and diffraction of light*. Elsevier, 2013.

[11] Eugene Hecht. *Optics*. 4th. San Francisco: Addison Wesley, 2003. ISBN: 978-0805385663.

[12] Hagai Kirshner et al. “3-D PSF fitting for fluorescence microscopy: implementation and localization application.” In: *Journal of microscopy* 249.1 (2013), pp. 13–25.

[13] Sjoerd Stallinga and Bernd Rieger. “Accuracy of the Gaussian point spread function model in 2D localization microscopy.” In: *Optics express* 18.24 (2010), pp. 24461–24476.

[14] Bo Zhang, Josiane Zerubia, and Jean-Christophe Olivo-Marin. “Gaussian approximations of fluorescence microscope point-spread function models.” In: *Applied optics* 46.10 (2007), pp. 1819–1829.

[15] Marco Prato et al. “Efficient deconvolution methods for astronomical imaging: algorithms and IDL-GPU codes.” In: *Astronomy & Astrophysics* 539 (2012), A133.

[16] François Aguet, Dimitri Van De Ville, and Michael Unser. “Model-based 2.5-D deconvolution for extended depth of field in brightfield microscopy.” In: *IEEE Transactions on Image Processing* 17.7 (2008), pp. 1144–1153.

[17] Hiromi Imamura et al. “Visualization of ATP levels inside single living cells with fluorescence resonance energy transfer-based genetically encoded indicators.” In: *Proceedings of the National Academy of Sciences* 106.37 (2009), pp. 15651–15656.

[18] Hideyuki Yaginuma et al. “Diversity in ATP concentrations in a single bacterial cell population revealed by quantitative single-cell imaging.” In: *Scientific Reports* 4.1 (2014), p. 6522.

[19] D. L. Jones, R. C. Brewster, and R. Phillips. “Promoter architecture dictates cell-to-cell variability in gene expression.” In: *Science* 346.6216 (2014), pp. 1533–6.

[20] Rosalind Wenshan Pan et al. “Deciphering regulatory architectures of bacterial promoters from synthetic expression patterns.” In: *PLOS Computational Biology* 20.12 (2024), e1012697.

[21] Ahmed A Heikal et al. “Molecular spectroscopy and dynamics of intrinsically fluorescent proteins: coral red (dsRed) and yellow (Citrine).” In: *Proceedings of the National Academy of Sciences* 97.22 (2000), pp. 11996–12001.

[22] Christian Eggeling et al. “Photobleaching of fluorescent dyes under conditions used for single-molecule detection: evidence of two-step photolysis.” In: *Analytical chemistry* 70.13 (1998), pp. 2651–2659.

[23] Rob Phillips et al. *Physical biology of the cell*. Garland Science, 2012.

[24] William R. Schief et al. “Inhibition of kinesin motility by ADP and phosphate supports a hand-over-hand mechanism.” In: *Proceedings of the National Academy of Sciences* 101.5 (2004), pp. 1183–1188.

[25] David L Coy, Michael Wagenbach, and Jonathon Howard. “Kinesin takes one 8-nm step for each ATP that it hydrolyzes.” In: *Journal of Biological Chemistry* 274.6 (1999), pp. 3667–3671.

[26] A. H. Stouthamer. “Theoretical study on amount of ATP required for synthesis of microbial cell material.” In: *Antonie Van Leeuwenhoek Journal of Microbiology* 39.3 (1973), pp. 545–565.

[27] M. Lynch and G. K. Marinov. “The bioenergetic costs of a gene.” In: *Proceedings of the National Academy of Sciences of the United States of America* 112.51 (2015), pp. 15690–15695.

[28] John J. Hopfield. “Kinetic proofreading: A new mechanism for reducing errors in biosynthetic processes requiring high specificity.” In: *Proceedings of the National Academy of Sciences of the United States of America* 71.10 (1974), pp. 4135–9.

[29] T. L. Hill and Marc W. Kirschner. “Bioenergetics and kinetics of microtubule and actin filament assembly-disassembly.” In: *Int Rev Cytol* 78 (1982), pp. 1–125.

[30] Tim J. Mitchison and Marc W. Kirschner. “Properties of the Kinetochore In vitro. II. Microtubule Capture and ATP-Dependent Translocation.” In: *Journal of Cell Biology* 101.3 (1985), pp. 766–777.

[31] Ron Milo and Rob Phillips. *Cell biology by the numbers*. Garland Science, 2015.

[32] Chris Westbrook. *Calculate density and viscosity of glycerol/water mixtures*. Accessed: 2024. 2018. URL: %7Bhttps://www.met.reading.ac.uk/~sws04cdw/viscosity_calc.html%7D.

[33] Julia M Yeomans. “The hydrodynamics of active systems.” In: *La Rivista del Nuovo Cimento* 40.1 (2017), pp. 1–31.

[34] Rui Zhang et al. “Interplay of structure, elasticity, and dynamics in actin-based nematic materials.” In: *Proceedings of the National Academy of Sciences* 115.2 (2018), E124–E133.

[35] Rui Zhang et al. “Dynamic structure of active nematic shells.” In: *Nature Communications* 7.1 (2016), p. 13483.

[36] Mark Schnitzer and Steven Block. “Kinesin hydrolyses one ATP per 8-nm step.” In: *Nature* 388 (1997), pp. 386–390.

[37] Rachel A. Banks et al. “Motor processivity and speed determine structure and dynamics of microtubule-motor assemblies.” In: *Elife* 12 (2023), e79402.